2023

An Integrated Algorithm for Automatic GPR Data Processing for Concrete Rebar Location

Lihong Mao

An Integrated Algorithm for Automatic GPR Data Processing for Concrete Rebar Location

by

Lihong Mao

Presented to the Faculty of the Graduate School of The University of Texas at Arlington in

Partial Fulfillment for the Requirements for the Degree of

DOCTOR OF PHILOSOPHY

University of Texas at Arlington

August 2023

ACKNOWLEDGEMENTS

I would like to express my deepest gratitude to all the individuals and organizations who have contributed to the successful completion of my Ph.D. research.

First and foremost, I am immensely thankful to my supervisor, Dr. Nur Yazdani, for his unwavering support, guidance, and encouragement throughout my Ph.D. journey. His expertise, patience, and insightful feedback have been invaluable in shaping my research and academic growth.

I would also like to extend my heartfelt appreciation to my postdoc, Dr. Beneberu Eyosias Solomon, for his valuable assistance in reviewing my papers and providing constructive feedback. His mentorship has played a crucial role in enhancing the quality of my research work. I am grateful to the members of my committee, Dr. ARaad Azzawi, Dr. Ashraf Warda, and Sharma Chakravarthy, for their valuable time, expertise, and feedback during the evaluation of my research. Their insightful comments and suggestions have significantly improved the quality of my dissertation.

I extend my sincere gratitude to DeKar Debashish and Mahala Avinash, research assistants from the Computer Science Department, for their invaluable technical support and innovative contributions in developing my application. I also acknowledge the contributions of my colleagues, Alateeq, Ahmed Abdullah, Jalal, Khadiza Binte, Rahman, Mohd Mezanur, Florius, and Nyoka Amy, for their assistance in data collection and specimen making. Their support and collaboration have been instrumental in the success of my research.

A special thank you goes to my husband and daughter for their understanding, love, and encouragement throughout this challenging journey. Their unwavering support has been a constant source of strength and motivation for me.

Lastly, I would like to thank all my friends, family, and well-wishers who have supported me in various ways, whether through moral support or kind gestures. Your encouragement has been a driving force behind my perseverance.

To all those mentioned above and countless others who have contributed to my Ph.D. research in one way or another, I extend my heartfelt gratitude. Without your support, this accomplishment would not have been possible. Thank you all for being an integral part of my academic and personal journey.

Lihong Mao

August 2023

ABSTRACT

An Integrated Algorithm for Automatic GPR Data Processing for Concrete Rebar Location

Lihong Mao

The University of Texas at Arlington, 2023

Supervising Professor: Dr. Nur Yazdani

Ground Penetrating Radar (GPR) has emerged as a valuable nondestructive testing technique for subsurface imaging and characterization in civil engineering applications. In particular, GPR plays a crucial role in the evaluation of reinforced concrete (RC) structures, enabling the determination of concrete cover thickness and the localization of reinforcement. However, the efficacy of GPR data analysis is often hindered by inherent challenges, including correction of time-zero position, unknown EM wave velocity, hyperbola picking, strong noise, and blurred signals. These challenges contribute to the complexity of achieving accurate and automated GPR data processing for rebar location.

This Ph.D. research aims to address these challenges and enhance the accuracy and efficiency of GPR data processing for RC structures. The research consists of three main chapters, each focusing on a specific aspect of GPR data analysis.

Chapter 2 presents a novel time-zero (TZ) correction method specifically designed for RC structures. The proposed approach involves the identification of the first negative peak in the direct wave as the temporary TZ, followed by the application of an adjusting value to obtain the true TZ.

This innovative approach results in more accurate depth measurements and facilitates reliable assessment of concrete infrastructure with GPR. GPR scanning of 32 RC specimens with different rebar depths, sizes, and spacings was conducted, leading to the determination of a specific adjusting value of 0.14299 ns. To validate the proposed method, lab tests were conducted confirming the accuracy and reliability of the proposed TZ correction method, opening new avenues for improved GPR data analysis in RC structures.

Chapter 3 introduces a nondestructive algorithm for accurately estimating GPR's electromagnetic wave velocity. The algorithm leverages hyperbolic fitting and travel-time analysis, offering a practical solution for velocity estimation without the need for core drilling. Various factors, such as subsurface media type, moisture content, temperature, and antenna frequency, affect GPR wave propagation velocity. Traditional methods for velocity estimation often rely on empirical models or assumptions, limiting their accuracy in complex subsurface conditions. In contrast, the proposed algorithm utilizes advanced techniques that account for the variation of wave velocity with depth and consider the effects of subsurface heterogeneity, resulting in more precise velocity estimation. Laboratory experiments successfully validated the algorithm's accuracy and robustness, demonstrating its potential to enhance subsurface imaging capabilities and improve data interpretation.

Chapter 4 presents a comprehensive data processing algorithm for rebar localization in RC structures. The automated algorithm addresses challenges such as unknown time-zero, strong noise, and blurred signals, which are common in GPR data. By eliminating the need for manual interpretation or rebar-picking, the algorithm achieves full automation, enhancing efficiency and accuracy in data processing. Additionally, the proposed algorithm corrects time-zero and calculates electromagnetic wave velocity without the requirement for core-drilling, further

streamlining the data processing workflow. Validation on various datasets, including lab-made reinforced concrete blocks, bridge decks, and a culvert, demonstrated promising performance in determining the rebar's location. Compared with existing methods, the proposed algorithm proved to be cost-effective, practical, and efficient, providing accurate and reliable rebar localization.

In conclusion, this Ph.D. research makes significant contributions to the GPR-based assessment of RC structures through the development of innovative TZ correction, velocity estimation, and rebar localization methods. The validated approaches improve the accuracy, reliability, and efficiency of GPR data processing, paving the way for more informed decision-making in civil engineering and geophysical applications. The proposed methods open avenues for further research, such as exploring noise reduction techniques, machine learning-based approaches, and real-time GPR data processing integration. Overall, this research empowers civil engineers and researchers with robust tools for effective GPR data analysis and structural assessment in concrete infrastructure evaluation scenarios.

Table of Contents

List of Figures

List of Tables

CHAPTER 1

INTRODUCTION

1.1 Background

Adequate concrete cover in reinforced concrete (RC) structures provides a barrier against corrosion and fire damage for the steel reinforcement. It also enables the rebar to be stressed without slipping. Having accurate information on the concrete cover and rebar location is essential to evaluate the performance of existing structures. However, quite a few of the old structures are missing their as-built plan [1]. Besides, improper concrete and rebar placement occurs during the construction of buildings and bridges. Measuring as-built concrete cover thicknesses and identifying rebar locations have been challenging problems. A non-destructive method for measuring concrete cover thickness, and for identification of rebar location will be very useful in closing this knowledge gap. While core drilling would provide ground-truth information on the concrete cover, it is destructive and time-consuming. In addition, this 'spot test' method cannot provide comprehensive information pertaining to horizontal location, depth, and spacing of reinforcement.

Among the variety of Non-destructive Evaluation (NDE) techniques, Ground Penetrating Radar (GPR) and Cover Meter are the equipment that can be used for the investigation of concrete cover thickness and identification of rebar location in the field test [2]. However, the efficiency and accuracy of the Cover Meter are affected greatly by various factors, such as the second layer of reinforcement, rebars that are parallel to the detected bar, and probe choice (deep or shallow) [3]. In addition, it is not efficient to use Cover Meter to measure the large area and complicated

reinforcement layout. In contrast, GPR offers a more pragmatic solution and is widely adopted in NDE practice.

GPR operates on Electromagnetic (EM)-based principles, utilizing high-frequency radio waves (usually in the range of 10 MHz to 2.6 GHz) to reveal subsurface characteristics. It consists of a power supply, two antennae (transmitting and receiving antenna), and a radargram (central unit). The transmitting antenna emits an EM pulse into the subsurface (Figure1- 1). When the EM pulse encounters any buried objects or any changes in subsurface material, it reflects back to the surface. The receiving antenna receives these return signals and records the corresponding variations. The detected subsurface image is interpreted and displayed on the radargram. The time taken by the reflected signals to travel back is measured, which is an indication of the depth and location of the interruption (buried object).

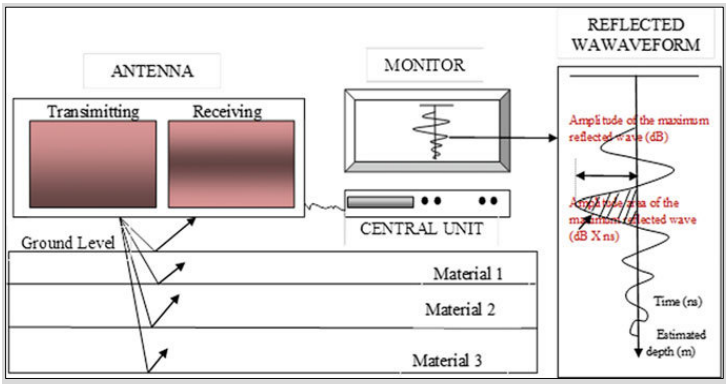

Figure1- 1. GPR working principle [4]

GPR was initially used in geophysics to investigate subsurface characteristics [4]. It was later adopted in civil engineering for cavity detection in airfields [5]. Subsequently, GPR was used to detect voids in concrete [6] and masonry structures [7], and delamination in concrete bridge decks [8]. It was also used to locate pipes [9], calculate the thicknesses of slabs or roads [10], determine the moisture content in concrete [11], and identify the reinforcement in concrete structures [12].

1.2 Problem Statement

GPR is increasingly used in the evaluation of the bridge deck condition and has been proven more effective than other equipment in measuring concrete cover thickness and identifying the location of rebar [13-15]. However, due to the existence of environmental noise, signal interference, and deficiencies of the GPR device, several challenges still need to be addressed in order to generate an accurate result in GPR data processing. These challenges are discussed as follows:

- **Time-zero estimation**

As shown in Figure1- 2, there is a small existing gap between the GPR antennae and the reinforced concrete surface. Time-zero exists because the recording of signals does not start until the direct wave (breakthrough signal) traveling along the air gap between the specimen surface and the GPR device reaches the receiving antenna (R).

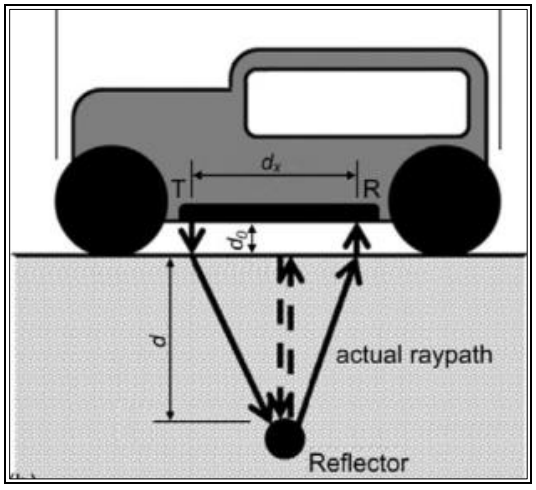

Figure1- 2. GPR device scanning the undersurface rebar

Therefore, the actual two-way travel time of the EM wave in the concrete can be described as in Eq. (1- 1):

$$t_a = t_g - t_0 \tag{1-1}$$

Where:

t_a = Actual two-way travel time of the EM wave in the concrete

t_g = Total time recorded by GPR

Considering the geometrical relation illustrated in Figure1- 2, the range of t_0 is presented in Eq. (1-2):

$$\frac{2\sqrt{\frac{d_x}{4} + {d_0}^2}}{v_a} < t_0 < \frac{d_0 + \sqrt{{d_x}^2 + {d_0}^2}}{v_a} \tag{1-2}$$

Where:

d_0 = Distance between the antenna and surface

v_a = EM wave velocity in the air

Conventionally, the time-zero position is placed at either the negative or the positive maximum peaks of the first wavelet. However, those peaks do not represent the true time-zero position. The true time-zero position still needs to be corrected in subsequent GPR data processing. As shown in Figure1- 3, the accurate setting of the time-zero position highly affects the actual EM wave two-way travel time. Consequently, it limits the accuracy of calculating the concrete cover thickness and identifying the rebar location.

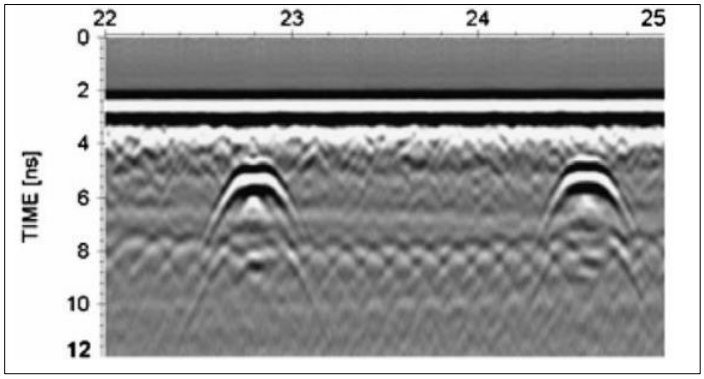

(a)

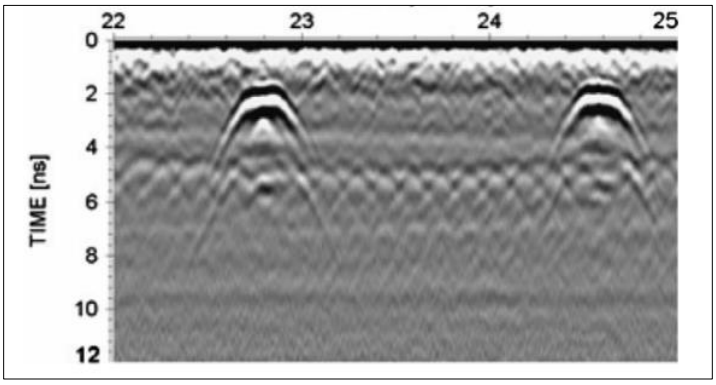

(b)

Figure1- 3. An example of a GPR image: (a) Before time-zero correction; (b) After time-zero correction [7]

- **The unknown EM wave velocity in the concrete**

To calculate the concrete cover thickness of rebars, the EM wave velocity in the concrete must be estimated. The relationship between concrete cover thickness, EM wave velocity in the concrete, and the EM wave two-way travel time is shown in Eq. (1-3).

$$C = \frac{v * t_a}{2} \tag{1-3}$$

Where:

C = Concrete cover thickness

The EM wave velocity in the concrete is affected by the dielectric constant of concrete. The relationship between EM wave velocity in the concrete and concrete dielectric constant is shown in Eq. (1-4).

$$v = \frac{c}{\sqrt{\epsilon}} \tag{1-4}$$

Where:

c = Speed of light in air

ϵ = Dielectric constant of concrete

Traditionally, core drilling is necessary for GPR application to estimate the concrete cover thickness. Multiple cores are drilled to measure the clear cover thickness. The true concrete cover thickness values are then used to back-calculate the actual concrete dielectric constant, which is used in the subsequent GPR data processing. However, this method is destructive, time-consuming, and not accurate because the dielectric constant at each core drilling point may differ.

- **The efficiency of GPR data processing**

Automatic object detection using GPR is a relatively new research area. Object locating through GPR data processing has been either done manually or by using commercial software. Depending on the size of the detection area and the complexity of the reinforcement layout, manually locating objects in a scan can be extremely time-consuming. When combined with the cost of GPR device and commercial software, these methods can easily limit the usage of the GPR technology. To move forward to a fully automatic solution for measuring concrete cover thickness and locating rebar, the primary concerns with modern methods are the accuracy of detection and the ability to perform automatic detection (automatic GPR data processing). The challenges that affect automatic data processing accuracy include the existence of background noise and blurry hyperbolic signals.

1.3 Objectives

This research involves laboratory testing, field testing, and MATLAB [16] coding to develop an integrated GPR data processing algorithm. It is a new and comprehensive method. It will improve the accuracy and efficiency of GPR data processing. The objectives of this research are:

- Correct the time-zero position.
- Find the EM wave velocity at every rebar location without drilling cores.

- Convert the time-zero and EM wave method into MATLAB [16] algorithm for better GPR data processing.
- Develop an integrated GPR image processing algorithm to automatically assess the rebar location, rebar spacing, and concrete cover thickness.
- Investigate the performance of the developed data processing algorithm.

The developed GPR data processing algorithm will be an integrated method, that addresses the challenges of time-zero position, EM wave estimation, and automatic data processing. Eventually, the GPR raw data will be processed more accurately and effectively by the proposed method.

1.4 Literature review

1.4.1 Time-zero

One of the most important steps in GPR application is the time-zero value correction. The setting of the time-zero location is highly related to the accuracy of determining the value of the two-way travel time. Consequently, it will greatly affect the accuracy of calculating the concrete cover thickness in the GPR data processing. Yelf et al. [17] examined the setting of the true time-zero position that both the GPR user and the equipment manufacturers use in reality. It is suggested that using a carefully calibrated time-zero value in advance of the first positive peak of the direct wavelet gives the most consistently accurate results for shallow depth estimates. In addition, it was also found that for a 1.5 GHz bow-tie antenna, the time-zero is located at 0.61 ns before the first positive peak in the direct wavelet. This is highly beneficial for predicting where the true time-zero occurs in the GPR application.

Assuming the buried object is located in the middle of the transmitting and receiving antenna. Clem et al. [14] proposed a new method to calculate the time-zero value. The proposed

approach considered electromagnetic wave (EM) propagation only parallel to the ground surface, and not any other paths. The time-zero is suggested as a fixed value and calculated by Eq. (1-5).

$$t_0 = \frac{d_x}{C_{air}} \tag{1-5}$$

Where:

t_0 = Time-zero value

C_{air} = EM wave velocity in the air

d_x = Distance between the receiving and the transmitting antenna (Figure1- 4)

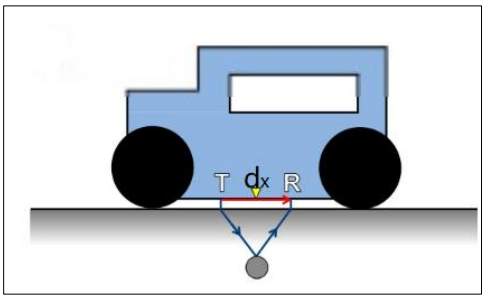

Figure1- 4. Elevation view of the antenna [18]

Agreed et al. [18] proposed to take advantage of using two receiving antennae in estimating the time-zero value. As illustrated in Figure1- 5, two receiving antennae were used, once the GPR profile had been achieved, immediately and without interruption of the recording, a measurement of the EM wave traveling in the air was made. This measurement was then used to estimate the time-zero value. However, this study considered the time that the EM wave traveled directly from the transmitting antenna to the receiving antenna as the time-zero value. The wave will likely hit the surface first and then reflect back to the receiver in reality. As shown in Figure1- 6, the EM wave travel paths 2 and 3 were also existing.

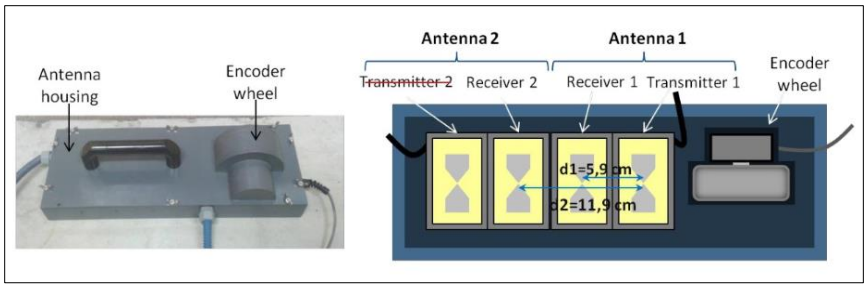

Figure1- 5. Box containing two antennae [18]

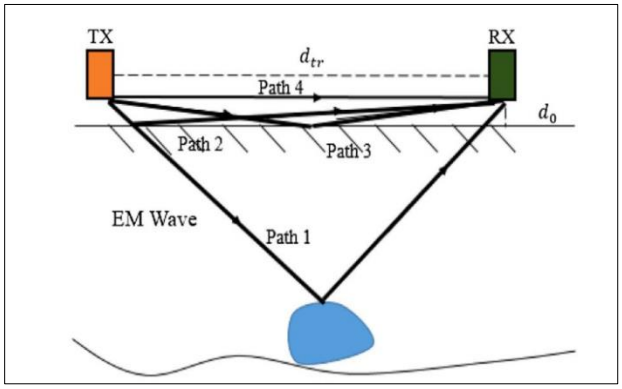

Figure1- 6. GPR EM wave travel path [20]

1.4.2 EM Wave Velocity

Besides the time-zero correction, the estimation of the EM wave velocity is another important process in GPR data processing. Traditionally, core drilling is required to measure the concrete cover thickness. Consequently, the EM wave velocity will be calculated by using the ground-truth concrete cover thickness. In Eq. (1-6), the relationship between the EM wave velocity and the thickness of the concrete cover is shown.

$$v = \frac{d}{t} \tag{1-6}$$

Where:

v = EM wave velocity in the concrete

d = Concrete cover thickness found by core drilling

t = EM wave travel time between the concrete surface and the buried rebar

However, because core drilling is destructive and time-consuming, the hyperbolic method in EM wave velocity estimation has become a non-destructive alternative. As shown by Laurens et al. [19], the shape of GPR hyperbolic signals, in the theoretical equation, is controlled by the EM wave velocity. Such velocity is affected by the water content, the concrete grade, the material distribution, and other factors.

Wiwatrojanagul et al. [20] proposed the use of an imaginary curve method to estimate the EM wave velocity in concrete. This method consists of drawing an imaginary curve that allocates the possible location of the reinforcement on the B-scan for each scan position. The curves are drawn by changing the estimated velocity of propagation. If all the curves obtained for different scans and a given velocity cross at the same point, this point corresponds to the position of the reinforcement, and that estimated velocity is the true EM wave velocity in the concrete. Wiwatrojanagul showed that the diameter of the object has no significant effect on concrete cover detection. The relative error is less than 5% for concrete cover thickness greater than 50 mm, whereas, for a smaller cover thickness (less than 25 mm), this error is approximately 15%. However, it is not a reliable method because the study estimated the time-zero before deciding the EM wave velocity.

1.4.3 Automatic GPR Data Processing

As for the automatic GPR data processing, a few attempts were made on extracting the information of rebar location from the raw GPR image. Dinh et al. [21] presented a new method to automatically pick rebars from the raw GPR image. The proposed approach is a deep learning-based software algorithm. It utilized GPR data processing methods like migration, normalized cross-correlation, and thresholding to extract the pixels from the hyperbolic signals. A trained

convolutional neural network (CNN) was then used to spot the peaks of the hyperboles. The authors claimed that the accuracy of GPR detection of rebar location improved significantly through the proposed method. However, this method involves a large amount of data in CNN training. Besides, the training data must be representative of the bridge decks that will be scanned. The neural network approach has been researched in another study. Al-Nuaimy et al. [22] employed an algorithm to automatically select the pixels which contain the locations of the buried objects from the GPR image. The study suggested using feature extraction and neural network classification to split up the GPR images. The segment that has information about the peaks of the hyperboles was then further processed by using edge detection and pattern recognition algorithms. However, the limitation is that sufficient representative data was required for the neural network training.

Krause et al. [23] applied the image segment method to detect the rebar location from GPR B-scan images. Different from the segmentation method used in Al-Nuaimy et al. [22], Krause proposed to separate the arcs of the GPR B-scan hyperboles. The arc which matches the hyperbolic shape the best was then recognized as the hyperbolic rebar signature by an arc detector. However, limitations still exist in this method. The accuracy improved by this method cannot be demonstrated in complicated GPR profiles which are common in GPR applications.

Gamba et al. [24] employed a new neural network method in underground pipe detection. The authors also employed some pre-processing steps before the neural network detector was applied. The purpose of these pre-processing steps was to improve the visibility of the GPR hyperbole signatures. However, the pipes detected in the article had bigger sizes and the layout is less complicated than rebars in a reinforced structure. Hence, this method has uncertainty for use in rebar detection.

A new neural network approach was proposed by Shaw et al. [12] to detect the rebar signatures. The edge detection process was used in the GPR image processing. The authors proposed to train and test the networks to find the hyperbolic rebar patterns using the detected edge lines. However, the concrete property used in the simulation is not continuous in the real situation, which can limit the improvement of accuracy. Besides, the GPR images used for validation were much less complicated than the real case; therefore, the proposed method remains uncertain for in-site application.

Pasolli et al. [25] proposed the use of a support vector machine (SVM) to automatically analyze GPR images. A pattern recognition algorithm was developed to first separate the GPR images into binary images, linear signatures, and hyperbolic signatures. Certain features were then used to extract linear and hyperbolic signatures from the binary images. SVM was finally used to categorize linear and hyperbolic shapes.

In a more recent study, the SVM classifier was presented by Kaur et al. [26] in an automatic rebar detection. In the first step, they suggested using an SVM classifier to locate the rebar region from GPR images. Then, a developed hyperbola-fitting algorithm was used to locate the peak within the region. The advantage of this method is to avoid using poorly performed data processing techniques, such as edge detection, thresholding, and template matching.

Similar to the method proposed by Kaur et al. [26], Gibb et al. [27] developed another machine learning-based algorithm to detect the rebar from GPR images. They suggested using Naïve Bayes classifier to approximately extract the images containing rebar signatures from GPR images. Then, a histogram maxima detection along with a local search was applied. The rebar locations were precisely identified as the peaks of the hyperboles in GPR images. Instead of using the hyperbola-fitting method proposed by Kaur et al. (25), they used a histogram localization

method to spot the point that has the highest pixel density. The hyperbolic signatures having low contrast can be detected more efficiently through this method.

However, among these data processing methods, the focus is all on finding the peaks in the GPR hyperbolas to represent the rebar location. The existing challenges in GPR data processing, such as time-zero correction, and EM wave velocity estimation still need to be addressed.

Kien Dinh et al. [21] presented a new methodology to automatically pick rebar from GPR signals. The proposed approach is a deep learning-based software algorithm. It utilized GPR signal processing methods like migration, normalized cross-correlation, and thresholding to extra the pixels from the hyperbole signals. A trained convolutional neural network (CNN) was then used to spot the peaks of the hyperboles. The author claimed that the accuracy of GPR detecting rebar location improved significantly through the proposed methods. However, this methodology involves a large amount of data in CNN training. Besides, those data have to be representative of the bridge decks that will be detected.

The neural network approach has been researched in another study. Al-Nuaimy et al. [22] employed an algorithm to automatically select the pixels which contain the location of the buried objects. The authors suggest using feature extraction and neural network classification to split up the GPR images. The segment that has information about the peaks of the hyperboles is then further processed using edge detection and pattern recognition algorithms. However, the same limitation presented in this approach is that enough representative data is required for the neural network training. Gamba and Lossani [24] employed neural networks in underground pipe detection. However, the authors proposed some pre-processing steps before the neural network detector was applied. The purpose of these pre-processing steps is to improve the visibility of the GPR hyperbole signatures. Another neural network approach was proposed by Shaw et al. [12] to detect

the rebar signatures. The edge detection process was used in image processing. The author proposes to train and test the networks to find the hyperbolic rebar patterns using the detected edge lines. However, the concrete property used in the simulation is not continuous in the real situation, which can limit the improvement of accuracy. Besides, the GPR images used for validation were much less complicated than the real case, therefore, the proposed methodology remains uncertain for in-site application.

The image segmentation method was applied by Krause et al. [23] to detect the rebar location from the GPR B-scan image. Different from the segmentation method used in Al-Nuaimy et al. [22] research, the authors proposed to separate the arcs of the GPR B-scan hyperboles. The arc which matches the hyperbolic shape the best is then recognized as the hyperbolic rebar signature by an arc detector. However, limitations still exist in this methodology. The accuracy improved by this method can't be demonstrated in complicated GPR profiles which is common in GPR applications.

Pasolli et al. [28] proposed to use of a support vector machine (SVM) to automatically analyze GPR images. A pattern recognition algorithm was developed to first separate the GPR images into binary images, linear and hyperbolic signatures. Certain features then are used to extract linear and hyperbolic signatures from the binary images. SVM was finally used to categorize linear and hyperbolic shapes.

In a more recent study [26], the support vector machine (SVM) classifier was presented in automatic rebar detection. In the first step, the authors suggest using an SVM classifier to locate the rebar region from the GPR scan image. Then, a developed hyperbola-fitting algorithm was used to locate the peaks within the region. The advantage of this methodology is avoiding using

poorly performed data process techniques, such as edge detection, thresholding, and template matching.

Similar to the methodology proposed in [26], Spencer Gibb et al. [27] developed another machine learning-based algorithm to detect the rebar from GPR images. The authors proposed to use Naïve Bayes classifier to approximately extra the images containing rebar signatures from the GPR scan. Then, a histogram maxima detection along with a local search was applied. The rebar location is precisely located as the peaks of the hyperboles. Instead of using the hyperbola-fitting method proposed in [26], the author used a histogram localization method that spots the point that has the highest pixel density. The hyperbolic signatures which have low contrast can be detected more efficiently through this methodology.

Magdalena Szymczyk et. al [29] presented a set of data processing techniques after raw data was produced by GPR. These basic procedures include editing, rubber-banding, dewow, time-zero correction, filtering, etc. Additionally, the other also described the automatic imaging processing techniques. Various 1D temporal filters and spatial filters are illustrated in this paper. This paper stresses the importance of choosing the proper processing technique. Moreover, the same scheme should be throughout the whole data processing procedure.

L. W. Galagedara et.al [30] proposed a method to calculate the GPR-time zero value. In the author's methodology, wave arrival time is automatically determined by picking the arrival time of the ground wave peak for fixed-offset data. The author suggests conducting a time-zero air wave calibration at both the beginning and the end station of a data set. Then by using those obtained data, a more accurate time-zero estimation should be produced. However, this method is only conducted in soil water content. It will be more valuable if reinforced concrete structures are tested.

The rebar size determination is the least reliability application of the GPR device. The estimation of EM wave velocity in concrete has been too. Aleksandar Vaso Ristic et. al [20] proposed a new approach to estimate cylindric object radius (R) and EM wave propagation velocity (V) from GPR. In the new method, the author suggested three steps. First, using the extracted raw data to find the hyperbola peak point (x_0, t_0), then the boundary speed v is calculated. Finally, v is refined to a more accurate value v_{min} . Although the methodology is not applied in RC structures, it is still valuable for estimating the rebar size (R) and EM wave velocity.

Traditionally, core drilling has been the common way to estimate EM wave velocity. Due to the increase requirement of non-destructive detection, the hyperbolic method to calculate EM wave velocity became popular. However, the accuracy of the hyperbolic velocity method highly depends on the method algorithm and raw GPR image. Jenet F.C. Sham et. al [31] proposed a new approach to estimate the EM wave velocity of GPR. The steps of this new method are the import of radargram, select suitable antenna frequency, set the region of interest (ROI) for locating the position of time zero in the direct wave, set the ROI for locating the position of the hyperbola signal from the reflector, set the desired standard deviation (SD) to eliminate the erroneous data. However, the new method was only applied in tests using a high-frequency antenna (2 GHz). If the author considered using various frequency antennae, the result will be more comprehensive and reliable.

Automated data processing for GPR has become more and more popular. However, there are a few fully developed automated algorithms to visualize the radargram. Kien Dinh et. al [32] developed a new algorithm that can both locate the rebar and detect the corrosive area in the concrete structure. This method is based on background removal, depth correction, and synthetic aperture of focusing technique (SAFT). Although the authors claimed the proposed method has

improved the accuracy of GPR data processing, the time consumed in the data training step is remarkable.

While most of the automated data processing approaches are based on the analysis of amplitudes of reflection, Tarussov et al. [33] argued that a visual interpretation by an experienced GPR analyst would provide much more accurate evaluations. To justify their claim, the authors pointed out three specific reasons. First, they view the GPR as an imaging device and not a measuring instrument. Second, they stated that a simple analysis of amplitude would ignore most information contained in the B-scans, and such an analysis can be affected by many factors, such as the rebar depth, surface anomalies, rebar configuration, polarization effects, etc. Finally, the authors explained the issue with the conventional method of contour mapping. According to them, as this method was based on interpolation, it was not suitable to map corroded areas, which usually had sharp limits in B-scans.

Hai Liu et al. [34] proposed an automatic detection and localization method using a Single Shot Multibox Detector (SSD) model and migration. However, the performance of this method highly depends on the dataset. Without appropriately adjusting the time zero position and calculating EM wave velocity, the accuracy of depth measurement is inefficient.

Maas et al. [35] proposed a GPR data process algorithm to only detect the presence of buried objects with high accuracy. Their method, like other neural network systems, requires training examples in similar environments and performance depends on the neural network structure. Moreover, these techniques fail in the presence of incomplete or highly disturbed profiles.

Another machine learning-driven approach proposed by Pasolli et al.[28] which includes utilizing Genetic Algorithm (GA) with Support Vector Machine (SVM) classifier for object detection and material recognition with 80% percent accuracy. Lu et. al [36] Proposed a new

algorithm for the automatic detection and material classification of buried objects with 92% accuracy using SVM after applying discrete wavelet transform (DWT) and fractional Fourier transforms (FRFT). Although the accuracy of the proposed method is high, the system is not fully automatic and does not provide a depth estimation which is of utmost importance in real applications. Qiao et al. [37] proposed a multi-stage process called the Multiresolution Monogenic Signal Analysis (MMSA) which detected targets and estimated their horizontal and vertical position with an average 5.8 cm distance error.

1.5 Dissertation Organization

The dissertation is organized as follows: Chapter 1 provides an introduction to the research, presenting the background, problem statement, and research objectives, followed by an extensive literature review. The main body of the dissertation consists of three papers: Chapter 2 introduces a novel GPR time-zero correction method for concrete structure evaluation, Chapter 3 describes a nondestructive method to calculate the EM wave velocity in concrete during depth measurement, and Chapter 4 presents a comprehensive algorithm for processing GPR data with full automation. The dissertation concludes with Chapter 5, where a summary of the research findings and their implications are discussed, followed by conclusive remarks.

CHAPTER 2

GROUND PENETRATING RADAR TIME ZERO CORRECTION FOR CONCRETE STRUCTURE EVALUATION

ABSTRACT

Ground penetrating radar (GPR) has been widely used for the Non-Destructive Evaluation (NDE) of reinforced concrete (RC) structures, especially for determining the concrete cover thickness and locating reinforcement. Accurate determination of these parameters is essential for maintenance and repair design. However, establishing an accurate time zero (TZ) position, which directly impacts the depth measurement accuracy, remains challenging. Existing methods for TZ correction lack accuracy and consensus. To overcome this limitation, this study proposed a novel approach by identifying the first negative peak in the direct wave as the temporary TZ position and then applying an adjusting value relative to this position. GPR scanning data from 32 RC samples with different rebar depths were used to come up with a -0.14299 ns adjustment value, locating the TZ position at 0.14299 ns ahead of the first negative peak. An antenna pulling-away test was conducted on a metal panel to validate the proposed approach, considering both the first positive and negative peaks as the temporary TZ and subsequently adjusting the real TZ. It was found that the adjusted TZ positions obtained from the two temporary TZ positions coincided, confirming the accuracy and reliability of the proposed approach. Due to the influence of subsurface material on the arrival time of the first positive and negative peaks, the calculated adjustment value is only applicable to RC structures.

Keywords: time zero, ground-penetrating, concrete, first negative peak, first positive peak

2.1 Introduction

Ground Penetrating Radar (GPR) is a widely used Non-Destructive Evaluation (NDE) technique for subsurface investigations, including the determination of concrete reinforcement cover and locations [38]. Accurate rebar placement and depth information are important for effective repair and maintenance of Reinforced Concrete (RC) buildings and bridges [33, 39, 40]. GPR offers several advantages over alternative approaches, including non-destructiveness, high resolution, and excellent measurement accuracy [41]. The GPR system typically consists of a radar control unit (radargram), a data acquisition system, and a transmitting and receiving antenna. It gathers subsurface data by employing high-frequency (10 to 3000 MHz) pulsed electromagnetic (EM) waves, often known as radar waves. The transmitting antenna emits an EM pulse into the subsurface. When the EM pulse encounters buried objects or changes in subsurface material, it reflects to the surface. The receiving antenna receives the returning signals and records the corresponding variations. The detected subsurface image is interpreted and displayed on the radargram. Measurement of the time the reflected signals take to travel back provides information about the depth and location of the interruption (e.g., embedded rebars in concrete) [42-45].

To ensure accurate depth measurements with GPR systems, a good assessment of the time the EM wave takes to travel from the transmitting antenna to the target and back to the receiving antenna is required. The time zero (TZ) position, serving as the time origin on radar measurements, is often assumed to be the moment when the direct wave, traveling from the transmitting antenna to the receiving antenna (Figure 2- 1), is collected by the antenna [46]. However, practical GPR applications involve a delay between the emission of the pulse by the transmitting antenna and the start of recording by the receiving antenna. Laurens [19] demonstrated that the arrival time of the direct wave varies and is not a valid time reference since it is affected by the moisture content of

the subsurface material. Therefore, the TZ position is an essential time reference that needs to be adjusted. Neglecting the proper TZ correction can significantly impact the two-way travel (TWT) time of the EM wave, leading to an error in the depth investigation of the buried objects.

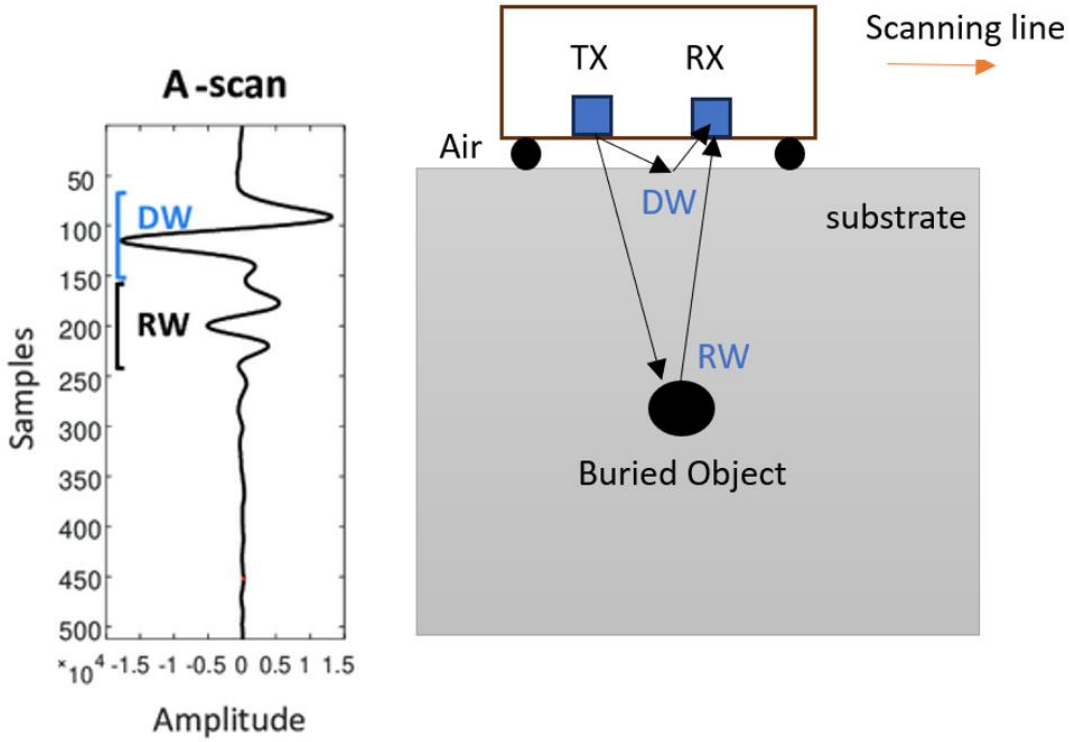

Figure 2- 1. Schematic diagram of the GPR signal

Most GPR manufacturers have TZ guidelines [47] specific to their systems. The need for TZ adjustment for GPR scans has been known for some time. Yelf [17] reported that the true TZ position is not a fixed value and is affected by the type of antenna, the height above the surface, and the moisture content of the substrate. Ernenwin [48] used the first break position of the direct wave as the TZ position, which is typically used in archeology where the ground is not too conductive and the depth of an object is not a major concern. Dinh et al. [8, 21, 32, 49, 50] proposed first finding the position of the first positive peak for all the GPR A-scans, and then calculating the average position of the first positive peak for the whole B-scan. The TZ position can be corrected by deleting all data before 0.61 ns of the average position of the first positive peak. Pongsak et al.

[51] suggested placing the TZ position for a 1.5 GHz antenna at 0.13 ns. Steinbeck et al. [52] compared pairwise and mesh calibration approaches by utilizing the ability of the monitoring system to conduct reciprocal measurements between any pair of antennae. The TZ position was calculated through a combination of pairwise and mesh calibrations. The former involves reciprocal measurements between individual antennae, while the latter combines reciprocal measurements from multiple transceivers. The calibration strategy considers the characteristics of the monitoring system and enables accurate measurements of signal propagation time between antennas in the absence of a known material for calibration. Zadhoush et al. [53] proposed using a realistic three-dimensional numerical model of a GPR transducer to generate a better process of TZ adjustment and time picking of the GPR wavelets.

Prior research on TZ corrections can be summarized as follows:

1. First-break picking: It involves identifying the first arrival of the radar signal from the subsurface corresponding to the reflection from the top layer. The time delay is used to correct the TZ that relies on accurately identifying the first arrival of the radar signal, which can be challenging in noisy or complex subsurface environments. Additionally, the first-break arrival time may not necessarily correspond to the true TZ position, particularly for multiple subsurface layers with different velocities.
2. Pulse stretching: It involves modifying the radar pulse shape to account for any distortions introduced by the antenna or cable delays. The pulse shape can be adjusted to match a reference signal, such as a synthetic pulse, to correct the TZ position. This method can be effective in correcting antenna ringing or cable delays. However, it can introduce additional noise or distortions in the radar signal and may also require extensive calibration or signal processing.

3. Waveform cross-correlation: This method involves comparing the recorded radar signal with a reference signal to determine the time delay. It requires a reference signal closely matching the recorded radar signal, which may not always be available. It can also be computationally intensive, particularly for large datasets or high-resolution imaging.

There is apparently a knowledge gap in the existing literature due to the limitations in the current approaches to the TZ correction for GPR scans and no consensus on any single method. It is possible that shallow wave reflections or near-field data can be deleted from the radargram or may not be seen if TZs are not correctly positioned, limiting the accuracy of exiting methods. The current study aims to plug this knowledge gap by proposing a more reliable and logical method for adjusting the GPR TZ position for RC structures.

2.2 Methodology

Figure 2- 2 illustrates the direct and reflected wave signals of the A-scan of a rebar with the horizontal and vertical axes corresponding to time and wave amplitude, respectively. The left box encloses the direct wave, while the right box is for the reflected wave. The two signals exhibited opposite polarities due to the shift in wave polarity caused by the reflection of a metallic medium. Times t_1, t_2, and t_3 represent the first positive peak in the direct wave, the negative peak of the direct wave, and the positive peak of the reflected wave, respectively. The signal TWT time between the scanning surface and rebar was calculated by measuring the time difference between the positive peak of the reflected wave and the temporary TZ.

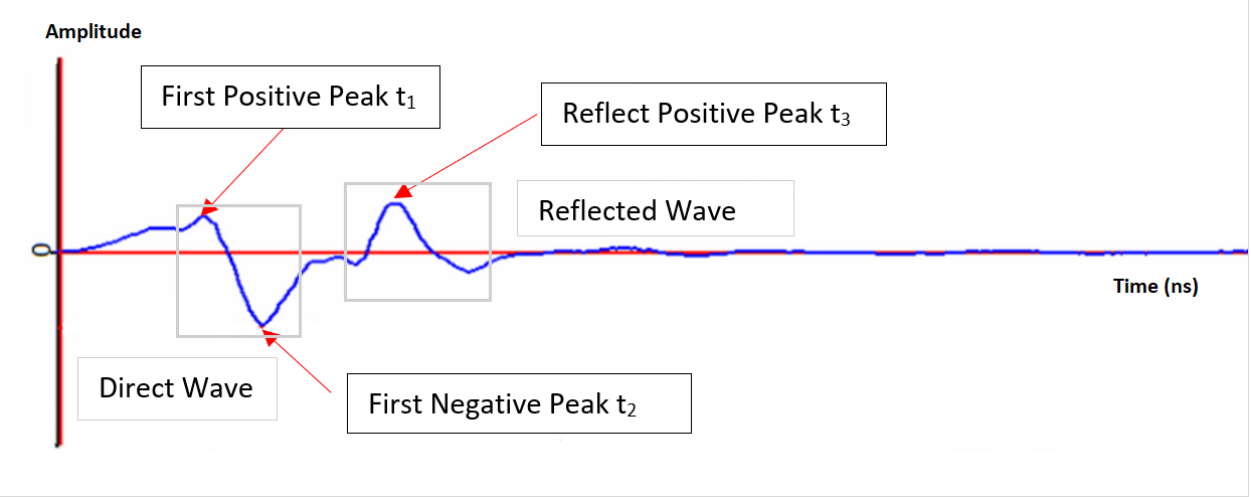

Figure 2- 2. A-scan of an embedded rebar

The proposed methodology (Figure 2- 3) included two main procedures: scanning RC specimens and conducting antenna pulling-away testing. The RC specimen testing, with the workflow depicted in Figure 2- 3 (a), involved scanning 32 samples with various rebar embedment depths. The first negative peak, denoted as t_2 in the direct wave, was used as the time reference. The signal travel time between the concrete surface and rebar was measured as the difference between t_3 and t_2. The travel distance corresponds to the signal path length from the concrete surface to the rebar and then reflects back to the concrete. Linear regression analysis was conducted on the plot of TWT distance versus travel time for each rebar size with variable depth. The slope of the regression line provided the EM wave velocity in the concrete specimen, while the intercept on the time axis offered the adjusting value for locating the true TZ position relative to the first negative peak of the direct wave, t_2. To compensate for the possible error in calculating the correct TZ position, the average intercept for each rebar size was used as the adjusting value.

In order to verify the proposed method, an antenna pulling-away test, with workflow shown in Figure 2- 3 (b), was conducted on a steel panel. Steel panel was chosen for its controlled interaction with GPR signals, well-defined electromagnetic properties, and stability. This ensured

the validation of the GPR system while minimizing interference and maintaining uniformity in the experiment. Figure 2- 4 shows the antenna pulled-away test. Similar to the RC specimens, GPR scanning of the steel panel was conducted to obtain the A-scans. The antenna was placed on a plastic box, which was later pulled away from the steel panel at different distances. The distance between the panel and the antenna requires no-overlapping of the direct wave with the reflected wave; hence the minimum distance was bigger than zero. The GPR antenna was pulled further away from a steel plate at distances of 50, 100, 150, 200, 250, and 300 mm (1.97, 3.94, 5.91, 7.87, 9.84 and 11.81 in.). As air is a simple and homogeneous media, the A-scan clearly contains the direct and the reflected waves. The radar images can be clean and easily interpreted, even though clutter due to unwanted targets can be detected. A careful interpretation considering this difficulty can provide information to calibrate an antenna [54]. The temporary TZ position was initially placed at the first positive peak, denoted as t_1 in the A-scan. A linearly best-fit trend line was then developed from the recorded TWT time and distance while putting the antenna at different distances. The intercept on the time axis represents the adjusting value for calibrating the TZ position in reference to the first positive peak. In this case, the signal travel velocity was known as 300 mm/ns due to the homogeneous nature of air. Next, the temporary TZ was set at the first negative peak, labeled as t_2 in the direct wave of the A-scan. Similar to the positive peak, TWT time and distance were calculated. Then, a linear regression graph of the TWT distance versus time data was generated. The time axis intercept was used to calibrate the TZ position with respect to the first negative peak. Comparing the location of the calibrated TZ using the first positive and negative peaks, they were found to coincide. It means that the location of the calibrated Temporary Zero (TZ) relative to the first negative peak aligns with the location of the calibrated TZ relative

to the first positive peak. This confirmed the accuracy of putting the temporary TZ position at the negative peak.

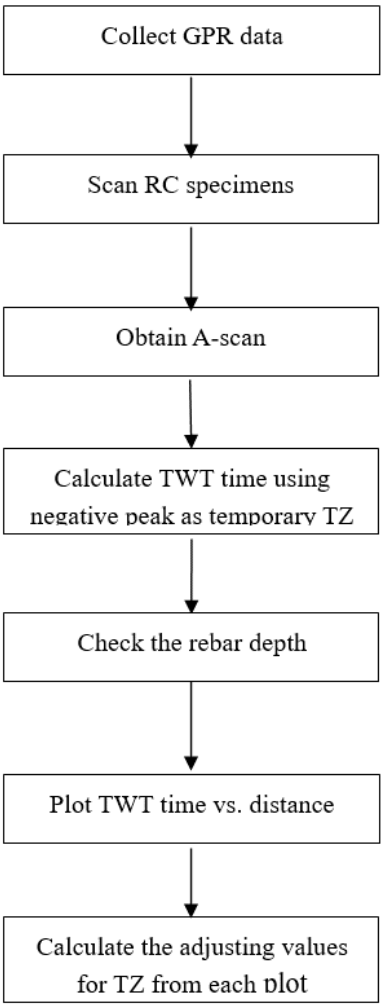

(a)

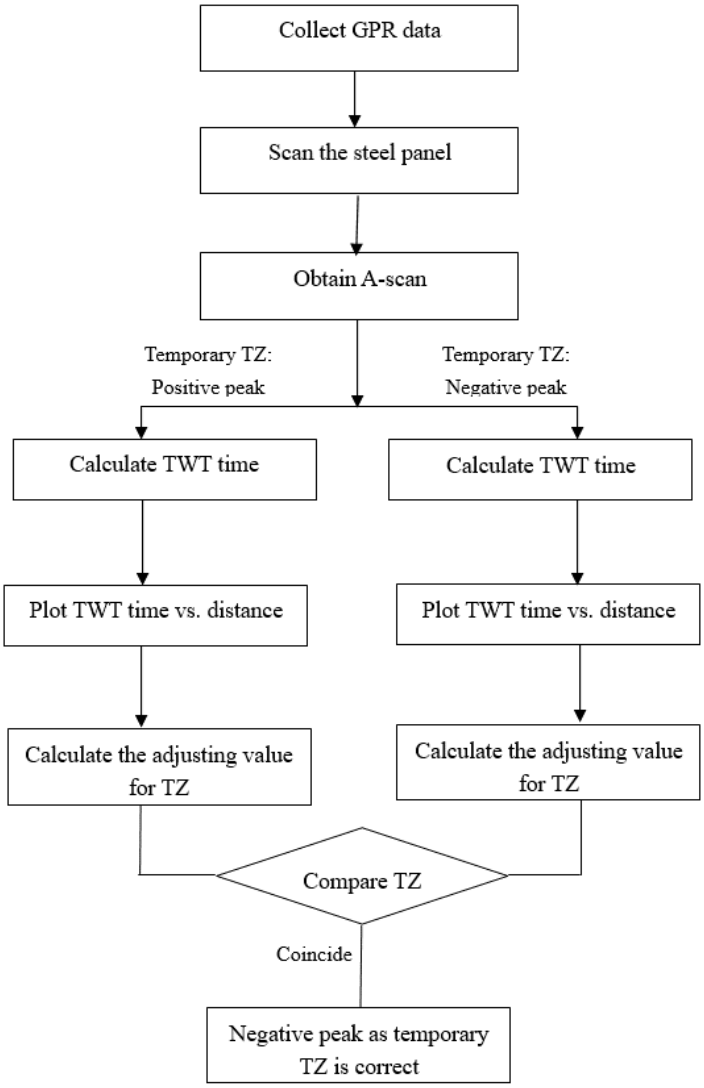

(b)

Figure 2- 3. Proposed methodology workflow: (a) RC sample scanning; (b) Antenna pulling away testing

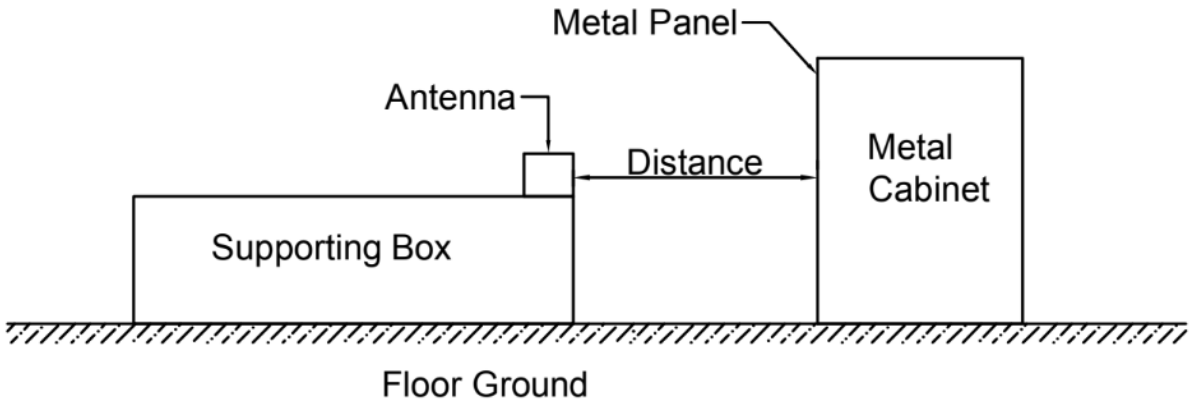

(a)

(b)

Figure 2- 4. Antenna pull-away test (a) Testing scheme; (b) Actual testing

Additionally, scanning of different surfaces was conducted to verify the material dependency of the values of the first positive and negative peaks. Consequently, the calculated adjusting TZ value in reference to the first negative peak was determined to be suitable for the RC structure surface.

2.2.1 Specimen design

To prevent GPR antenna footprint interference with reflections from the edges and bottom, RC specimens, each measuring 914 x 381 x 203 mm (36 x 15 x 8 in.), were selected as shown in Figure 2- 5. The dimensions allowed the GPR waveforms to capture two distinct signals, direct and reflected waves. A factorial design method was employed to determine the number of samples considering rebar depth, size, and spacing. Minitab statistical software was utilized, incorporating three degrees of freedom [55]. Concrete covers of 25, 38, 64, and 89 mm (1, 1.5, 2.5, and 3.5 in.) were considered to incorporate the most frequently used values specified in ACI 318-19 [56]. Rebar sizes of #3 to #11 were considered, encompassing commonly used sizes. The minimum rebar spacing requirement per ACI-318-19 [56] was taken into account to ensure proper concrete consolidation around the reinforcement. The minimum spacing was determined to be a maximum of 25 mm (1 in.), a bar diameter, or 1.33 times the maximum aggregate size. In addition, as-built plans for various structures, including RC slabs, bridge decks, and girders, showed a wide range of spacings, from 76 to 457 mm (3 to 18 in.). Therefore, rebar spacings of 76, 102, 127, and 179 mm (3, 4, 5, and 7 in.) were used for the specimens, as these are commonly used in RC structures. Table 2- 1 shows the rebar information for the 32 samples.

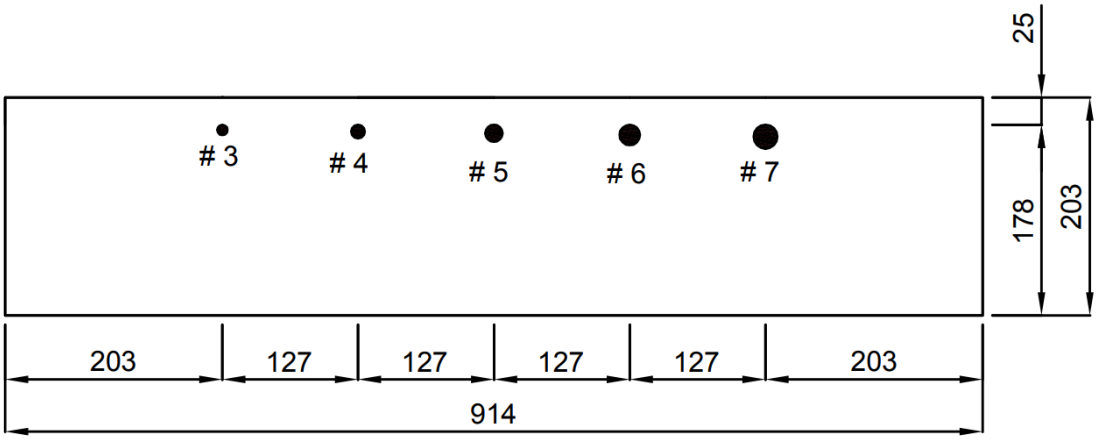

Figure 2- 5. RC specimens (All dimensions in mm)

Table 2- 1. Test matrix

Specimen number	Rebar cover mm (in.)	Rebar size	Rebar spacing mm (in.)
1	25 (1)	#3, #4, # 5, #6, #7	76 (3)
2	25 (1)	#8, #9, # 10, #11	76 (3)
3	38 (1.5)	#3, #4, # 5, #6, #7	76 (3)
4	38 (1.5)	#8, #9, # 10, #11	76 (3)
5	64 (2.5)	#3, #4, # 5, #6, #7	76 (3)
6	64 (2.5)	#8, #9, # 10, #11	76 (3)
7	89 (3.5)	#3, #4, # 5, #6, #7	76 (3)
8	89 (3.5)	#8, #9, # 10, #11	76 (3)
9	25 (1)	#3, #4, # 5, #6, #7	102 (4)
10	25 (1)	#8, #9, # 10, #11	102 (4)
11	38 (1.5)	#3, #4, # 5, #6, #7	102 (4)
12	38 (1.5)	#8, #9, # 10, #11	102 (4)
13	64 (2.5)	#3, #4, # 5, #6, #7	102 (4)
14	64 (2.5)	#8, #9, # 10, #11	102 (4)
15	89 (3.5)	#3, #4, # 5, #6, #7	102 (4)
16	89 (3.5)	#8, #9, # 10, #11	102 (4)
17	25 (1)	#3, #4, # 5, #6, #7	127 (5)
18	25 (1)	#8, #9, # 10, #11	127 (5)
19	38 (1.5)	#3, #4, # 5, #6, #7	127 (5)
20	38 (1.5)	#8, #9, # 10, #11	127 (5)
21	64 (2.5)	#3, #4, # 5, #6, #7	127 (5)
22	64 (2.5)	#8, #9, # 10, #11	127 (5)
23	89 (3.5)	#3, #4, # 5, #6, #7	127 (5)
24	89 (3.5)	#8, #9, # 10, #11	127 (5)
25	25 (1)	#3, #4, # 5, #6, #7	178 (7)
26	25 (1)	#8, #9, # 10, #11	178 (7)
27	38 (1.5)	#3, #4, # 5, #6, #7	178 (7)
28	38 (1.5)	#8, #9, # 10, #11	178 (7)
29	64 (2.5)	#3, #4, # 5, #6, #7	178 (7)
30	64 (2.5)	#8, #9, # 10, #11	178 (7)
31	89 (3.5)	#3, #4, # 5, #6, #7	178 (7)
32	89 (3.5)	#8, #9, # 10, #11	178 (7)

2.2.2 Specimen preparation

Normal strength concrete from a local ready-mixed supplier was used to cast the samples as it is the most commonly used in RC structures. Target compressive strength of 27.6 MPa (4

ksi), slump of 102 ±25 mm (4 ± 1 in.), and air content of 4.5% (± 1.5%) were selected. Detailed information on the concrete mix is shown in Table 2- 2.

Table 2- 2. Concrete mix design, per 0.765 m3 (1 cy)

Material	**Weight**
Type I Cement	205 kg (451 lb)
Class C Fly Ash	51 kg (113 lb)
Size #57 coarse Aggregate	839 kg (1850 lb)
Fine Aggregate (Bristol Sand)	145 kg (320 lb)
Fine Aggregate (Bridgeport sand)	436 kg (961 lb)
Water-reducing Admixture	13 kg (28 lb)
Air-entraining admixture	7.94 g (2.8 oz)
City Water	59 kg (120 lb)

A combination of plywood and lumber was used to construct the formworks, as shown in Figure 2- 6. Holes were drilled in the plywood to install the rebars at the prescribed depths. The specimens were vibrated and troweled during casting to ensure proper consolidation and finish, per ASTM C-31 [57] (Figure 2- 6). After finishing, a curing compound was applied to each specimen and protected from direct sunlight to prevent moisture loss. Concrete cylinder specimens per ASTM C39 [57] were prepared to verify the target compressive strength.

(a)

(b)

(c)

Figure 2- 6. Samples preparation: (a) Formwork with rebars; (b) Concrete casting

2.2.3 GPR scanning of RC specimens

SIR-30 ground-coupled 2.6 GHz high-frequency GPR antenna was used for this study (Figure 2- 7). The 2.6 GHz central frequency is appropriate for shallow-depth concrete investigation, usually in the range of 0 to 305 mm (0 to 12 in.). The offset between the transmitting and the receiving antennas is 39 mm, as shown in Figure 2- 7. To ensure a straight scanning path along the length, two survey lines were marked on the surface of the samples, as depicted in Figure 2- 8. The antenna was then rolled along these two lines during the scanning process.

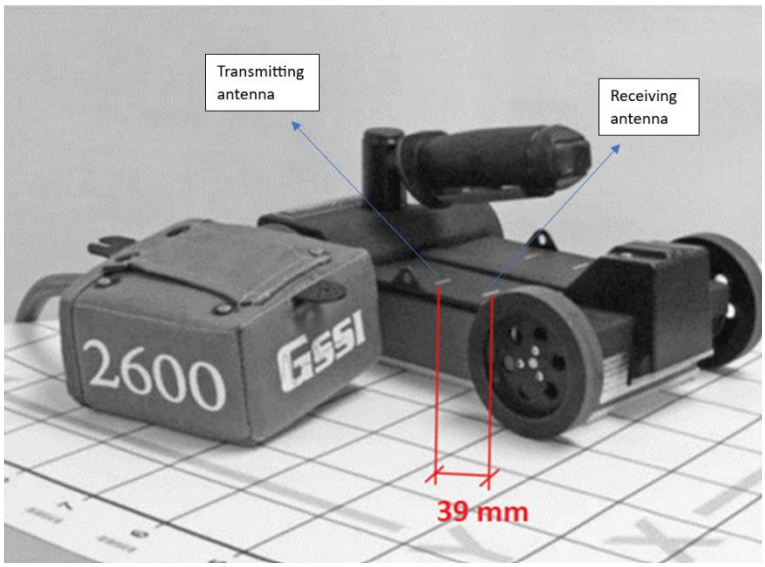

Figure 2- 7. 2.6 GHz GPR antenna

Figure 2- 8. RC specimen scanning

2.2.3 Scanning of different material surfaces

In this laboratory test, wood, plastic, and concrete surfaces were scanned using the SIR-30 antenna (Figure 2- 9), and their respective first positive and negative peak values were recorded. Subsequently, the time difference between the first positive peak and the first negative peak was calculated for each material.

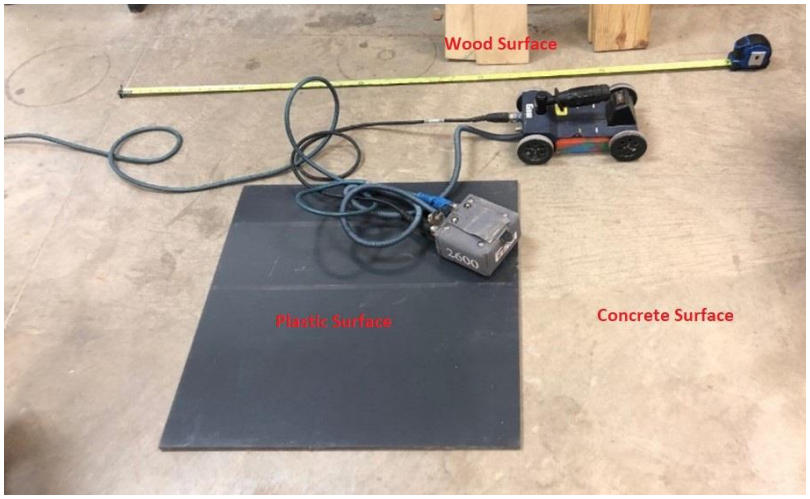

Figure 2- 9. GPR scanning of concrete, plastic, and wood surfaces

2.3 Result and Discussion

2.3.1 RC specimen scanning

Figure 2- 10 shows the plots of TWT distance versus the best fit linear trend lines for samples with rebar sizes #3 to #11 at different cover depths and the corresponding TZ positions. As demonstrated in Figure 2- 10 (a) to 11(i), the EM wave velocity remained mostly stable at around 95 mm/ns. The velocity variation depends on moisture content, concrete composition, porosity, and density. Generally, the velocity of EM waves in concrete falls within a range of 55 to 112 mm/ns [58]. All plots had an excellent coefficient of determination, R^2, ranging from 0.9930 to 0.9973. This implied that the linear regression model efficiently captured the variation in the data. The intercept in the horizontal time axis, where TWT time equals zero, represents the real-

time origin or the TZ position. Hence, the intercept value is used to accurately locate the TZ position in reference to the first negative peak of the direct wave. Ranges of intercept values from different samples and depths were obtained, reflecting the variations in the arrival time of the EM wave at the TZ position. The average of the intercept values was calculated to ensure a representative TZ position adjustment value. This helps mitigate potential outliers or unforeseen measurement errors that may occur in individual samples. The intercept values from each graph are summarized in Table 2- 3, resulting in an average of -0.14299 ns. This average value adjusts the TZ position slightly before the first negative peak, ensuring precise TWT time determination and subsequent accurate depth measurement.

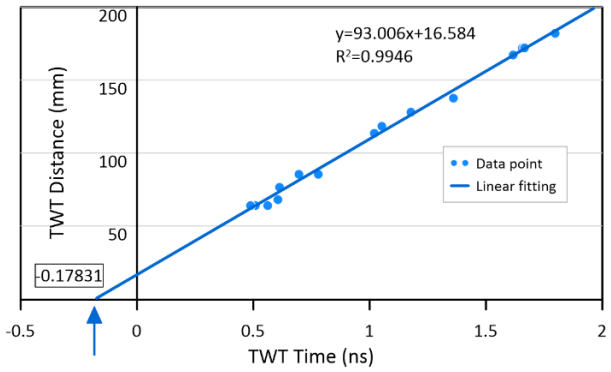

(a)

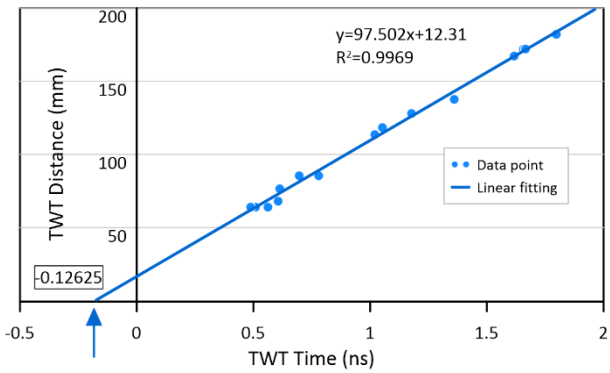

(b)

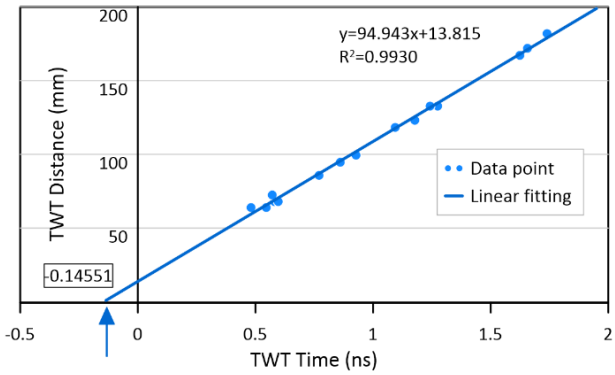

(c)

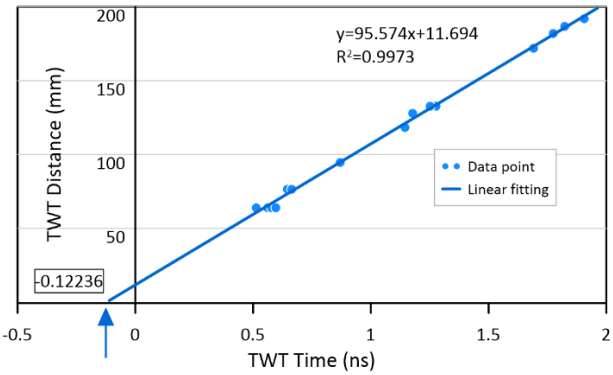

(d)

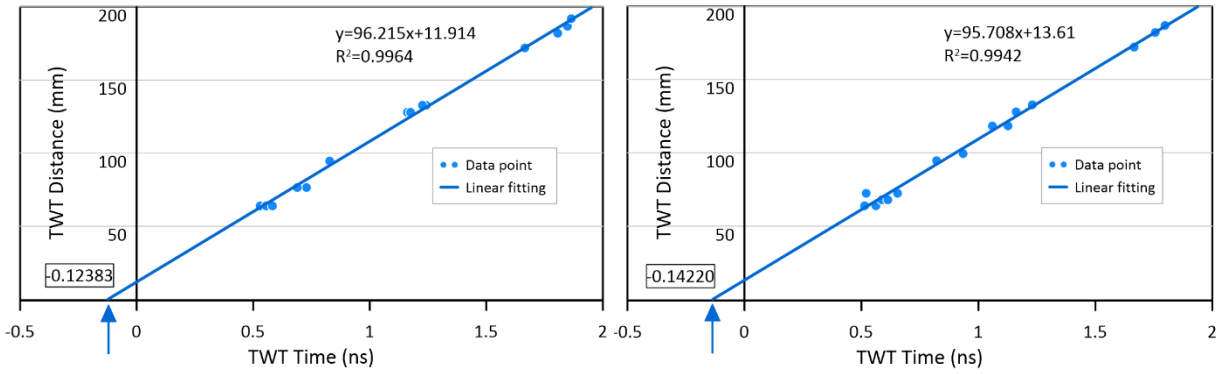

(e) (f)

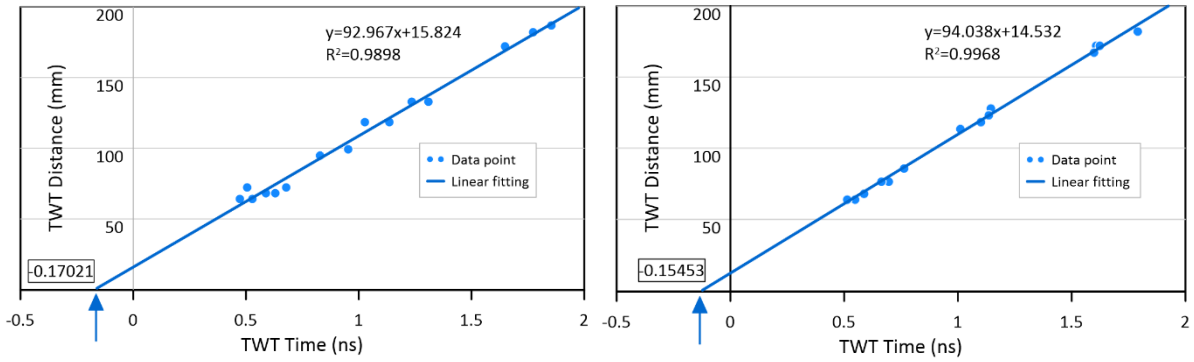

(g) (h)

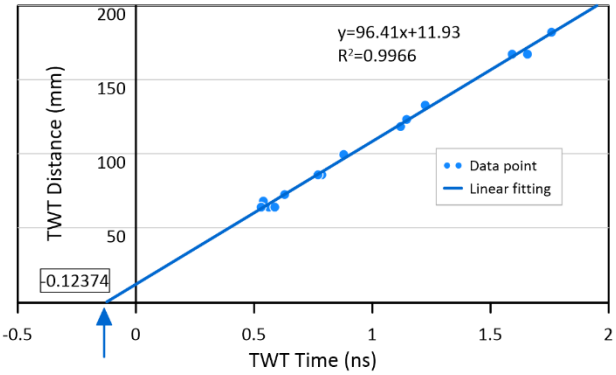

(i)

Figure 2- 10. TWT distance vs. time plots: (a) #3; (b) #4; (c) #5; (d) #6; (e) #7; (f) #8; (g) #9; (h) #10; (i) #11

Table 2- 3. Adjusted values for true Time Zero

Rebar	TZ to the first negative peak (ns)
#3	-0.178311077
#4	-0.12625382
#5	-0.145508358
#6	-0.122360573
#7	-0.123826846
#8	-0.142203369
#9	-0.170210935
#10	-0.154533274
#11	-0.12374235
	-0.14299

2.3.2 Antenna pulling away test

The TWT time versus distance plot for temporary TZ placed at the first positive peak is shown in Figure 2- 11.TWT time vs. distance with the first positive peak as reference point. Linear fitting was employed due to the assumption of a constant EM wave velocity, which corresponds to the gradient of the graph. The 300.84 mm/ns trend line slope agrees with the fact that EM wave travels at 300 mm/ns in air. The R^2 value of 0.9992 demonstrated an excellent fit of the collected data point to the best-fit line. The time axis intercept shows that the TZ position is 0.131123 ns behind the first positive peak, verified by several studies [14, 51, 59]. Therefore, the true TZ position for the antenna pulling way test may be considered as 0.131123 ns behind the first positive peak.

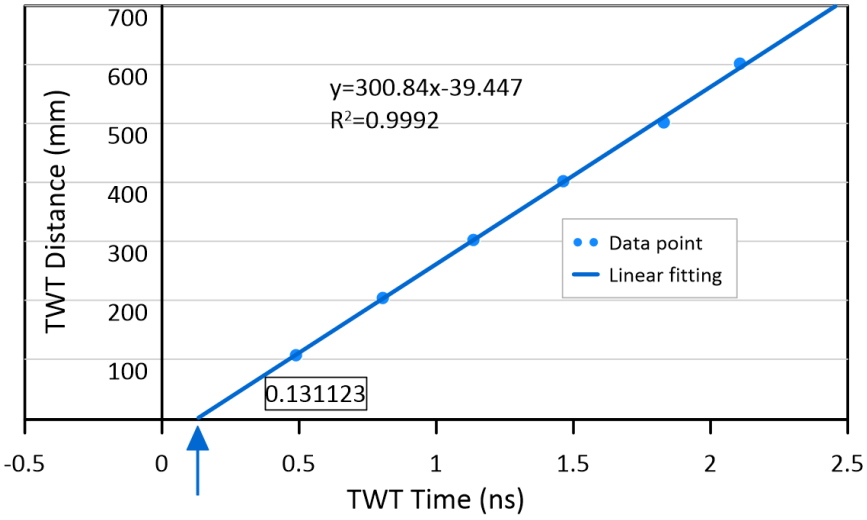

Figure 2- 11.TWT time vs. distance with the first positive peak as reference point

The TWT time versus distance plot, when the time origin was placed at the first negative peak, is shown in Figure 2- 12. TWT time vs. distance with the negative peak as reference point. The linear regression trend line shows that the calculated EM velocity in air is 299.18 mm/ns, closely matching the 300 mm/ns expected value. The adjusted TZ value is 0.17831 ns ahead of the first negative peak, corresponding to the true TZ position in the A-scan. The difference between the first positive and negative is 0.308 ns as shown in Table 2- 1. Hence, the proposed method of using the first negative peak as the temporary time origin is verified.

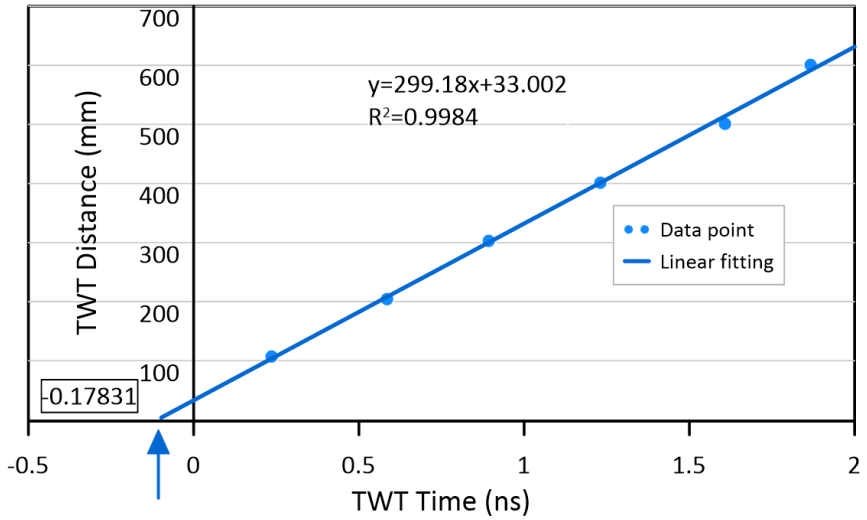

Figure 2- 12. TWT time vs. distance with the negative peak as reference point

Table 2- 4. First positive and negative peaks for different materials

Material	A-scan first positive peak in the time axis (ns)	A-scan first negative peak in the time axis (ns)
Concrete	0.785	1.105
Plastic	0.781	1.014
Wood	0.680	1.233
Steel	0.805	1.113

2.3.3 Scanning of different materials

Table 2- 1 summarizes the scanning results of concrete, plastic, wood and steel surfaces. The test verified that the first positive and negative peaks and the difference between the two points depend on the surface materials. It is noted that calibrated TZ with respect to the first negative peak is not a fixed value for different material surfaces. However, the -0.14299 ns value generated from this research is suitable for RC structures.

2.4 Conclusion

The following conclusions can be made based on the findings from this study:

1) This research presented a novel TZ correction method for RC structures application. It involved identifying the first negative peak in the direct wave as the temporary TZ and then applying an adjusting value in regard to this position to obtain the true TZ. This approach enables more accurate depth measurements and facilitates reliable assessment of concrete infrastructure with GPR.
2) The specific adjusting value for RC structures using the proposed method was obtained through GPR scanning of 32 RC specimens with different rebar depths, sizes, and spacings. From the data analysis, a 0.14299 ns adjustment value ahead of the first negative GPR wave peak was determined.

3) To validate the proposed approach, an antenna pulling-away test was conducted on a metal panel which entailed considering both the first positive and negative peaks as the temporary TZ and adjusting the real TZ accordingly. It was found that the adjusted TZ positions obtained from the two temporary TZ positions coincided, confirming the accuracy and reliability of the proposed approach.
4) Additionally, the study explored the behavior of the first positive and negative peaks on different material surfaces using the same GPR configuration. The results indicated that the positions of these peaks and their differences depend on the surface materials. Therefore, it can be concluded that the adjusting value with respect to the first negative peak is not a fixed value for different material surfaces.

In conclusion, this research provides a significant contribution to the GPR-based assessment of concrete structures through the development of an innovative TZ correction method. The validated approach improves the accuracy and reliability of depth measurements in GPR data analysis. These findings open an avenue for further research and encourage the application of the proposed method in various concrete infrastructure evaluation scenarios.

2.5 Limitation

The approach presented in this research assumes relatively equal water content in all the samples since they were made of the same concrete mix and subjected to the same curing condition. However, in reality, the water content in concrete varies. Thus, the effect of water content on TZ correction should be investigated. The type of subsurface material affects the first negative and positive peaks' arrival time; hence, the -0.14299 ns adjusting value only applies to RC structures. However, the proposed methodology in this research could be used for determining the TZ corrections for other materials.

CHAPTER 3

A Nondestructive Method to Estimate GPR Propagation Velocity

ABSTRACT

Ground Penetrating Radar (GPR) is a widely used nondestructive testing technique for subsurface imaging and characterization. Accurate estimation of the GPR propagation velocity is crucial for interpreting radar signals and obtaining accurate depth measurements. However, existing methods for velocity estimation in GPR are often limited by the reliance on empirical models or assumptions, which may lead to inaccuracies in complex subsurface conditions. This paper presents a nondestructive method for estimating GPR propagation velocity based on the analysis of hyperbolic fitting and travel-time analysis. The proposed method is validated through laboratory experiments, demonstrating its effectiveness in estimating propagation velocity with high precision. The results indicate that the proposed method offers a practical and reliable solution for GPR practitioners to enhance subsurface imaging capabilities and improve data interpretation.

Keywords: Ground-penetrating radar (GPR), propagation velocity estimation, nondestructive testing, hyperbolic fitting, travel-time analysis.

3.1 Introduction

Ground Penetrating Radar (GPR) is a valuable non-destructive geophysical tool used in subsurface investigations for infrastructure condition assessment, as well as for geophysics, environmental studies, and archaeology [12, 60-63]. It provides valuable information about the internal structures and properties of materials, such as concrete, soil, and pavement. GPR works by emitting electromagnetic waves into the subsurface and detecting the reflected signals to construct a detailed image of subsurface structures and properties (Figure 1)[64]. One of the critical

parameters in GPR data analysis is the electromagnetic wave velocity, which affects the depth and location calculation of subsurface features. Accurate estimation of GPR propagation velocity is crucial as it directly impacts the interpretation of radar data and the accuracy of subsurface imaging.

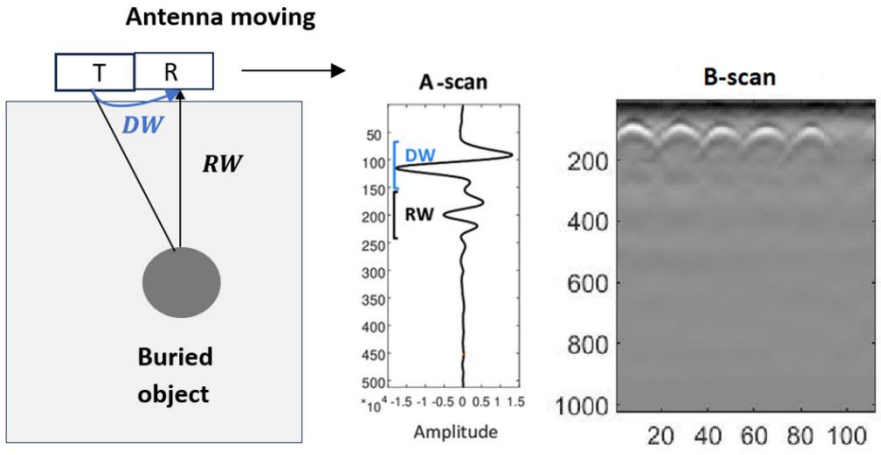

Figure 3- 1. GPR working principle

Several factors affect GPR propagation velocity [65, 66], including the soil type, material and Different soil types have varying electrical properties, such as permittivity and conductivity, which influence the propagation velocity of GPR waves. Materials with higher electrical conductivity tend to slow down the radar waves, while those with higher permittivity accelerate them. Second, the moisture content. The moisture content in the subsurface can significantly impact GPR propagation velocity. Moisture affects the dielectric properties of the material, altering its permittivity and conductivity and, consequently, the speed of radar waves. Moist soils with higher moisture content tend to exhibit reduced propagation velocities [67-70]. Third, temperature. Temperature variations in the subsurface can influence the propagation velocity of GPR waves. Temperature changes affect the dielectric properties of materials, causing variations in their permittivity and conductivity and, thus, impacting the radar wave speed. Last, is the antenna frequency. The frequency of the GPR system used for data collection also affects

propagation velocity. Higher frequencies tend to result in shorter wavelengths and increased resolution but are more sensitive to subsurface variations. The propagation velocity is inversely related to frequency, meaning that higher frequencies generally result in slower radar wave speeds.

Traditionally, GPR propagation velocity estimation has relied on empirical models or assumptions, but their accuracy is often limited due to the complex nature of subsurface conditions mentioned above. To overcome this limitation, there is a growing need for an automated and robust algorithm that can provide accurate velocity estimation, enabling practitioners to obtain more reliable subsurface information. Several studies have explored different approaches for estimating GPR wave velocity.

Similar to migration in the domain of seismic techniques, Anxue et al. [71] present an approach to focus on GPR data and estimate the electromagnetic wave velocity underground. Lin et. al [72] study the estimation of underground electromagnetic wave velocity based on characteristics of shallow-buried small target echo. The traditional estimation of underground electromagnetic wave transmission velocity adopts the method of measuring the dielectric constant. A validation study was conducted by Lai et. al [73] over a fixed alignment of underground utilities to study the effects of GPR traverse directions on the GPR wave velocity estimation of utilities. Delf et. al [74] present an automated workflow to estimate an englacial radar velocity field from zero offset data and apply the algorithm to GPR data collected on Von Postbreen, a polythermal glacier in Svalbard, using a 25 MHz zero-offset GPR system. At present, there is a lack of such a relationship for active-layer soil moisture estimation for the Qinghai–Tibet plateau permafrost regions. Lau et. al [75] propose a combination of velocity algorithms for the estimation of velocity, followed by characterizing water leak location where wave velocity is reduced compared to non-leak location, without prior information of utility depth. Liu et. al [76] use a 1-GHz GPR system

to measure the travel times for direct and reflected waves for computing the EM wave velocity. The development of a new algorithm to estimate EM wave propagation velocity (v) with a shielded GPR antenna with a high frequency of 2 GHz is presented by sham et. al [31]. Nguyen et. al [77] study determining velocities in a high-frequency electromagnetic prospecting by phase shift plus interpolation migration. The problem of how to apply PSPI Migration to interpret GPR data will be presented. Nguyen et. al [78] are also going to present two processing steps to define the electromagnetic wave velocity and the position of the object from GPR data that was acquired by using a shield antenna machine prototype. Perroud et. al [79] describe the use of the common-reflection-surface (CRS) method to estimate velocities from ground-penetrating radar (GPR) data. Ristic et.al [20] present a new method to simultaneously estimate cylindrical object radius and EM wave propagation velocity (v) from GPR data. Weifeng et. al [80] study the estimation of the GPR wave velocity based on template matching. A new GPR wave velocity estimation method is proposed based on template matching. Wijewardana et. al [81] focus on the estimation of spatiotemporal variability of volumetric soil water content in raised bed agricultural fields using GPR, comparison of the GPR method with gravimetric sampling data, and development of 2D maps of water content. Liu et.al [82] study dynamic groundwater level estimation by the velocity spectrum analysis of GPR. A new algorithm that involves envelope velocity spectrum and an automatic velocity picking scheme was proposed. The purpose of Pue et. al [83] is to evaluate the velocity semblance analysis technique for air-coupled common midpoint (CMP) measurements with a small antenna offset. In order to improve the resolution of GPR profiles from the perspective of data processing, the migration technique is applied to forward and measured GPR profiles [84]. Yuan et. al [85] apply a diffraction imaging method to improve imaging for surface reflection GPR data. At present, there is a lack of such a relationship for active-layer soil moisture estimation for

the Qinghai–Tibet plateau permafrost regions. Du et. al [86] utilize the Complex Refractive Index Model to establish such a calibration equation that is suitable for active-layer soil moisture estimation with GPR velocity. Other influential works include the work of Huggernberger et. al [87].

Those methods mentioned above involve manual picking of arrival times or curve fitting, which are subjective and prone to errors. Researchers have also investigated waveform analysis, frequency-domain techniques, and migration methods to improve the accuracy of velocity estimation. However, these approaches can be computationally intensive and may not be well-suited for real-time applications. In recent years, machine learning techniques, such as neural networks and support vector machines, have shown promise in GPR velocity estimation. Nevertheless, these methods often require large training datasets and depend on the availability of labeled data, which can be a limitation. To address these challenges, this research presents a novel nondestructive method for estimating GPR propagation velocity. The proposed method relies on hyperbolic fitting and travel-time analysis, leveraging the characteristics of GPR waveforms and their relationship with the subsurface. The hyperbolic fitting technique enables the modeling of the relationship between arrival times and offsets, providing a robust estimation of the wave velocity. Additionally, travel-time analysis techniques account for the variation of wave velocity with depth and consider the effects of subsurface heterogeneity, further enhancing the accuracy of velocity estimation. Through the integration of these advanced techniques, the proposed algorithm presents a reliable and accurate solution for the estimation of GPR wave velocity. The effectiveness of the algorithm, as well as its capability to enhance subsurface imaging and improve data interpretation, has been successfully validated through a laboratory experiment.

3.2 Methodology

This research proposes a nondestructive method in GPR velocity estimation, contributing to the broader field of non-destructive evaluation and providing valuable insights for subsurface characterization. The proposed algorithm consists of the following steps:

1. Data Preprocessing: Raw GPR data is preprocessed to remove noise, filter unwanted frequencies, and enhance the signal-to-noise ratio. This step improves the quality of the data and ensures reliable velocity estimation.
2. Hyperbolic Fitting: A hyperbolic curve fitting technique is applied to the preprocessed data. By fitting a hyperbolic curve to the arrival times and corresponding offsets, the peak coordinates of each hyperbola can be obtained for further velocity analysis.
3. Travel-Time Analysis: Travel-time analysis is performed to account for the variation of wave velocity with depth and the effects of subsurface heterogeneity. This analysis refines the velocity estimation and provides a more accurate estimation of the wave velocity.
4. Validation and Calibration: The estimated wave velocity is compared with reference values obtained from known subsurface features or calibration targets. This validation step ensures the accuracy and reliability of the algorithm.

Through laboratory experiments and field measurements, the proposed algorithm's performance is assessed, and its effectiveness in estimating GPR's electromagnetic wave velocity is validated. The results demonstrate the algorithm's capability to provide accurate and reliable velocity estimation.

Hyperbola fitting

Artificial neural networks, which treat radargrams as images, can be used to detect hyperbolas. Object detection in radargrams is often accomplished using machine learning and deep

learning approaches [34, 88]. For hyperbola identification, several networks are commonly employed, including regions with convolutional neural work (R-CNN) [89, 90], Faster R-CNN [91], Cascade R-CNN [92], Single shot multi-box detector (SSD) [93], You Only Look Once (YOLO) [94], and RetinaNet [95]. These networks can be constructed using deep learning frameworks like Python or MATLAB's Deep Learning toolbox. To address the challenge of acquiring a large number of images for training, pre-trained models can be utilized in transfer learning, adapting the model specifically for hyperbola detection in radargrams.

Once the hyperbolas are detected, the hyperbolic curve can be fitted in each hyperbola reflection in the radargram by extracting attributes that characterize hyperbolic signatures and distinguishing them from other undesired backgrounds. In a GPR image, the detected hyperbolae are manifested as “south-opening” branches, given by Eq. 3-1. Figure 3- 2 (a) and (b) show the hyperbola reflections and the hyperbola with the fitted curve, respectively.

$$\left(\frac{y-y_0}{a^2}\right)^2 - \left(\frac{x-x_0}{b^2}\right)^2 = 1, \text{ with } y < 0 \qquad (3\text{-}1)$$

Where:

y = Two-way travel time of the EM waves

x = Distance along the measured direction

(x_0, y_0) = Center of the hyperbola

a = Length of the semi-major axis

b = Length of semi-minor axis

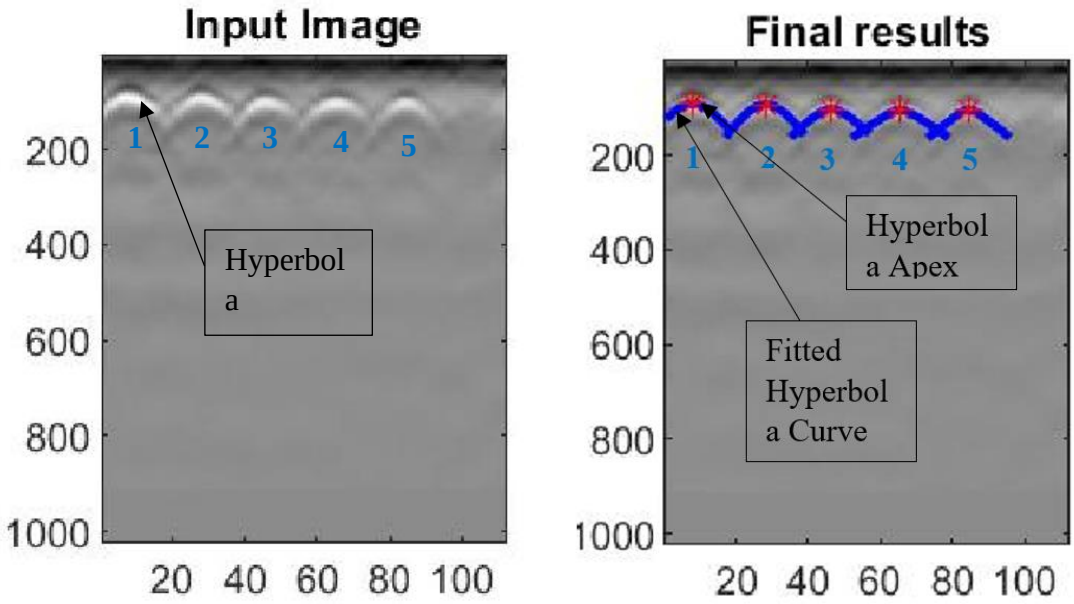

Figure 3- 2. Radar scan: (a)Images with original hyperbolas; (b) Fitted hyperbolas

Travel time analysis

Figure 3- 3 (a) shows a GPR hyperbolic reflection from the location of a buried object. Point (x_0, t_0) is the coordinate at the peak hyperbolic reflection from the buried object. The points (x_i, t_i) are the extracted points from the first positive peak amplitude of the hyperbolic pattern from the buried object, the signal travel path for those points is demonstrated in Figure 3- 3 (b).

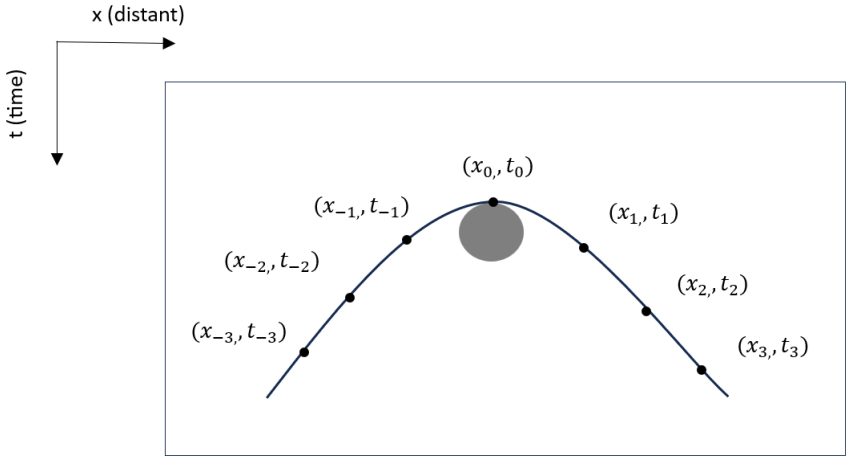

(a)

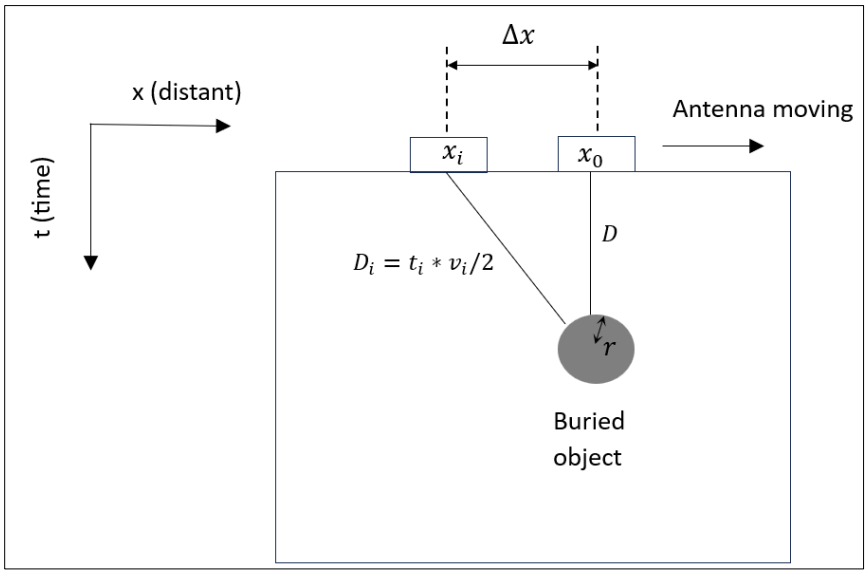

(b)

Figure 3- 3. Hyperbolic reflection of a buried object: (a) Hyperbola curve with the extracted points; (b) Signal ravel path

The right triangle with sizes D, D_i, and Δx in Figure 3 (b) can be described as Eq. (3-2)

$$D_i{}^2 = D^2 + \Delta x^2 \tag{3-2}$$

Where:

D_i = Distance between the antenna at x_i position and the buried object

D = Distance between the antenna at x_0 position and the buried object

Δx = Horizontal distance between antennas at x_0 and x_i position

r = Radius of the buried object

Based on the meaning of D, D_i, and Δx, Eq. (3-2) also can be written as Eq. (3-3).

$$\left(\frac{v_i * t_i}{2} + r\right)^2 = \left(\frac{v_0 * t_0}{2} + r\right)^2 + (x_i - x_0)^2 \tag{3-3}$$

Where:

t_i = Actual two-way travel time (after time-zero correction) between the antenna and the buried object at the GPR image location x_i

t_0 = Actual two-way travel time at the GPR image location x_0

x_0 = Location of GPR at the peak hyperbolic reflection from the buried object

x_i = Horizontal location of a selected point i in the GPR image

v_i = EM wave velocity when the EM wave propagates from the position x_i to the buried object

v_0 = EM wave velocity when the EM wave propagates from the position x_0 to the buried object

According to Al-Nuaimy [21], for rebar diameter, not over 32 mm, (1.26 in.) the rebar diameter does not significantly affect the concrete cover thickness measuring. Therefore, this research assumes $r \approx 0$, and Eq. (3) can be rewritten as Eq. (3-4).

$$\left(\frac{v_i * t_i}{2}\right)^2 = \left(\frac{v_0 * t_0}{2}\right)^2 + (x_i - x_0)^2 \tag{3-4}$$

Define $v_0 = v_i$, Eq. (3-4) can be written as a function of t_0 , t_i , x_i , x_0 , as shown in Eq. (3-5).

$$v_i = \sqrt{\frac{4(x_i - x_0)^2}{(t_i)^2 - (t_0)^2}} \tag{3-5}$$

Therefore, each pair of (x_i, t_i) will generate a singular EM wave velocity v_i. To ensure the accuracy of the analysis, erroneous data points are eliminated by applying a standard deviation (SD) limit. This limit regulates the number of discrete velocities selected for the final velocity analysis. In order to decide the final EM wave velocity at each GPR hyperbolic peak location, the average of the v_i at each hyperbolic signature is calculated. This average v value represents the

EM wave velocity at the GPR hyperbolic peak location. Subsequently, this EM wave velocity is utilized in the calculation of the concrete cover thickness during the subsequent GPR data processing stage.

Validation and Calibration

To validate the proposed methodology, a total of ten concrete specimens were cast in the laboratory. Each specimen had dimensions of 914.4 x 381 x 203.2 mm (36 x 15 x 8 in.), as shown in Figure 3- 4. The chosen dimensions, along with a spacing of 76 mm (3 in.) between rebars, ensured that the GPR waveforms captured both the direct and reflected waves for each rebar. In order to investigate the impact of the buried object's radius on velocity estimation, rebars ranging from size #3 to #11 were utilized in the specimens. Additionally, four different rebar embedded depths were considered: 25, 38, 64, and 89 mm (1, 1.5, 2.5, and 3.5 in.), which are commonly specified values according to ACI 318-19 guidelines. Detailed information on each cast concrete specimen can be found in *Table 3- 1* .

Figure 3- 4. Concrete specimens with rebar embedded

Table 3- 1.The rebar information for the concrete specimen

Sample No.	Rebar Embed Depth mm(in)	Rebar Size
1	25.4 (1)	# 3, # 4, # 5, # 6, # 7
2		# 8, # 9, # 10, # 11
3	38.1 (1.5)	# 3, # 4, # 5, # 6, # 7
4		# 8, # 9, # 10, # 11
5	63.5 (2.5)	# 3, # 4, # 5, # 6, # 7
6		# 8, # 9, # 10, # 11
7	88.9 (3.5)	# 3, # 4, # 5, # 6, # 7
8		# 8, # 9, # 10, # 11
9	101.6 (4.0)	# 3, # 4, # 5, # 6, # 7
10		# 8, # 9, # 10, # 11

3.3 Experimental Result and Discussion

GPR data were collected from the ten concrete specimens. After hyperbola fitting, each hyperbola will generate a peak coordinate (x_0, t_0), the reference velocity v_0 of each rebar is calculated using known depth divided by the travel time. The coordinates (x_i, t_i) along each hyperbola were collected to calculate the EM velocity using the proposed method. The results from the velocity estimation analysis for different rebar depths are presented in Tables 2 to 6. Each table provides the data for different rebar depths, along with the corresponding sample, rebar size, x_0 (mm), t_0 (ns), v_0 (mm/ns), v (mm/ns), and the percentage error.

Table 3- 2 shows the results for the rebar depth of 25.4 mm (1 in.). It can be observed that the absolute error of the calculated velocity compared to the reference velocity is generally low, with most rebar sizes (#3 to #9) demonstrating an absolute error rate of less than 5%. The highest absolute error is observed for the #11 rebar, with a 6.78% error rate. These results suggest that the proposed algorithm performs well in estimating the velocities for these rebar sizes. For example, in table 1. sample 1, the absolute error for rebar size #3 is 3.31%. This indicates that the estimated velocity of 96.539 mm/ns is very close to the reference velocity of 93.446 mm/ns. Similarly, for rebar sizes #4 to #7, the absolute error rates range from -2.76% to 4.25%, indicating reasonably

accurate velocity estimations. However, for larger rebar sizes such as #10 and #11, the absolute error rates are slightly higher, reaching 5.75% and 6.78% respectively.

Table 3- 2. Rebar depth 25.4 mm (1 in.)

Sample	Rebar	x_0 (mm)	t_0 (ns)	v_0 (mm/ns)	v (mm/ns)	% Error
1	#3	7.629	0.544	93.446	96.539	3.31%
	#4	83.067	0.542	93.779	91.191	-2.76%
	#5	158.251	0.514	98.898	94.349	-4.60%
	#6	232.165	0.511	99.374	101.749	2.39%
	#7	305.317	0.535	95.012	99.050	4.25%
2	#8	8.732	0.534	95.201	99.685	4.71%
	#9	83.650	0.551	92.163	96.697	4.92%
	#10	157.038	0.514	98.894	104.581	5.75%
	#11	232.240	0.511	99.335	106.070	6.78%

Table 3- 3 presents the results for the rebar depth of 38.1 mm (1.5 in.). Similar to Table 2, the absolute error is generally low, with most rebar sizes (#3 to #9) showing an absolute error rate of less than 5%. The highest error rate is observed for the #11 rebar, with a 6.28% error.

Table 3- 3. Rebar depth 38.1 mm (1.5 in.)

Sample	Rebar	x_0 (mm)	t_0 (ns)	v_0 (mm/ns)	v (mm/ns)	% Error
3	#3	4.380	0.844	90.323	88.236	-2.31%
	#4	82.925	0.812	93.876	90.318	-3.79%
	#5	152.293	0.864	88.228	91.890	4.15%
	#6	228.975	0.811	93.934	97.118	3.39%
	#7	302.127	0.835	91.292	95.455	4.56%
4	#8	11.663	0.821	92.858	97.603	5.11%
	#9	86.581	0.838	90.909	96.291	5.92%
	#10	159.969	0.801	95.169	100.622	5.73%
	#11	235.171	0.798	95.441	101.435	6.28%

In Table 3- 4, the results for the rebar depth of 63.5 mm (2.5 in.) are displayed. The absolute error remains relatively low, with most rebar sizes (#3 to #9) demonstrating an absolute error rate of less than 5%. The highest error rate is observed for the #11 rebar, with a 6.34% error.

Table 3- 4. Rebar depth 63.5 mm (2.5 in.)

Sample	Rebar	x_0 (mm)	t_0 (ns)	v_0 (mm/ns)	v (mm/ns)	% Error
5	#3	10.323	1.367	92.929	94.946	2.17%
	#4	88.867	1.384	91.796	94.357	2.79%
	#5	158.241	1.398	90.865	88.929	-2.13%
	#6	234.924	1.334	95.180	98.264	3.24%
	#7	308.076	1.358	93.543	97.435	4.16%
6	#8	8.299	1.356	93.647	98.077	4.73%
	#9	83.216	1.385	91.703	97.086	5.87%
	#10	156.604	1.337	94.997	100.982	6.30%
	#11	231.806	1.352	93.928	99.883	6.34%

Moving on to Table 3- 5, which represents the rebar depth of 88.9 mm (3.5 in.), it can be observed that the absolute error remains within an acceptable range. Most rebar sizes (#3 to #9) exhibit an absolute error rate of less than 5%. The highest error rate is observed for the #11 rebar, with a 6.70% error.

Table 3- 5. Rebar depth 88.9 mm (3.5 in.)

Sample	Rebar	x_0 (mm)	t_0 (ns)	v_0 (mm/ns)	v (mm/ns)	% Error
7	#3	9.819	1.836	96.855	99.887	3.13%
	#4	88.363	1.854	95.911	92.852	-3.19%
	#5	157.736	1.796	99.011	102.704	3.73%
	#6	234.419	1.803	98.597	102.748	4.21%
	#7	307.571	1.827	97.330	101.574	4.36%
8	#8	11.384	1.826	97.387	102.412	5.16%
	#9	86.302	1.843	96.457	102.168	5.92%
	#10	159.690	1.806	98.462	104.832	6.47%
	#11	234.892	1.804	98.586	105.191	6.70%

Lastly, Table 3- 6 presents the results for the rebar depth of 101.6 mm (4.0 in.). The absolute error remains relatively low, with most rebar sizes (#3 to #9) showing an absolute error rate of less than 5%. The highest error rate is observed for the #11 rebar, with a 7.01% error.

Table 3- 6. Rebar depth 101.6 mm (4.0 in.)

Sample	Rebar	x_0 (mm)	t_0 (ns)	v_0 (mm/ns)	v (mm/ns)	% Error
9	#3	10.589	2.048	99.212	103.310	4.13%
	#4	89.133	2.066	98.345	102.200	3.92%
	#5	158.506	2.008	101.187	105.214	3.98%
	#6	235.190	2.016	100.809	105.446	4.60%
	#7	308.341	2.039	99.648	104.402	4.77%
10	#8	8.399	2.038	99.700	105.792	6.11%
	#9	83.316	2.056	98.847	104.758	5.98%
	#10	156.705	2.018	100.685	107.451	6.72%
	#11	231.906	2.016	100.799	107.865	7.01%

Overall, the results demonstrate that the proposed method provides reasonably accurate velocity estimation for different rebar depths. The absolute error rates are generally within an acceptable range, with most rebar sizes showing errors of less than 5%. The higher error rates observed for the #11 rebar could be attributed to the increased complexity introduced by larger rebar sizes. Nevertheless, the proposed methodology proves to be effective in estimating GPR wave velocity for a range of rebar depths, providing valuable insights for non-destructive evaluation and subsurface characterization.

The velocity analysis for different rebar sizes (#3 to #11) at varying depths (25.1 mm to 101.6 mm) was conducted, and the results are presented in Figure 3- 5 (a) to (i), based on the values extracted from Table 3- 2 to Table 3- 6. Figure 3- 5 (a) represents the velocity analysis for the #3 rebar. The horizontal axis denotes the rebar depth, ranging from 25.1 mm to 101.6 mm, while the vertical axis represents the velocity. Both the reference and the calculated velocity for the #3 rebar at depths from Table 3- 2 to Table 3- 6 are plotted on the graph. The data points illustrate the variations in velocity for different rebar depths, providing insights into the behavior of the #3 rebar at varying depths. Similarly, Figure 3- 5 (b) to (i) depict the velocity analysis for the #4 to #11 rebars, respectively. Each graph follows the same format, with the rebar depth on the

horizontal axis and the velocity on the vertical axis. The reference and the calculated velocity extracted from Table 3- 2 to Table 3- 6 are plotted on the respective graphs for each rebar size.

The analysis of the graphs reveals trends in velocity variation for different rebar sizes and depths. The closeness of these two values indicates the reliability of the estimation method, while larger discrepancies may suggest potential sources of error or limitations in the estimation process. Upon observing Figure 3- 5 (a) to 5(c), corresponding to rebar #3 to #5, it can be noted that there is an up-and-down variance in velocity at different depths compared to the reference velocity. However, these differences fall within a range of 5 mm/ns, indicating a good level of accuracy in the velocity estimation.

Similarly, Figure 3- 5 (d) to 5(i), corresponding to rebar #6 to #11, show that the calculated velocities are slightly above the reference velocities, but still within 5 mm/ns. This indicates that the velocity estimation remains accurate.

Overall, the velocity analysis graphs provide a visual representation of the relationship between rebar depth and velocity for different rebar sizes. These insights contribute to the understanding of the behavior of GPR wave velocities in concrete structures with varying rebar depths, and they validate the effectiveness of the proposed methodology in estimating GPR wave velocities accurately.

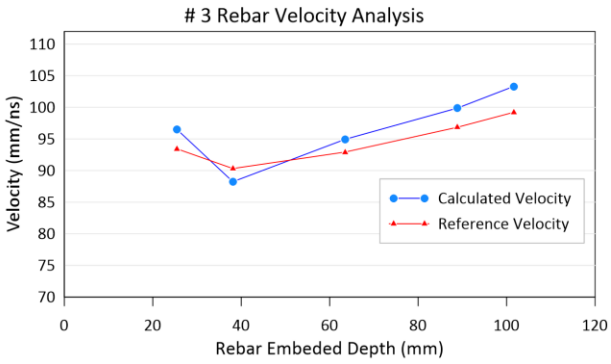

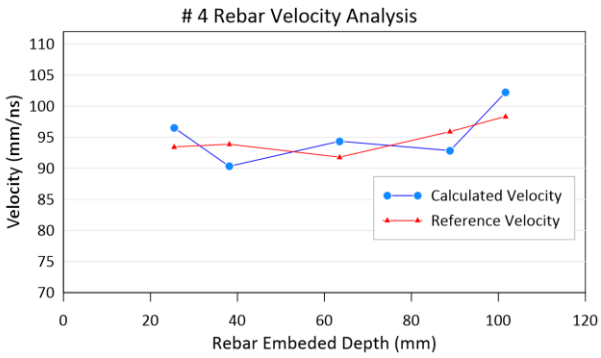

(a)

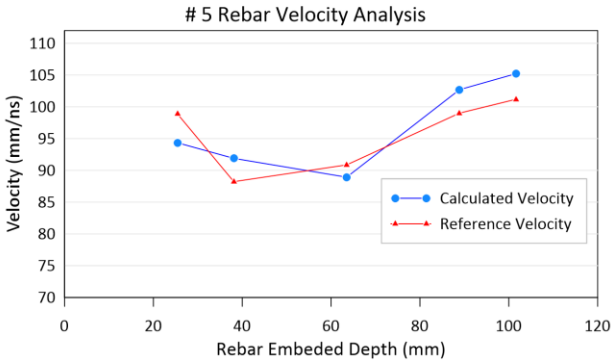
5 Rebar Velocity Analysis
Velocity (mm/ns)
Rebar Embeded Depth (mm)
Calculated Velocity
Reference Velocity

(b)

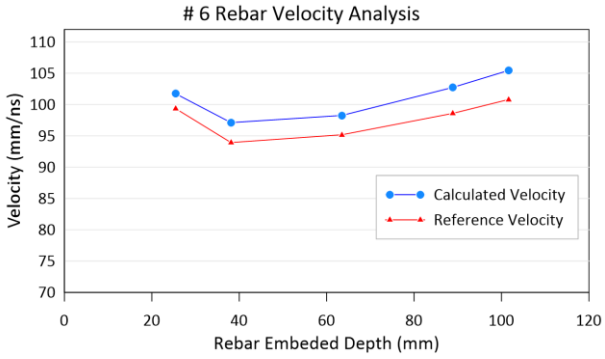
6 Rebar Velocity Analysis
Velocity (mm/ns)
Rebar Embeded Depth (mm)
Calculated Velocity
Reference Velocity

(c)

(d)

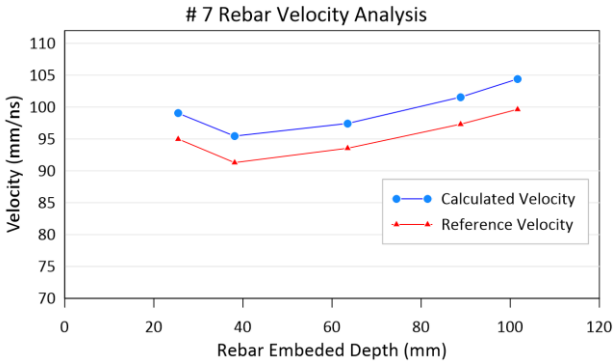
7 Rebar Velocity Analysis
Velocity (mm/ns)
Rebar Embeded Depth (mm)
Calculated Velocity
Reference Velocity

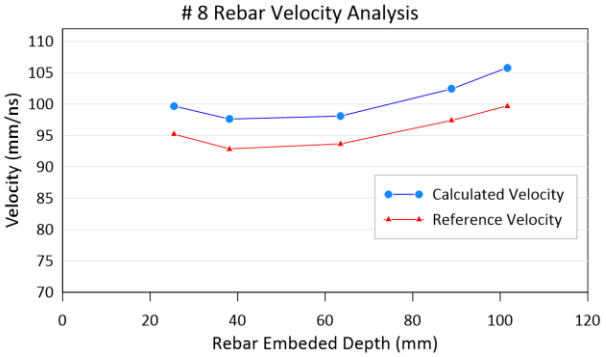
8 Rebar Velocity Analysis
Velocity (mm/ns)
Rebar Embeded Depth (mm)
Calculated Velocity
Reference Velocity

(e)

(f)

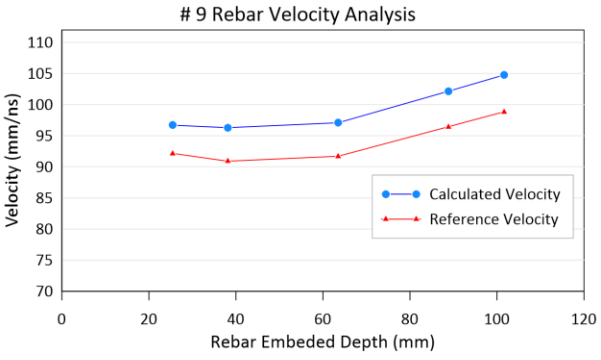
9 Rebar Velocity Analysis
Velocity (mm/ns)
Rebar Embeded Depth (mm)
Calculated Velocity
Reference Velocity

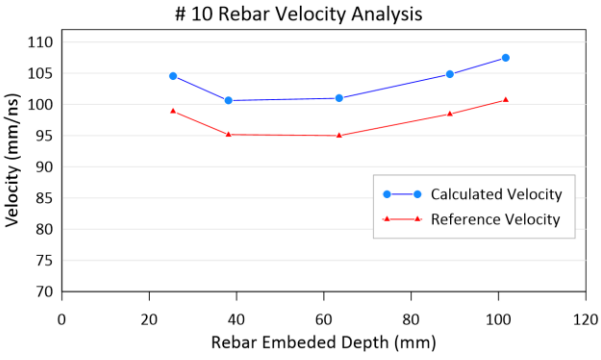
10 Rebar Velocity Analysis
Velocity (mm/ns)
Rebar Embeded Depth (mm)
Calculated Velocity
Reference Velocity

(g)

(h)

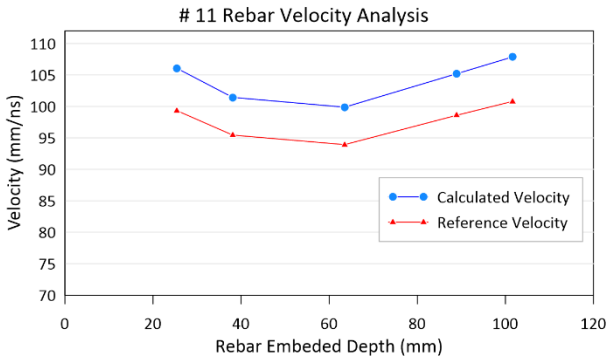

(i)

Figure 3- 5. Rebar Velocity Analysis with rebar size of: (a) #3; (b) #4; (c)#5; (d) #6; (e)#7; (f) #8; (g) #9; (h)#10; (i) #11

3.4 Conclusion

This paper has presented a novel nondestructive algorithm for accurately estimating GPR's electromagnetic wave velocity. The proposed algorithm, based on hyperbolic fitting and travel-time analysis, offers a practical solution for GPR practitioners to enhance subsurface imaging capabilities and improve data interpretation. One of the significant advantages of this research lies in its ability to provide accurate velocity estimation without the need for core drilling. Core drilling is a traditional method used to obtain concrete samples for velocity estimation, but it can be time-consuming, expensive, and destructive to the structure being investigated. The proposed nondestructive algorithm eliminates the need for core drilling, making the velocity estimation process much more efficient and cost-effective. Through laboratory experiments, the algorithm's performance was thoroughly assessed and validated. The results consistently demonstrated the algorithm's accuracy and reliability in estimating the wave velocity. The algorithm maintained its effectiveness across various GPR system configurations, highlighting its robustness and adaptability. By providing an accurate estimation of GPR's electromagnetic wave velocity, the proposed algorithm enables enhanced subsurface investigations, such as concrete rebar location

and subsurface characterization. This contributes to more precise data interpretation, informed depth measuring, and improved overall efficiency in civil engineering and geophysical applications.

Future research can focus on further refining the algorithm's performance and exploring its applicability in different scenarios. Additionally, the integration of this algorithm with other GPR data processing techniques may lead to more comprehensive and advanced subsurface imaging methodologies. In conclusion, the proposed nondestructive algorithm represents a significant advancement in GPR technology, offering a reliable and efficient approach for estimating electromagnetic wave velocity. Its implementation has the potential to significantly enhance subsurface imaging capabilities and improve data interpretation in various practical applications.

Acknowledgments

The authors acknowledge the editorial assistant and the thorough revision by the anonymous reviewers who significantly improved the proposed research work.

CHAPTER 4

Comprehensive GPR Data Processing Algorithm in Reinforced Concrete Structures

ABSTRACT

Nondestructive Evaluation (NDE) of reinforced concrete (RC) structures in civil engineering often relies on Ground Penetrating Radar (GPR) as a versatile tool to determine concrete cover thickness and locate reinforcement. However, the complexities associated with processing raw GPR data, including time zero correction, electromagnetic (EM) wave velocity calculation, background noise removal, and hyperbola signature identification, require the specialized knowledge of GPR practitioners and manual rebar picking. Achieving fully automated GPR data processing remains a challenge. To address this issue, this paper proposes a comprehensive method based on image processing, and curve-fitting principles to process the raw GPR data to identify and localize the rebar. The proposed method has been validated on forty lab-made reinforced concrete blocks, three bridge decks, and one culvert data. Results of conducting the experiments are promising and reveal that: (1) the processing application developed in this study has achieved full automation, eliminating the need for manual interpretation or manual rebar-picking; (2) the proposed data processing algorithm can correct the time-zero, and calculate the EM wave velocity without core-drilling; (3) the proposed data processing system has improved the data processing efficiency significantly.

Keywords: Ground-penetrating radar (GPR), Hyperbola, Rebar location, Image processing, Curve fitting, Automated rebar recognition

4.1 Introduction

Condition assessment is one of the most crucial maintenance procedures for reinforced concrete (RC) structures. During an inspection, it is frequently necessary to know the as-built locations and cover thickness of the reinforcing steel bars [1-3]. Ground Penetrating Radar (GPR) is one of the most popular Non-Destructive Evaluation (NDE) methods to carry out work such tasks due to its high penetrating capabilities, quick scanning speed, and capacity to detect hidden objects [4-6]. It comprised a radar control unit (radargram), a data acquisition system, a transmitting antenna, and a receiving antenna. High-frequency pulsed Electromagnetic (EM) waves (between 10 and 3000 MHz) or radar waves are used to collect subsurface data. In the subsoil, the transmitting antenna sends off an EM pulse. Any buried objects or modifications in the subsurface material cause the EM pulse to reflect back to the surface. The receiving antenna picks up the return signals and logs the related fluctuations. The radargram interprets and shows the detected subsurface image. The depth and position of the interruption (buried object) are revealed by measuring the time it takes for the reflected signals to return [7-10].

GPR A-scan is a graphical representation of the reflected signal from the subsurface when a single pulse of electromagnetic energy is transmitted to the ground, as depicted in Figure 4- 1. It provides information about the depth and amplitude of reflections, allowing for the identification of subsurface targets such as buried utilities, geological layers, or archaeological artifacts. On the other hand, GPR B-scan is a two-dimensional representation of the subsurface obtained by continuously scanning the ground surface with a GPR antenna while collecting A-scan data along a specific line. It provides a cross-sectional view of the subsurface, displaying variations in reflection patterns and depths. GPR B-scans are valuable for mapping and interpreting subsurface features over larger areas, aiding in geological, engineering, and environmental investigations.

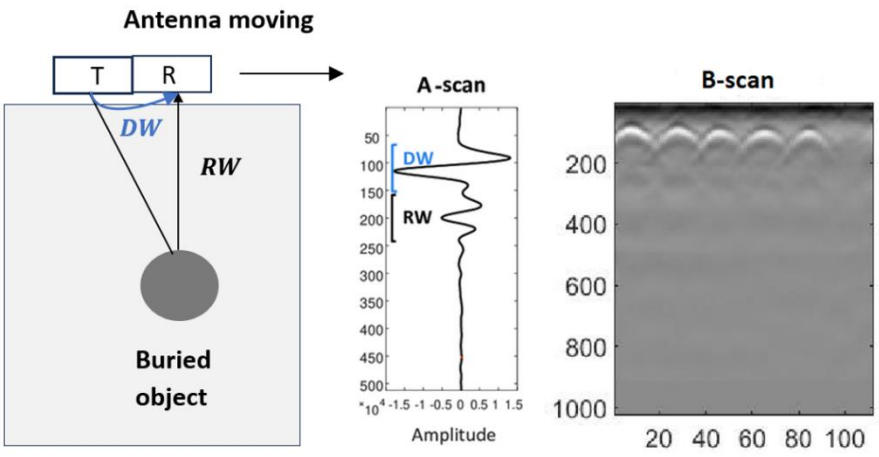

Figure 4- 1. GPR A-scan and B-scan data

Steel reinforcement in RC can often be found and located using GPR. Although GPR data collecting is quick and effective, its data interpretation is labor-intensive and depends on the operator's expertise to deliver accurate output. Currently, commercial software such as Radan from GSSI and GPRslice have limitations in effectively and accurately processing GPR data. [11] underscores that GPRslice is inadequate for handling large datasets or multiple frequencies, limited by the available computer memory. The program's functionality is based on the assumption of data collection along a straight line and a relatively uniform subsurface. It also encounters challenges in automated data analysis. Additionally, RADAN's capabilities are constrained to data with minimal noise, resulting in recognition accuracy for datasets as low as 54% [12]. Therefore, academic scholars have looked into a potential method for automatically identifying rebar from the GPR data [13]. These studies can be divided into two groups: (a) Image-based approach (pattern recognition); and (b) Machine learning-based approach.

The output of a GPR is often interpreted as images due to its characteristic hyperbolic signature [14]. Image processing techniques have been extensively used to generate visual representations of GPR data and extract relevant features from these images. For instance, visual

patterns of buried objects recorded in GPR data reflect depth and size and this has been used to determine rebar depth from the extracted parameters of these patterns [15, 16]. However, the inherent difficulties in analyzing GPR data limit this method's efficacy. Several studies have focused on identifying rebar signals through the distinct reflection of hyperbolic traces, such as the automated rebar recognition technique developed by Sato et al. [11]. The research utilized a wavelet recognition technique that filtered the concentrated energy of hyperbolic traces and transformed the GPR data using a parabolic wavelet. Compared to the inverse scattering problem [12], the image-based solution benefits from its computational efficiency by employing pattern analysis within specific areas of the bridge deck. The pattern-based methods have limited applicability in other contexts and are primarily used in geological surveys [17, 18]. Researchers have also explored various image processing techniques, including edge detection, thresholding, and texture analysis [19-25]. Using edge detection and thresholding to identify potential hyperbola regions on local extrema of intensity for image pre-processing has been an intuitive strategy frequently employed in prior studies. However, these techniques have inherent limitations, such as subpar performance in the presence of noise and image blurring. Moreover, thresholding often requires manual selection and adjusting parameters specific to the analyzed dataset.

Some studies have employed neural networks as a machine learning approach for automated rebar detection in GPR data [4, 23, 24, 26, 27]. It is important to note that these methods utilize edge detection as a pre-processing step, posing similar limitations in terms of sensitivity to noise and the need for parameter adjustment as conventional edge detectors. Singh and Nene [27] focused on a single GPR image featuring four hyperbolas, and the investigation yielded promising outcomes in the classification stage through neural networks. Another technique [26] involved trapezoidal image cropping before neural network classification, enabling the identification of

hyperbolic regions. However, this method lacks curve fitting and roughly localizes the hyperbola apex by evaluating pixels within the fixed trapezoidal region. Support Vector Machines (SVM) have also been utilized for automated rebar classification [28-30]. Although it utilized synthetic data, earlier studies on SVM-based rebar detection demonstrated favorable results [17]. However, this approach involves thresholding the image for binarization, resulting in a fragile image representation that heavily relies on parameter selection.

While automated GPR data processing techniques have shown promise, there is still a need for further research to address shortcomings, including (1) Lack of a comprehensive algorithm to automate the GPR data processing from collected raw data to generate rebar information; (2) The accuracy of the data processing still needs to be improved, due to the effects of unknown time-zero offset, interference from background noise, unknown EM wave velocity, challenges of recognizing the hyperboles, and interpreting the location of the rebar; and (3) Inefficient GPR data processing since traditional method involves manual rebar picking which is labor demanding. To address these limitations, the primary objective of this research is to develop a robust automated algorithm. This advanced algorithm will be designed and implemented to conduct a seamless and automated GPR data processing workflow. This comprehensive workflow will encompass crucial stages such as raw data import, noise reduction, time-zero correction, EM wave velocity estimation, hyperbola identification, and precise rebar localization. The goal is to eliminate the need for manual intervention and significantly enhance the efficiency of the entire GPR data processing process.

4. 2 Methodology

The general processing steps are illustrated in Figure 4- 2, and the specifics of each step are described in the subsequent subsections. All the processing scripts in this research are implemented using MATLAB [96].

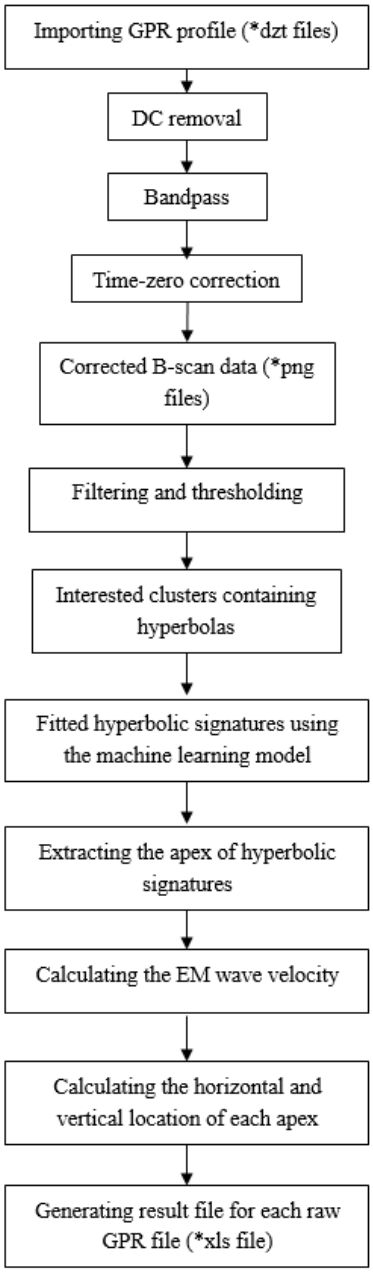

Figure 4- 2. Flowchart of the proposed GPR data processing algorithm

Importing GPR profile

SIR-10H type GSSI radar exploration system outputs the scan data in a binary DZT file containing two-part, the header followed by scan data as shown in Figure 4- 3. It is necessary to have a detailed interpretation of the header concerning the settings used to collect the data and the header size per the guidance provided in the literature [32]. Using MATLAB software's 'uigetfile' function, the original file input can be obtained via a Graphical User Interface (GUI). The user is then prompted with a dialog box, enabling the selection of the appropriate raw data file. Subsequently, the 'fopen' function is employed to open the chosen file, while the 'fseek' and 'fread' functions are utilized to read the header files and data volume sequentially. This approach enables systematically retrieving the file's header parameters and data based on the specific header structures and interpretations. Finally, leveraging the graphical tools of MATLAB, the collected GPR data can be visualized (Figure 4- 4).

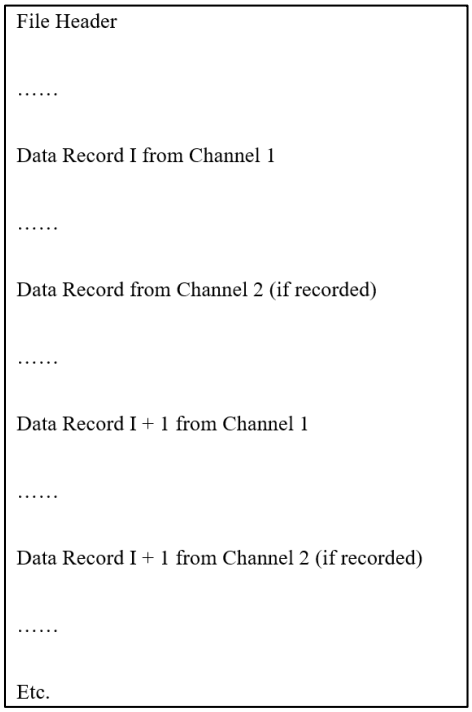

Figure 4- 3. DZT file format

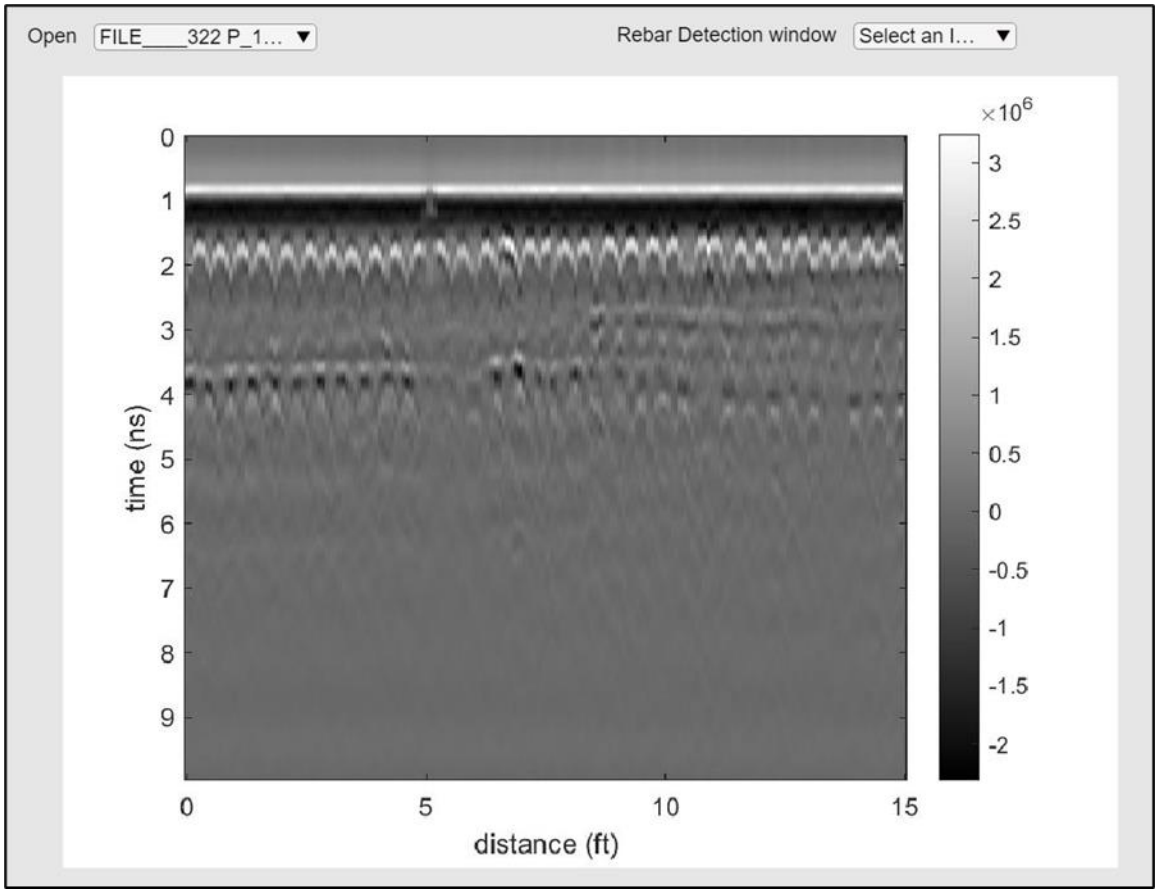

Figure 4- 4. Visualization of the collected raw data

DC removal and bandpass

After importing the DZT file into MATLAB, Direct current (DC) removal and bandpass filtering are applied before time-zero correction. DC removal eliminates the low-frequency baseline or average signal level, effectively removing slow-varying components and environmental noise from the data. This step enhances the visibility of actual radar reflections and prepares the data for further analysis. Subsequently, bandpass filtering is employed to selectively allow a specific frequency range of the GPR signal to pass through while attenuating frequencies outside the designated range. It is carefully optimized to focus on the depth range of interest and to suppress unwanted noise or interference. The GPR data is effectively conditioned by applying

these pre-processing steps in the specified order, improving data quality and facilitating subsequent automatic data processing algorithms.

Time-zero correction

After pre-processing the GPR data, the next step involves applying the time-zero to determine the two-way travel time and precisely measure depth. Depending on the type of antennae used, the time-zero corresponds to different reflections. It aligns with the reflection from the ground surface for an air-coupled antenna, while it corresponds to the direct-coupling reflection for a ground-coupled antenna. Conventionally, the time-zero is positioned at either the maximum negative or positive peaks of the first wavelet, but these peaks do not represent the true time-zero position. Based on previous research [33], the authors propose a more accurate time-zero position at 0.14 ns ahead of the first negative peak of each GPR A-scan. This choice is informed by the understanding that the first wavelet in an A-scan corresponds to the ground surface, which is mixed with the direct wave between the transmitter and receiver, resulting in a direct-coupling reflection. These reflections can be notably strong, especially for concrete bridge decks, comparable to those from the top reinforcing layer. Detailed information regarding the proposed time-zero correction can be found in the literature [33]. Figure 4- 5 displays the GPR image before and after applying the proposed time-zero correction. The time-zero corrected GPR data is effectively aligned and then saved in PNG format using the 'imwrite' function. This image format maintains the visual quality of the GPR results and allows consistent visualization across various platforms and software applications, facilitating seamless analysis and collaboration among researchers and practitioners.

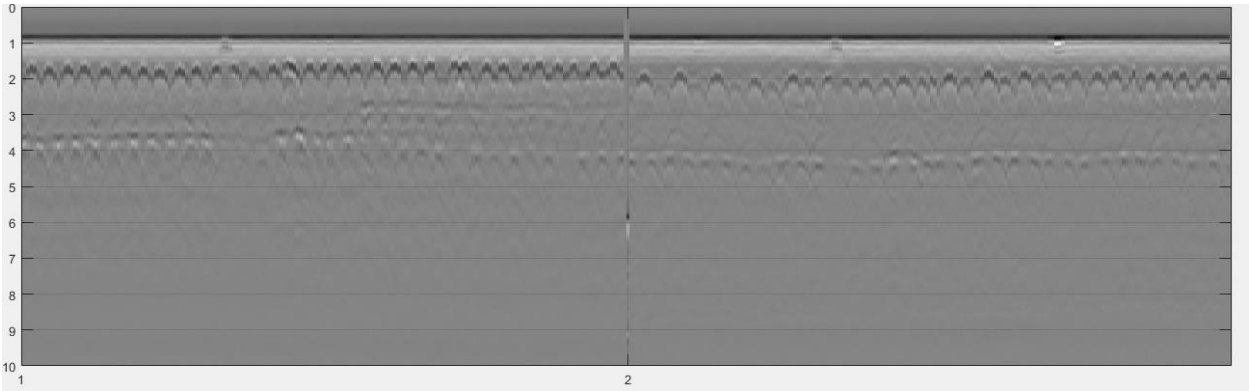

(a)

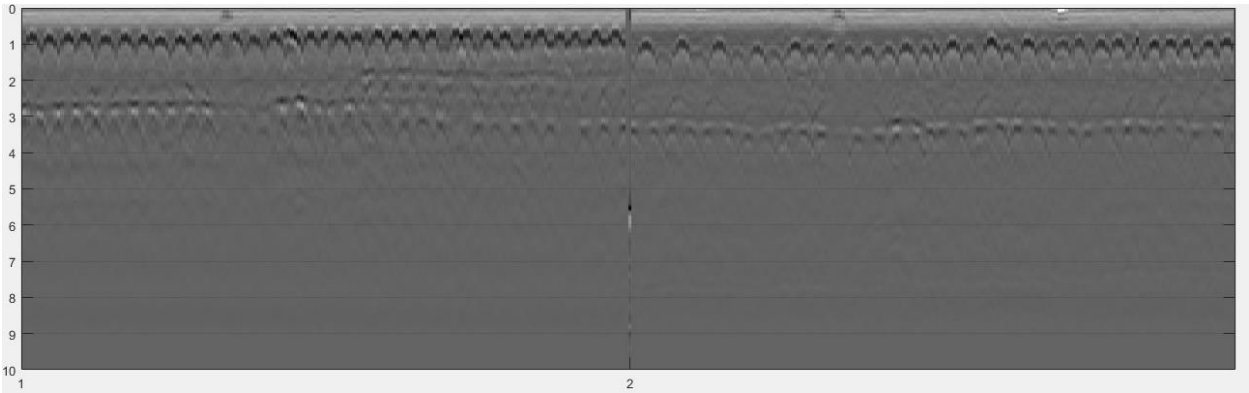

(b)

Figure 4- 5. GPR images: (a) before time-zero correction; (b) after time-zero correction

Filtering and thresholding

After time-zero correction, moving average filtering and thresholding are implemented to facilitate further data analysis. Firstly, the moving average filtering is employed to smooth the GPR data, reducing noise and random variations in the signal. It involves taking the average of neighboring data points within a specified window. Three by three were used in this research, effectively preserving significant features while minimizing undesirable fluctuations. Subsequently, thresholding is applied to classify the GPR data into subsurface categories based on their amplitudes. By setting a threshold value, reflections above the limit are considered potential

targets, while those below it are regarded as noise or background. Figure 4- 6 displays the input image after applying the moving average filter and thresholding.

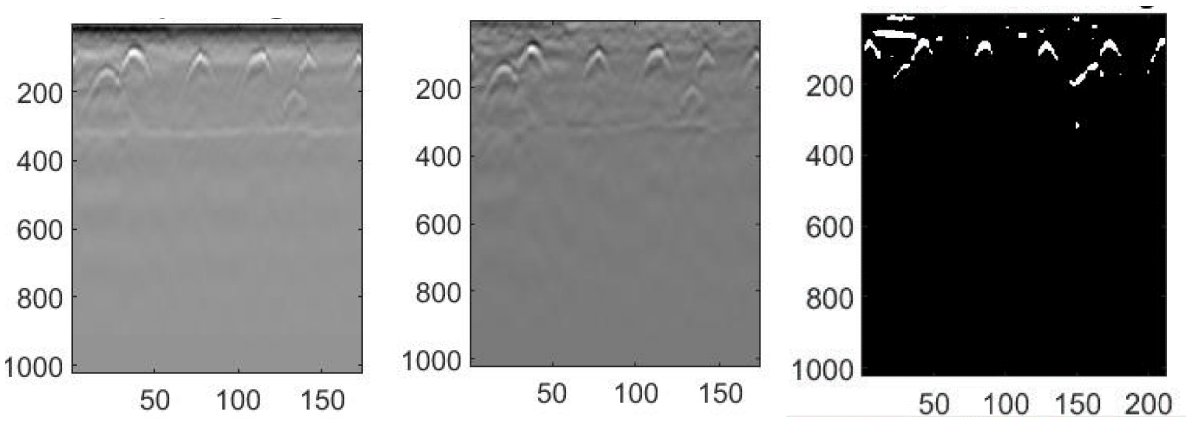

Figure 4- 6. Illustration of filtering and thresholding techniques: (a) Input image; (b) Image after filtering; (c) Image after thresholding

Extracting interested clusters containing hyperbolae

After applying thresholding, the binary image is generated. The column-connection clustering (C3) algorithm [29] is then applied to identify regions of interest containing potential hyperbolas. The C3 algorithm simplifies the B-scan GPR image by representing objects with single central strings, enhancing the B-scan representation and reducing computation time. It operates in three phases: column segmentation, column-segment connection (clustering), and central string extraction. Scanning the binary image column-wise from left to right, groups distinct regions into connected clusters. A cluster is formed when a series of consecutive points exceeds three and if a connecting element is found in the neighboring column at the same row. For each column segment in the first column, the C3 algorithm checks for connecting elements in the second column, ensuring cluster continuity. The process may lead to cluster splitting into multiple clusters. Each output cluster yields a central string composed of middle points from each column within the

cluster. The longest central string's points are then utilized for subsequent hyperbola fitting. The pseudo-code of the C3 Algorithm can be found in reference [34].

Hyperbola fitting using a machine learning model

To effectively identify hyperbolic signatures within the outputs of the C3 algorithm, extracting distinctive attributes that characterize these signatures is essential. This enables distinguishing the target hyperbola from other undesired and composite clusters formed by multiple hyperbolae. In a B-scan image, the identified hyperbolic (Figure 4- 7) features are visually represented as "south-opening" branches given by Eq. (4-1):

$$\left(\frac{y-y_0}{a^2}\right)^2 - \left(\frac{x-x_0}{b^2}\right)^2 = 1, \text{ with } y < 0 \quad (4\text{-}1)$$

Where:

y = Two-way travel time of the EM waves

x = Distance along the measured direction

(x_0, y_0) = Center of the hyperbola

a = Length of the semi-major axis

b = Length of semi-minor axis

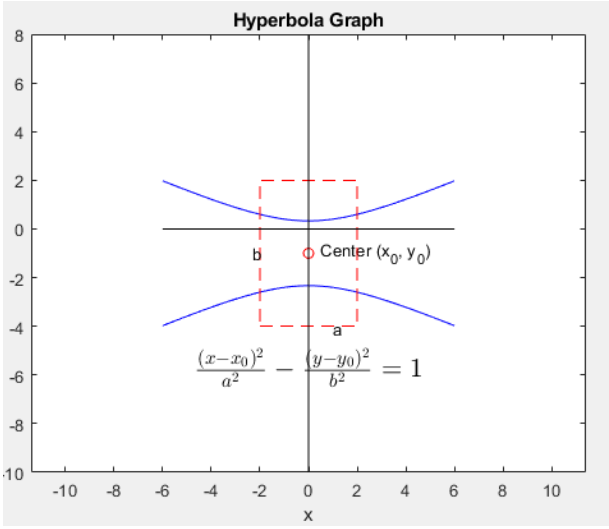

Figure 4- 7. Graph of a sample hyperbola

The flowchart in Figure 4- 8 outlines the step-by-step process of the machine learning model for GPR hyperbola detection. It starts with training the samples from the output of the C3 algorithm, which are then separated into negative and positive groups. Random Sample Consensus (RANSAC) [35] is then employed to fit hyperbolas to the detected peaks, handling noise and outliers effectively. Non-linear least-squares fitting [36] is then applied to refine hyperbola parameters, enhancing model accuracy. The machine learning model is trained using those labeled data to predict hyperbola parameters based on input features. Evaluation metrics assess the model's performance, and hyperparameter tuning is conducted if the model's performance is not satisfactory. Once trained, yielding high accuracy as indicated by the evaluation results, the model can be used for hyperbola detection in new GPR data.

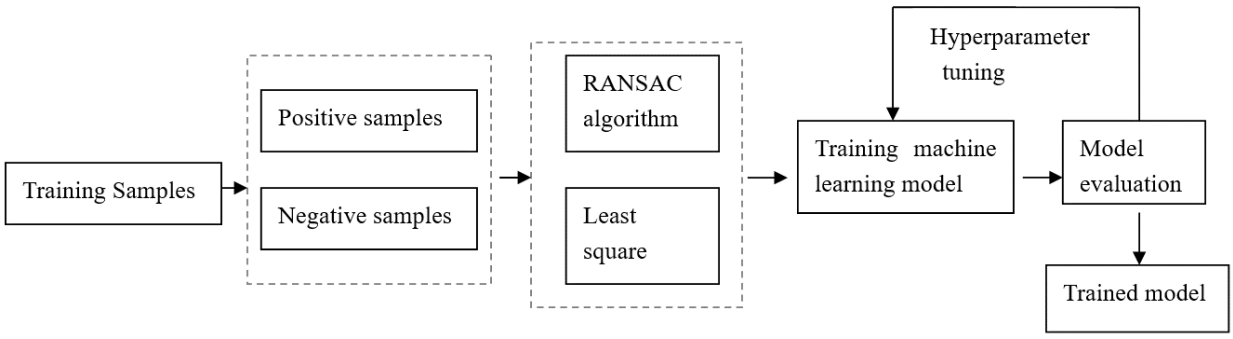

Figure 4- 8. Flowchart of the hyperbola fitting model

Extracting the apex of the hyperbola

After applying the trained automated hyperbola detection model, the input GPR images undergo hyperbola detection to identify hyperbolic curves within the radargram. The hyperbola reflections are illustrated in Figure 4- 9 (a), while in Figure 4- 9 (b), the hyperbola curves are displayed along with their fitted curves. The apex of each hyperbola, corresponding to the coordinates (x_0, y_0), is then extracted and saved for subsequent analysis.

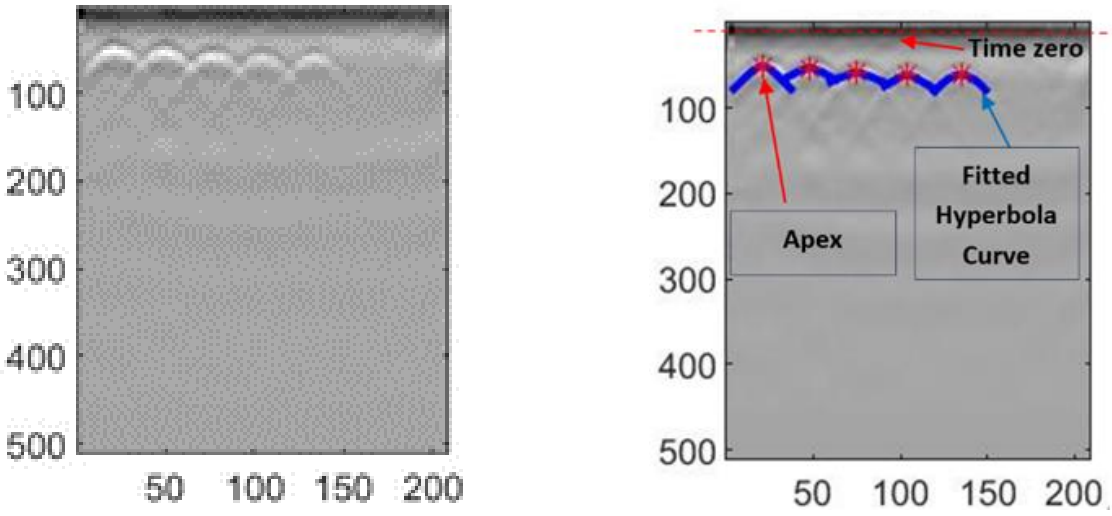

(a) (b)

Figure 4- 9. GPR images (a) The input raw image; (b) Target rebar detected and located GPR image

Calculating the EM wave velocity and locating the apex

By adjusting the time-zero position, the actual two-way travel time of the EM wave in the concrete is obtained and consequently used to calculate the concrete cover thickness of rebars. The relationship between concrete cover thickness, EM wave velocity in the concrete, and the EM wave two-way travel time is given by Eq. (4-2). The EM wave velocity in the concrete is affected by the dielectric constant of concrete and the relationship between the two is given by Eq. (4-3).

$$D = \frac{v * t_a}{2} \tag{4-2}$$

$$v = \frac{c}{\sqrt{\epsilon}} \tag{4-3}$$

Where:

D = Concrete cover thickness

t_a = Actual two-way travel time of the EM wave in the concrete

v = EM wave velocity

c = Speed of light in air

ϵ = Dielectric constant of concrete

For each detected hyperbola which represents a rebar, t_a equals y_0 since the vertical axis represents the EM wave travel time in the GPR data. Traditionally, core drilling is necessary for GPR application to estimate the concrete cover thickness. Multiple cores are drilled to measure the clear cover thickness. The true concrete cover thickness values are then used to back-calculate the actual concrete dielectric constant, which is used in the subsequent GPR data processing. However, this method is destructive, time-consuming, and not accurate because the dielectric constant at each core drilling point may differ. In this research, the EM wave velocity is calculated based on the analysis of hyperbolic fitting and travel-time analysis. Eq. (4-4) describes the calculation of EM wave velocity for each hyperbola.

$$v_i = \sqrt{\frac{4(x_i - x_0)^2}{(t_i)^2 - (t_0)^2}} \tag{4-4}$$

Where:

v_i= EM wave velocity while the antenna is at the location x_i

(x_i, t_i) = Coordinates of each point in the detected hyperbola curve (Figure 4- 10)

(x_0, t_0) = Coordinates of the peak in the detected hyperbola curve

Each pair of (x_i, t_i) along the detect hyperbola (Figure 4- 10) will generate a singular EM wave velocity v_i. To ensure the accuracy of the analysis, erroneous data points are eliminated by applying a standard deviation (SD) limit. This limit regulates the number of discrete velocities selected for the final velocity analysis. In order to decide the final EM wave velocity at each GPR hyperbolic peak location. The average of the collected EM wave velocity v_i is then calculated,

resulting in the EM wave velocity v at the GPR hyperbolic peak location. Subsequently, this EM wave velocity is utilized in the calculation of the concrete cover thickness during the subsequent GPR data processing stage.

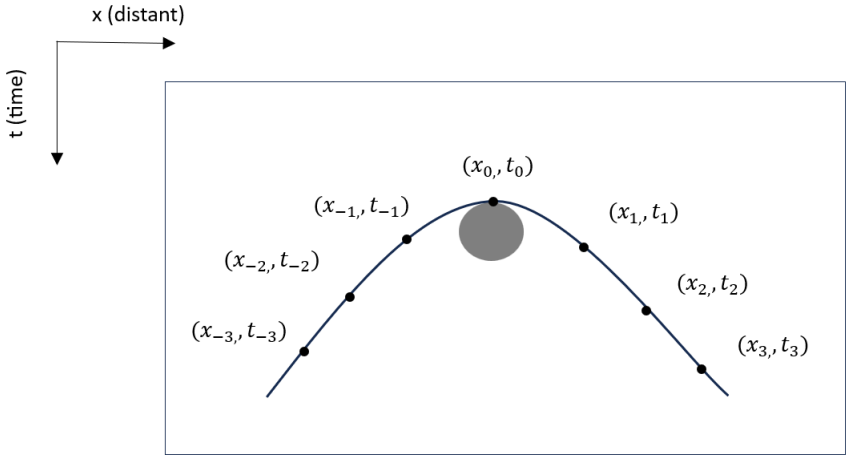

Figure 4- 10. Fitted hyperbolic curve of a buried object

Description of the software implementation

The proposed comprehensive GPR data processing algorithm can be effectively implemented as a user-friendly MATLAB application, offering ease of use and accessibility. The interface of the application with four intuitive operation steps is depicted in Figure 4- 11. The "Import File" tab empowers users to select the raw data folder and designate a location for storing processed data. In the "T0 Correction" tab, users can apply time correction alongside DC removal and bandpass filtering. The corrected data is then saved as an image file, facilitating subsequent processing. The "Automated Recognition" tab encompasses processing steps ranging from filtering to the calculation of each hyperbola apex's location. Lastly, the "Export Result" tab enables the conversion of processed data into an Excel sheet for user visualization.

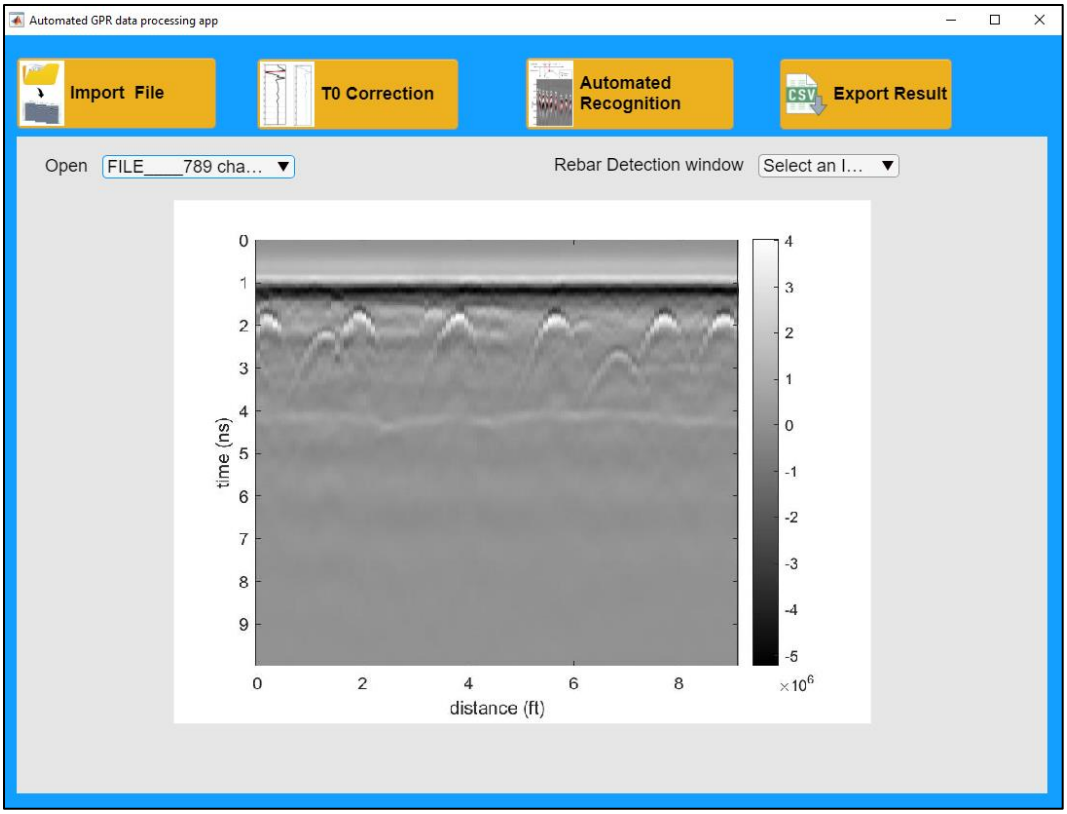

Figure 4- 11. The interface of the developed GPR data processing application

4. 3 Experimental Result

4. 3.1 Data collection setup and description of the datasets

In order to assess the efficacy of the proposed GPR data processing algorithm, data were collected from laboratory specimens and full-scale structures. Forty laboratory RC blocks, three bridge decks, and one culvert were scanned using GSSI SIR-30 GPR. Subsequently, the data was processed using commercial software and the proposed algorithm.

GPR data collection first involves setting up the control unit and the antennae. The antennae, typically cart-mounted or held by an operator, emit electromagnetic pulses into the ground while moving along the 762 mm (2.5 ft) apart parallel straight paths. Parameters such as pulse frequency, antenna orientation, and data sampling rate are typically adjusted based on the anticipated subsurface conditions and the desired resolution.

Lab Specimens

Forty samples were meticulously prepared, each exhibiting distinct variations in rebar depths, sizes, and spacing. Detailed information about the samples can be found in Table 4- 1. The visual representation of the reinforced concrete (RC) samples utilized in the study is depicted in Figure 4- 12. To conduct surface scanning, a handheld antenna operating at a frequency of 2.6 GHz was utilized. The scanning process involved the movement of antenna survey wheels along two parallel lines, ensuring comprehensive coverage of the sample surfaces.

Table 4- 1.The RC sample rebar information

Specimen number	Rebar depth mm (in.)	Rebar size	Rebar spacing mm (in.)
1	25 (1)	#3, #4, # 5, #6 and #7	76 (3)
2	25 (1)	#8, #9, # 10, and #11	76 (3)
3	38 (1.5)	#3, #4, # 5, #6 and #7	76 (3)
4	38 (1.5)	#8, #9, # 10, and #11	76 (3)
5	64 (2.5)	#3, #4, # 5, #6 and #7	76 (3)
6	64 (2.5)	#8, #9, # 10, and #11	76 (3)
7	89 (3.5)	#3, #4, # 5, #6 and #7	76 (3)
8	89 (3.5)	#8, #9, # 10, and #11	76 (3)
9	100 (4.0)	#3, #4, # 5, #6 and #7	76 (3)
10	100 (4.0)	#8, #9, # 10, and #11	76 (3)
11	25 (1)	#3, #4, # 5, #6 and #7	102 (4)
12	25 (1)	#8, #9, # 10, and #11	102 (4)
13	38 (1.5)	#3, #4, # 5, #6 and #7	102 (4)
14	38 (1.5)	#8, #9, # 10, and #11	102 (4)
15	64 (2.5)	#3, #4, # 5, #6 and #7	102 (4)
16	64 (2.5)	#8, #9, # 10, and #11	102 (4)
17	89 (3.5)	#3, #4, # 5, #6 and #7	102 (4)
18	89 (3.5)	#8, #9, # 10, and #11	102 (4)
29	100 (4.0)	#3, #4, # 5, #6 and #7	102 (4)
20	100 (4.0)	#8, #9, # 10, and #11	102 (4)
21	25 (1)	#3, #4, # 5, #6 and #7	127 (5)
22	25 (1)	#8, #9, # 10, and #11	127 (5)
23	38 (1.5)	#3, #4, # 5, #6 and #7	127 (5)
24	38 (1.5)	#8, #9, # 10, and #11	127 (5)
25	64 (2.5)	#3, #4, # 5, #6 and #7	127 (5)
26	64 (2.5)	#8, #9, # 10, and #11	127 (5)
27	89 (3.5)	#3, #4, # 5, #6 and #7	127 (5)

28	89 (3.5)	#8, #9, # 10, and #11	127 (5)
29	100 (4.0)	#3, #4, # 5, #6 and #7	127 (5)
30	100 (4.0)	#8, #9, # 10, and #11	127 (5)
31	25 (1)	#3, #4, # 5, #6 and #7	178 (7)
32	25 (1)	#8, #9, # 10, and #11	178 (7)
33	38 (1.5)	#3, #4, # 5, #6 and #7	178 (7)
34	38 (1.5)	#8, #9, # 10, and #11	178 (7)
35	64 (2.5)	#3, #4, # 5, #6 and #7	178 (7)
36	64 (2.5)	#8, #9, # 10, and #11	178 (7)
37	89 (3.5)	#3, #4, # 5, #6 and #7	178 (7)
38	89 (3.5)	#8, #9, # 10, and #11	178 (7)
39	100 (4.0)	#3, #4, # 5, #6 and #7	178 (7)
40	100 (4.0)	#8, #9, # 10, and #11	178 (7)

(a)

(b)

Figure 4- 12. Concrete samples: (a) The RC sample scanning; (b) The cured RC samples

Culvert

The GPR scanning process involved parallel lines spaced at intervals of 762 mm (2.5 ft) within the culvert cells and inner walls. Figure 4- 13 provides an on-site view of the culvert and an illustration of its geometry. In total, four cells were thoroughly scanned, including the walls and ceilings. Data collected from cell 1 and cell 2 walls were used in this research. The surveying wheel was moved along the parallel lines painted on the surface of the structure, as shown in Figure 4- 14, ensuring comprehensive coverage during the scanning process.

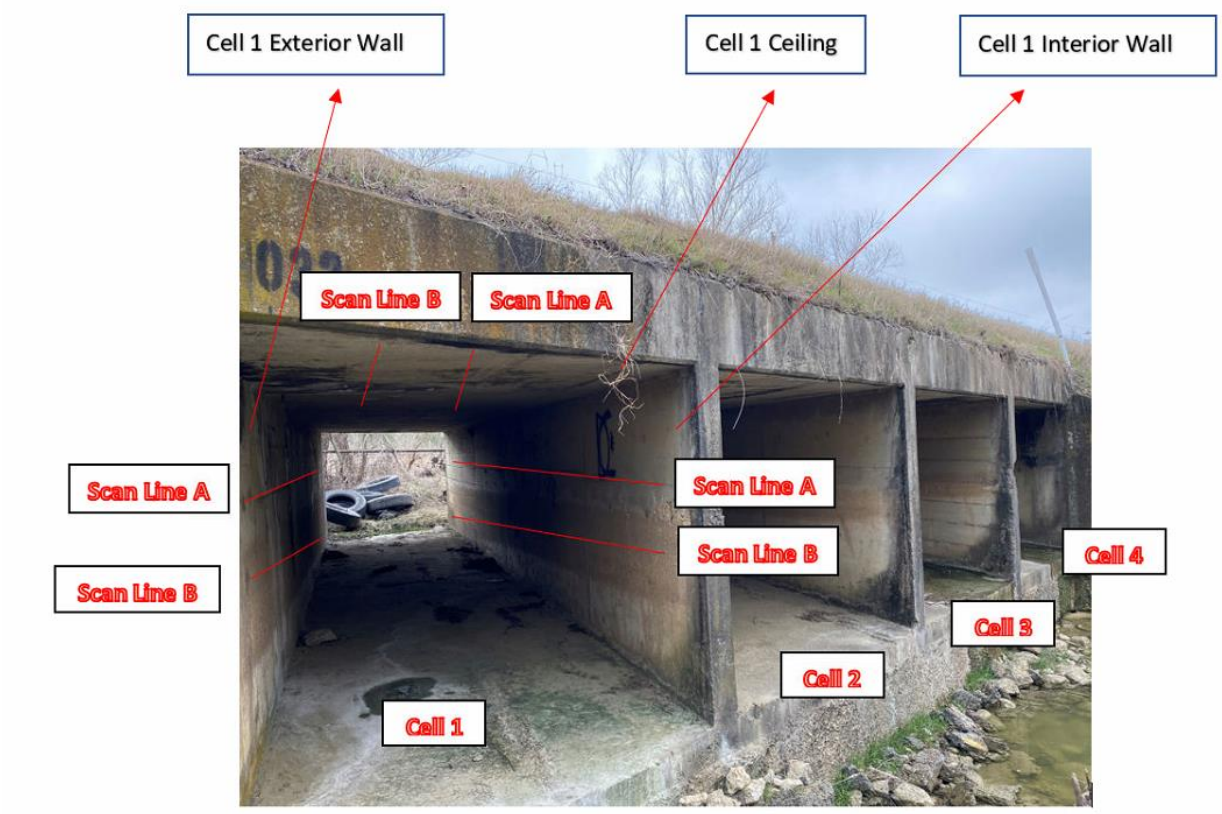

(a)

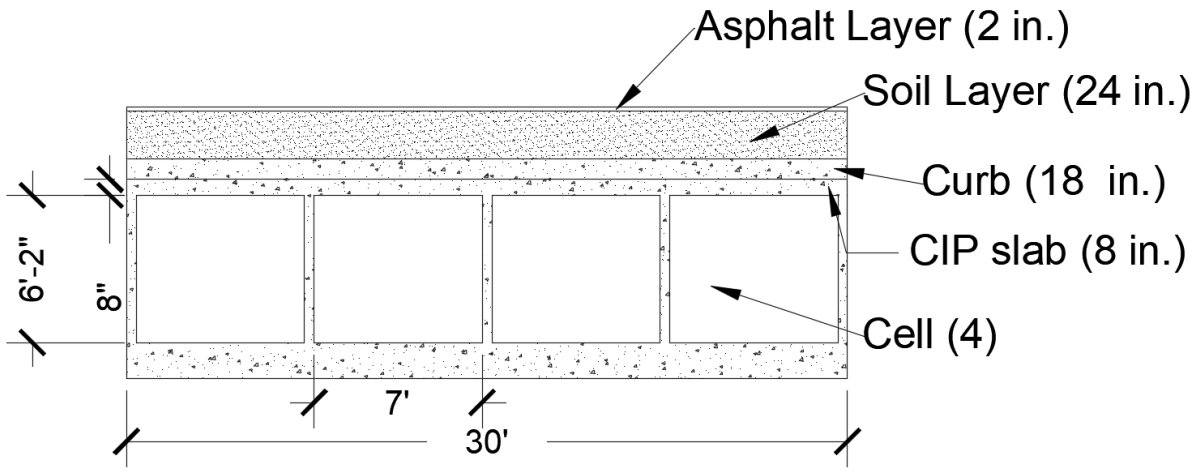

(b)

Figure 4- 13. FM 66 culvert: (a) field view; (2) An illustration of the FM 66 culvert geometry

Figure 4- 14. The GPR scanning on the wall

Highway Bridges

GPR data were collected from three different bridge decks in the DFW area, Texas. The bridges included the SH 310 bridge in Dallas, the I-45 bridge in Palmer, and the US-bridge in Sunnyvale.

In the case of the SH 310 bridge, Figure 4- 15 provides a top view of spans 41 and 42, constructed with fully cast-in-place concrete with a thickness of 178 mm (7 in.). As per the as-built plans, the concrete cover for the deck top layer rebars was 51 mm (2.0 in.). For the GPR data collection, scanning was conducted parallel to the traffic direction on both Lane 1S and Lane 2S.

In the case of Lane 1S (Figure 4- 16), survey lines of 762 mm (2.5 ft.) apart were marked on the deck to facilitate the scanning process, and a GPR scan was performed along the survey lines. The same scanning procedure was applied to Lane 2S of the bridge as well.

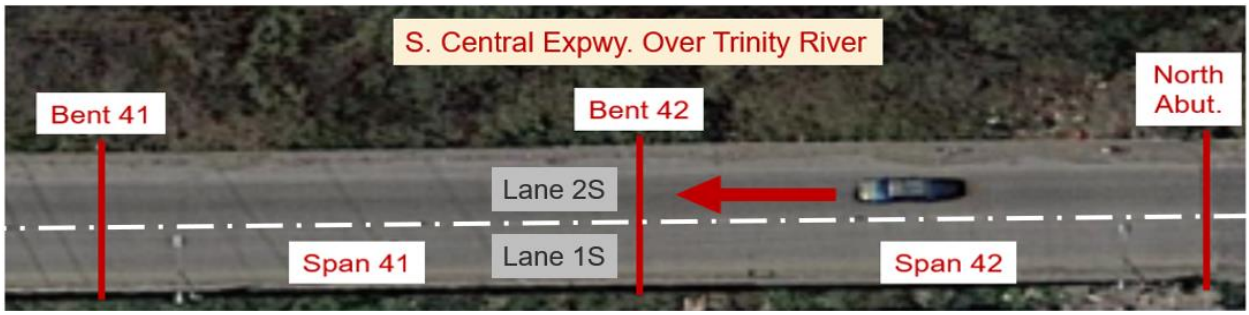

Figure 4- 15. SH 310 Bridge plan view

Figure 4- 16. GPR scanning on Lane 1S

On the I-45 bridge, it was constructed with a cast-in-place concrete deck, measuring 102 mm (4 in.) in thickness and supported by concrete box beams underneath. GPR scanning was carried out parallel to the traffic direction, covering both the Eastbound and Westbound lanes. The top view of the scanning lanes, Eastbound and Westbound Lane, is depicted in Figure 4- 17. The scanning lines for the Eastbound Lane of the bridge can be observed in Figure 4- 18. Multiple paths were scanned using GPR, including path A-C and path B-D, as illustrated in Figure 4- 18.

GPR scanning path over the I-45 Bridge deck. An identical scanning procedure was implemented for the Westbound Lane of the bridge as well.

Figure 4- 17. I-45 Bridge plan view

Figure 4- 18. GPR scanning path over the I-45 Bridge deck

As for the US-80 bridge, its superstructure comprises ten U54 prestressed concrete beams supporting a cast-in-place concrete deck atop a precast concrete panel. The as-built plans specified a top reinforcement cover of 51 mm (2 in.). For GPR scanning, data collection was performed parallel to the traffic direction on both sides of US-80 as well. A truck-mounted antenna was used for the scanning process, and the scanning speed was maintained at 5 miles per hour (mph), as shown in Figure 4- 19.

Figure 4- 19. scanning over the US-80 Bridge deck

4. 3. 2 Performance comparison with other applications

Lab specimens

The graph shown in Figure 4- 20 illustrates the results of rebar depth detection using GPR, with four separate graphs corresponding to different designed rebar depths of 25, 38, 64, 89, and 100 mm (1, 1.5, 2.5, 3.5, and 4 in.). The vertical axis represents the rebar depth, while the horizontal axis represents the rebar itself. The data was processed using both commercial software and the proposed research algorithm. Fluctuations are evident in both lines that depict the rebar depth from the commercial software and the proposed algorithm, occurring around the specified depth and exhibiting deviations within a range of 0.5 inches. These fluctuations stem from the inherent limitations and uncertainties associated with GPR technology, including environmental factors, signal processing algorithms, and system limitations. Despite the fluctuations, the rebar depths processed by the proposed research algorithm consistently show closer alignment to the designed rebar depth, indicating the improved accuracy of the proposed algorithm compared to the commercial software. Notably, as the designed rebar depth increases, the algorithm-processed data line becomes even closer to the designed rebar depth line in the respective graph. This suggests

that the proposed algorithm performs particularly well in detecting deeper rebar depths, exhibiting a higher degree of agreement with the designed depths.

These findings demonstrate the effectiveness of the proposed research algorithm in accurately estimating rebar depths using GPR, surpassing the performance of the commercial software. The results support the potential applicability of the algorithm for practical rebar depth detection in various construction and engineering applications.

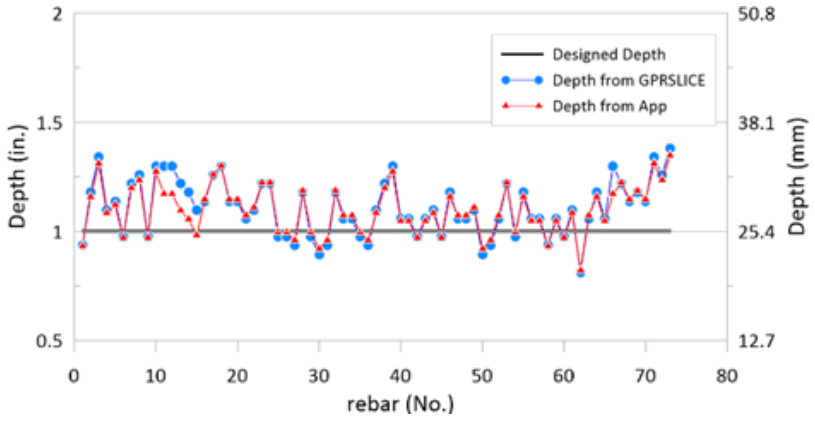

(a)

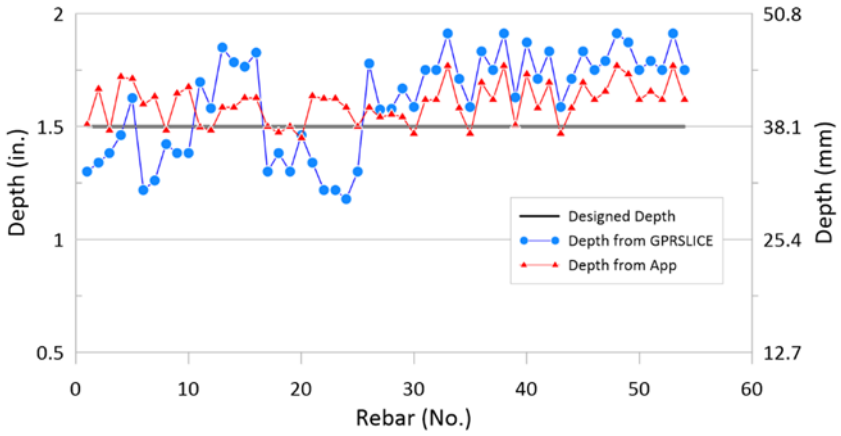

(b)

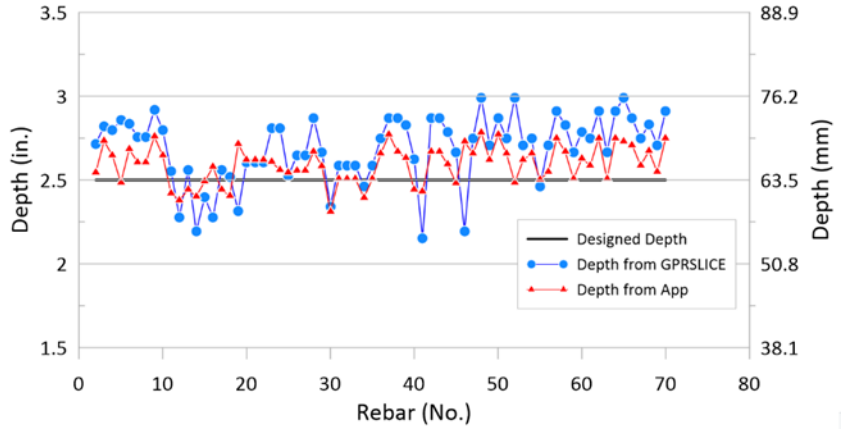

(c)

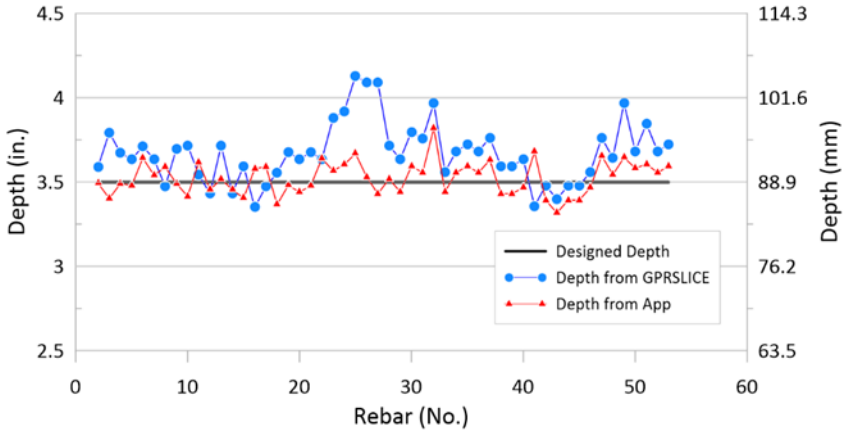

(d)

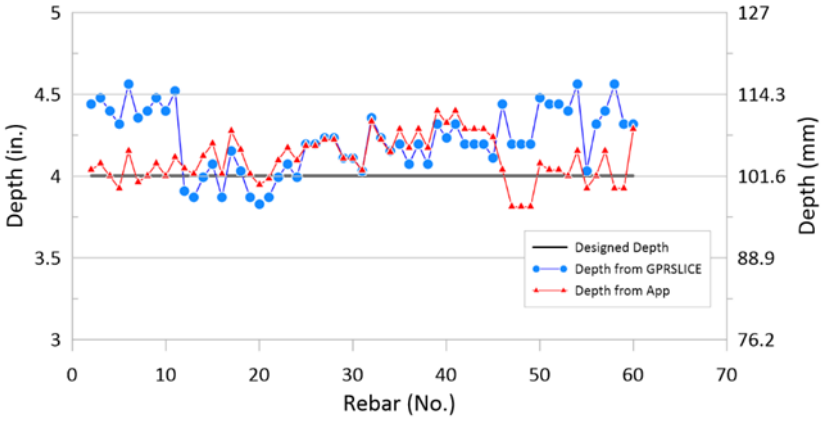

(e)

Figure 4- 20. Different designed rebar depth results: (a) 1.0 in (25 mm); (b)1.5 in (38 mm); (c) 2.5 in (64 mm); (d)3.5 in (89 mm); (d) 4.0 in (102 mm)

FM 66 Culvert

Figure 4- 21 shows the rebar depth estimation from the culvert scanning. The line of the rebar depth proposed by the proposed algorithm aligns notably well with the line of ground truth depth, indicating the algorithm's superior accuracy. Conversely, the line representing the commercial software's results shows deviations from the ground truth depths, suggesting potential inaccuracies.

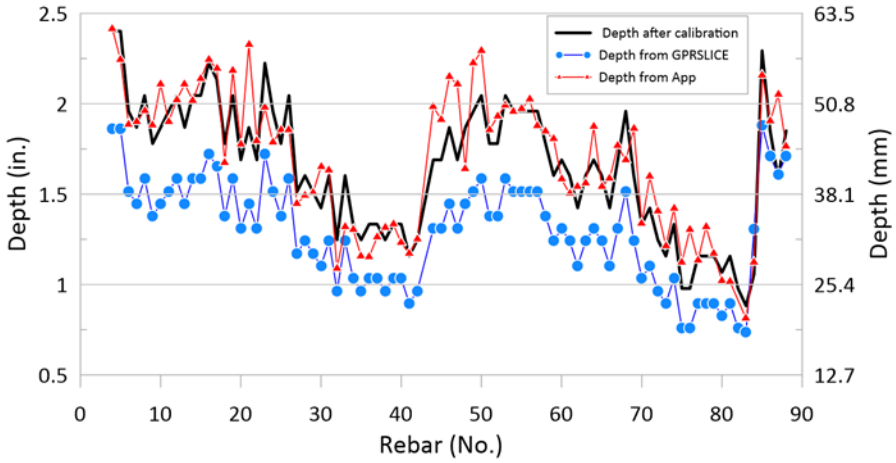

Figure 4- 21. Rebar depth result from FM 66 Culvert scanning

Highway Bridges

Figure 4- 22 presents the rebar depth estimation results obtained from GPR scanning of the three bridges. Figure 4- 22 (a) shows the algorithm processed depth closely aligns with the ground truth depths, indicating the proposed algorithm is outperforming the commercial software. Figure 4- 22 (b) shows algorithm processed depth consistently aligns with the ground truth depths, while the commercial software processed depth tends to overestimate rebar depths. Figure 4- 22 (c) shows both the algorithm and commercial software processed are positioned below the ground truth depths, but the algorithm processed depth is consistently closer to the truth, demonstrating the proposed algorithm's superiority. Overall, the results from all three bridges confirm the effectiveness of the proposed algorithm in accurately estimating rebar depths compared to the commercial software.

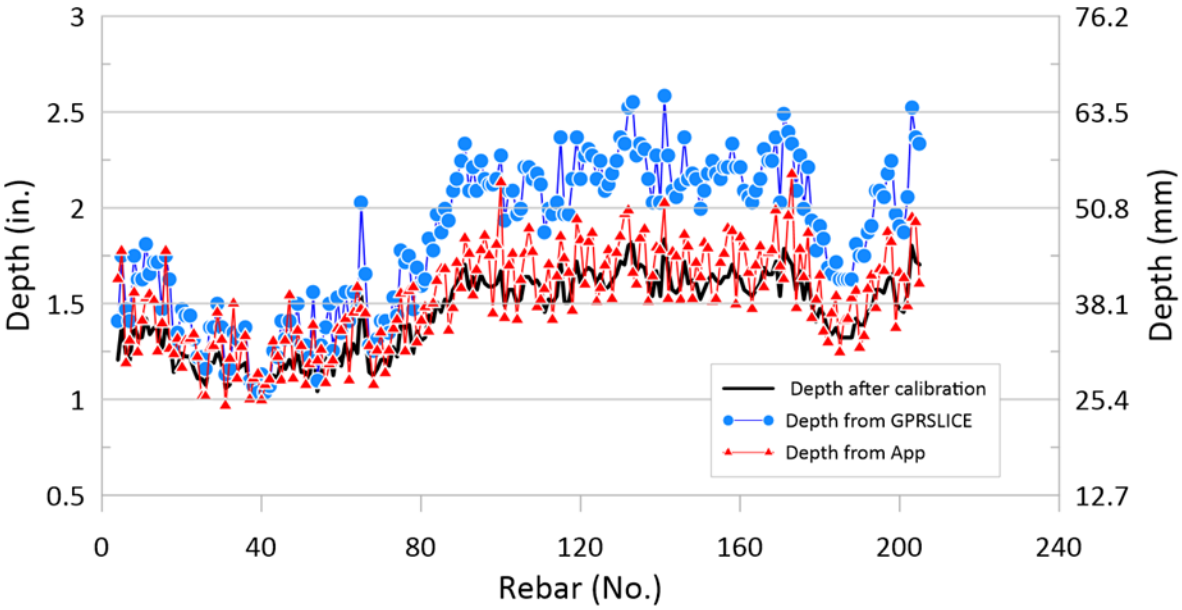
Depth (in.)
Depth (mm)
Rebar (No.)
Depth after calibration
Depth from GPRSLICE
Depth from App

(a)

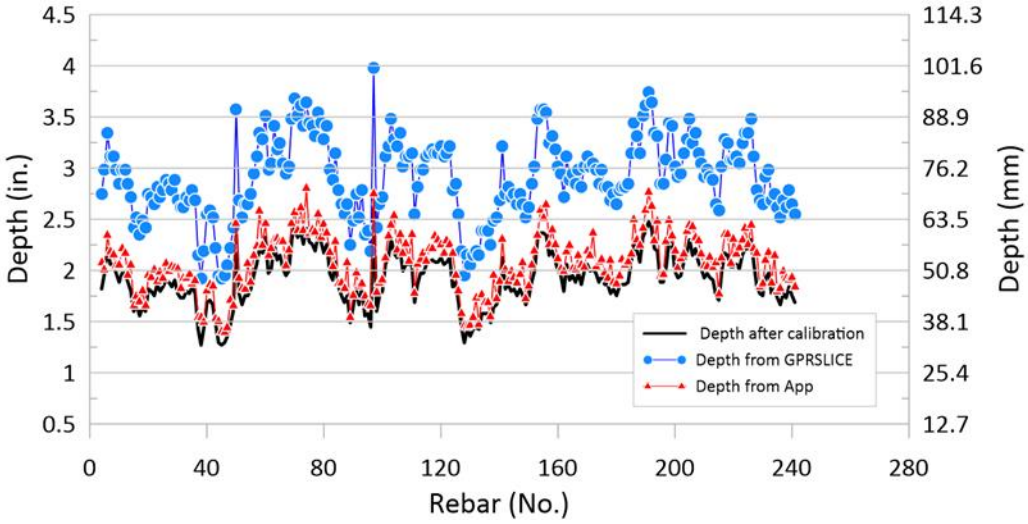
Depth (in.)
Depth (mm)
Rebar (No.)
Depth after calibration
Depth from GPRSLICE
Depth from App

(b)

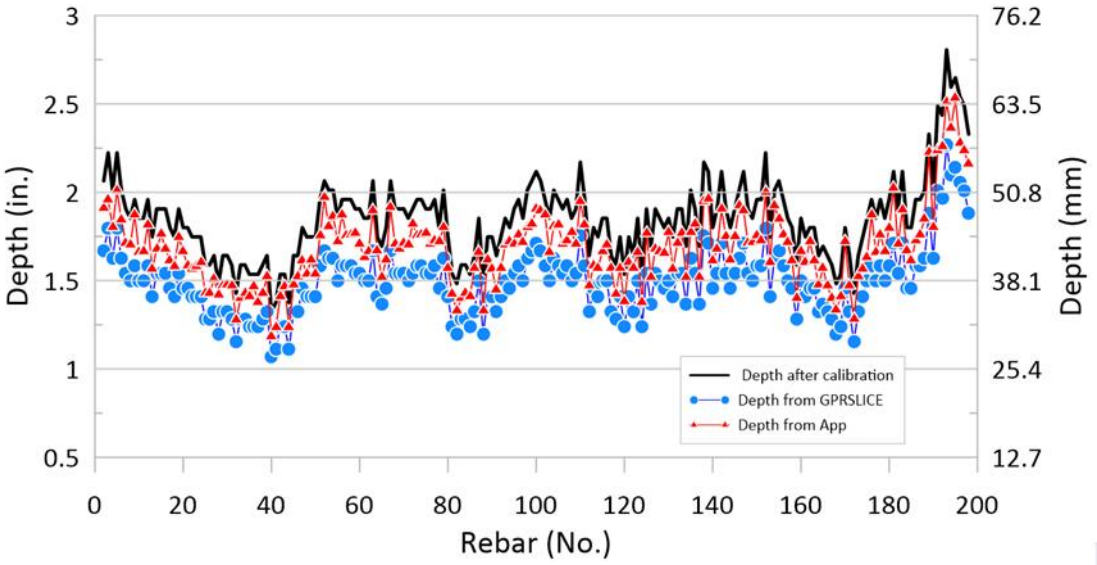

(c)

Figure 4- 22. Rebar depth result: (a) SH 310 Bridge deck; (b) I 45 Bridge deck; (c) US-80 Bridge deck

4. 4 Conclusion

This research proposed a comprehensive GPR data processing algorithm for rebar identification and localization in RC structures. The following conclusions can be made based on this research:

1) The application of this proposed algorithm is effective in addressing inherent challenges, such as unknown time-zero, strong noise, and blurred signals, which are common in GPR data.
2) Moreover, the proposed algorithm calculates electromagnetic wave velocity without requiring core-drilling, further improving the data processing workflow.
3) In addition, the system can directly generate *xls files of the results, saving time and reducing the need for further operations.

4) Notably, the developed processing application achieves full automation, eliminating the need for manual interpretation or rebar-picking, thus enhancing efficiency and accuracy in data processing.
5) The results from the validation of the proposed method on various datasets, including lab-made RC blocks, bridge decks, and a culvert, have shown promising performance in determining the rebar's location. Compared with the existing method, the proposed method is cost-effective, practical, and efficient in accurately and reliably determining rebar location

In summary, with these accomplishments, the proposed method advances GPR data processing for RC structures, offering valuable insights for civil engineering applications. It allows further enhancements and integration into real-time GPR data processing, empowering engineers and researchers with a robust tool for effective GPR data analysis and structural assessment.

4. 5 Future work and recommendations

1) Firstly, high levels of noise remain a challenge for extracting precise areas of interest of the hyperboles. Future research can explore the use of advanced signal processing techniques and noise reduction methods to address this challenge.
2) Secondly, machine learning based approaches can be explored to improve the weak hyperbola reflection in the pre-processing stage. This can include using deep learning models such as convolutional neural networks (CNNs) to enhance the accuracy of detecting and extracting weak hyperbola reflections.
3) Lastly, more field data can be used to further train the machine learning model used in the data processing algorithm.

Acknowledgments

The authors acknowledge the editorial assistant and the thorough revision by the anonymous reviewers who significantly improved the proposed research work.

CHAPTER 5

CONCLUSION AND RECOMMENDATION

5.1 Conclusion

This dissertation aimed to develop novel nondestructive evaluation methods using GPR for the assessment of RC structures. The primary objectives were to address the challenges in GPR data analysis, improve the accuracy and reliability of depth measurements, and provide efficient and practical solutions for concrete infrastructure evaluation. Based on the presented study main results were summarized as follows:

In Chapter 2, a novel time-zero (TZ) correction method was proposed and validated. The objective was to address the challenges of unknown TZ, strong noise, and blurry signals in GPR data analysis. Through extensive experimentation with GPR scanning of 32 RC specimens with different rebar depths, sizes, and spacings, a specific adjusting value of 0.14299 ns ahead of the first negative GPR wave peak was determined for RC structures. This value enabled more accurate depth measurements and reliable assessment of concrete infrastructure with GPR. The antenna pulling-away test further confirmed the accuracy and reliability of the proposed approach. The results demonstrated that the TZ correction method effectively improved the accuracy of depth calculations, mitigating the effects of TZ uncertainty and enhancing the reliability of GPR data interpretation for concrete structures.

In Chapter 3, a nondestructive method for estimating GPR propagation velocity was introduced. The objective was to overcome the limitations of existing empirical models and assumptions by leveraging hyperbolic fitting and travel-time analysis. The proposed algorithm demonstrated the capability to accurately estimate electromagnetic wave velocity without the need for core drilling, making the velocity estimation process more efficient and cost-effective.

Laboratory experiments validated the algorithm's performance and highlighted its robustness and adaptability across various GPR system configurations. The research results showed that the hyperbolic fitting and travel-time analysis technique effectively captured the relationship between arrival times and offsets, providing a reliable estimation of the wave velocity. The algorithm's accuracy and efficiency in estimating GPR wave velocity contribute to enhanced subsurface imaging capabilities and improved data interpretation, benefiting a wide range of applications in civil engineering, geophysics, environmental studies, and archaeology.

In Chapter 4, a comprehensive GPR data processing algorithm for rebar identification and localization in RC structures was developed and validated. The objective was to automate the rebar recognition process, eliminating the need for manual interpretation and rebar-picking. The proposed algorithm corrected time-zero and calculated electromagnetic wave velocity without requiring core-drilling, further improving the data processing workflow. Validation on various datasets, including lab-made reinforced concrete blocks, bridge decks, and a culvert, demonstrated the algorithm's promising performance in determining rebar location. The research results indicated that the automated GPR data processing algorithm effectively processed raw GPR data, identifying and localizing reinforcement in RC structures with high accuracy and reliability. The algorithm's ability to directly generate *xls files of the results also contributed to improved efficiency in data processing. The findings from this research open avenues for further enhancements and integration into real-time GPR data processing, empowering engineers and researchers with a robust tool for effective GPR data analysis and structural assessment.

The research conducted in this dissertation makes significant contributions to the field of GPR-based assessment of concrete structures. The TZ correction method proposed in Chapter 2 provides an innovative and reliable approach for improving depth measurements and data analysis

in GPR scans of RC structures. The nondestructive method for estimating GPR propagation velocity presented in Chapter 3 offers a practical solution for enhancing subsurface imaging capabilities and improving data interpretation. Lastly, the comprehensive GPR data processing algorithm in Chapter 4 contributes a valuable tool for efficient and accurate identification and localization of reinforcement in RC structures.

The results of this research have several implications for theory, practice, and policy. The novel TZ correction method enhances the accuracy of depth measurements in GPR data analysis, enabling a more reliable assessment of concrete infrastructure health. The nondestructive method for estimating GPR propagation velocity eliminates the need for core drilling, making subsurface investigations more efficient and cost-effective. The comprehensive GPR data processing algorithm streamlines the rebar identification process, facilitating efficient structural assessment and maintenance. These advancements have the potential to improve decision-making in civil engineering applications and contribute to the overall sustainability and safety of concrete structures.

5.2 Recommendation

Although the proposed methods have shown promising results, some limitations should be acknowledged. The TZ correction method assumes relatively equal water content in concrete samples, which may not always be the case in real-world scenarios. The adjusting value for different material surfaces requires further investigation. Additionally, the comprehensive GPR data processing algorithm may face challenges in extracting precise areas of interest from hyperboles in the presence of high levels of noise.

Future research can focus on addressing the limitations highlighted in this study, including investigating the impact of varying water content on TZ correction and evaluating the applicability

of the proposed algorithm to different material surfaces. Advanced signal processing techniques and machine learning approaches can be explored to enhance the robustness of the GPR data processing algorithm in noisy environments. Additional field data can be used to further train and validate the machine learning model. Furthermore, improvement can be made to the machine learning model for hyperbola fitting by exploring available model packages on the market. Additionally, enhancing the developed application could involve incorporating functions such as corrosion detection and contour map plotting. Further development to create a standalone app for user-friendly download and installation would also be beneficial.

In conclusion, this Ph.D. dissertation has made significant strides in the field of nondestructive evaluation of concrete structures using Ground Penetrating Radar. The novel TZ correction method, nondestructive estimation of GPR propagation velocity, and comprehensive GPR data processing algorithm contribute valuable tools for enhancing the accuracy, efficiency, and reliability of GPR data analysis. These research findings have practical applications in civil engineering, offering improved structural assessment capabilities and supporting sustainable infrastructure development. The proposed methods hold great promise for future research and implementation in real-world scenarios, empowering engineers and researchers with innovative techniques for effective and reliable assessment of concrete infrastructure.

Appendix A: GPR Data Format

DZT file format

The RADAN DZT file is a binary file containing a header followed by scans of data. The header contains information concerning the settings used to collect the data and the header size.

Note: This information is provided to the User for informational use only. It is not supported by GSSI technical support and is provided for those Users who are proficient in working in a C programming environment.

Internal structures

```
struct tagRFDate // File header date/time structure
{
unsigned sec2 : 5;          // second/2 (0-29)
unsigned min : 6;           // minute (0-59)
unsigned hour : 5;          // hour (0-23)
unsigned day : 5;           // day (1-31)
unsigned month: 4;          // month (1=Jan, 2=Feb, etc.)
unsigned year : 7;          // year-1980 (0-127 = 1980-2107)
};
struct tagRFCoords // Start/End position
{
float
rh_fstart;
float
rh_fend;
};
struct RGPS // GPS record/system time SYNC
{
char RecordType[4];         // “GGA”
DWORD TickCount;            // CPU tick count
double PositionGPS[4];      // Latitude (positive if 'N'), Longitude (positive if ‘E’),
// Altitude, FIXUTC
```

};

Constants and macros

```
// constants

const int MINHEADSIZE =
1024; const int
PARAREASIZE = 128;

const int GPSAREASIZE = 2 * sizeof(RGPS);

const int INFOAREASIZE (MINHEADSIZE - PARAREASIZE- GPSAREASIZE) ;

// structure member alignment macros
#define TYPEBYTE(x,n) BYTE x##[n]

#define SHORTBYTE(x) TYPEBYTE(x,2) // short int
(16 bit) #define FLOATBYTE(x) TYPEBYTE(x,4) //
float

#define RFDATEBYTE(x) TYPEBYTE(x,4) //
tagRFDate #define COORDBYTE(x)
TYPEBYTE(x,8) // tagRFCoords
```

RADAN header structure

```
struct tagRFHeader
{                                   // Offset in bytes
short rh_tag;                       // 0x00ff if header, 0xfnff for old file        00
short rh_data;                      // Offset to Data from beginning of file        02
                                        //  if rh_data < MINHEADSIZE then

                                        //  offset is MINHEADSIZE * rh_data

                                        //  else offset is MINHEADSIZE *rh_nchan
short rh_nsamp;                     // samples per scan                             04
short rh_bits;                      // bits per data word (8,16, 32) *              06
short rh_zero;                      // if rh_system is SIR 30,                      08
                                        // then equals repeats/sample

                                        // otherwise is 0x80 for 8 bit data and

                                        // 0x8000 for 16 bit data
FLOATBYTE(rhf_sps);                 // scans per second                             10
FLOATBYTE(rhf_spm);                 // scans per meter                              14
FLOATBYTE(rhf_mpm);                  // meters per mark                             18
FLOATBYTE(rhf_position);            // position (ns)                                22
FLOATBYTE(rhf_range);               // range (ns)                                   26
short rh_npass;                     // num of passes for 2-D files                  30
RFDATEBYTE(rhb_cdt);                // Creation date & time                         32
RFDATEBYTE(rhb_mdt);                // Last modification date & time                36
short rh_rgain;                     // offset to range gain function                40
short rh_nrgain;                    // size of range gain function                  42
short rh_text;                      // offset to text                               44
short rh_ntext;                     // size of text                                 46
```

```
short rh_proc;                  // offset to processing history        48
short rh_nproc;                 // size of processing history          50
short rh_nchan;                 // number of channels                  52
FLOATBYTE(rhf_epsr);            // average dielectric constant         54
FLOATBYTE(rhf_top);             // position in meters                  58
FLOATBYTE(rhf_depth);           // range in meters                     62
COORDBYTE(rh_coordX);           // X coordinates                       66
FLOATBYTE(rhf_servo_level);     // gain servo level                    74
char reserved[3];               // reserved                            78
BYTE rh_accomp;                 // Ant Conf component                  81
short rh_sconfig;               // setup config number                 82
short rh_spp;                   // scans per pass                      84
short rh_linenum;               // line number                         86
COORDBYTE(rh_coordY);           // Y coordinates                       88
BYTE rh_lineorder:4;            //                                     96
BYTE rh_slicetype:4;            //                                     96
char rh_dtype;                  //                                     97
char rh_antname[14];            // Antenna name                        98
BYTE rh_pass0TX:4;              // Activ Transmit mask                 112
BYTE rh_pass1TX:4;              // Activ Transmit mask                 112
BYTE rh_version:3;              // 1 – no GPS; 2 - GPS                 113
BYTE rh_system:5;               // (see below for description)**       113
char rh_name[12];               // Initial File Name                   114
short rh_chksum;                // checksum for header                 126
char variable[INFOAREASIZE];    // Variable data                       128
RGPS rh_RGPS[2];                // GPS info                            944

}; // End of tagRFHeader
```

*Data format is little-endian. Eight-byte and sixteen-byte samples are unsigned integers. Thirty-two-bit samples are signed integers. **rh_system values:

Control Unit	Number
SIR 2000	2
SIR 3000	3
TerraVision	4
SIR 20	6
SS Mini	7
SIR 30	9

The RADAN DZX file is an XML file used to store all information related to a RADAN DZT file that is not contained in the DZT file. It contains GPS data, user annotations (such as marks and mark names), interactive interpretation data (such as layers and targets), 3D information, such as profile starting and ending coordinates, and RADAN 7 settings, such as a color table, color transform, display gain, and units.

REFERENCE

[1] D. K. Harris, O. E. Ozbulut, A. Bagheri, M. S. Dizaji, A. K. Ndong, and M. Alipour, "Load Rating Strategies for Bridges With Limited or Missing As-Built Information," Virginia Transportation Research Council (VTRC), 2020.

[2] B. Sangoju and S. Vasanthakumar, "A STUDY ON THE APPLICABILITY OF COVER METER AND GPR SURVEY FOR COVER THICKNESS AND REBAR IDENTIFCATION IN REINFORCED CONCRETE STRUCTURES."

[3] R. Barnes and T. Zheng, "Research on factors affecting concrete cover measurement," *Journal of Nondestructive Testing*, 2008.

[4] D. J. Daniels, "Ground penetrating radar," *Encyclopedia of RF and Microwave Engineering*, 2005.

[5] V. M. Malhotra and N. J. Carino, *Handbook on nondestructive testing of concrete*. CRC press, 2003.

[6] X. Xu, Q. Zeng, D. Li, J. Wu, X. Wu, and J. Shen, "GPR detection of several common subsurface voids inside dikes and dams," *Engineering Geology*, vol. 111, no. 1-4, pp. 31-42, 2010.

[7] S. Santos-Assunçao, V. Perez-Gracia, O. Caselles, J. Clapes, and V. Salinas, "Assessment of complex masonry structures with GPR compared to other non-destructive testing studies," *Remote Sensing*, vol. 6, no. 9, pp. 8220-8237, 2014.

[8] K. Dinh, N. Gucunski, J. Kim, and T. H. Duong, "Understanding depth-amplitude effects in assessment of GPR data from concrete bridge decks," *NDT & E International*, vol. 83, pp. 48-58, 2016.

[9] X. Zeng and G. A. McMechan, "GPR characterization of buried tanks and pipes," *Geophysics*, vol. 62, no. 3, pp. 797-806, 1997.

[10] Y. S. Cho, S. U. Hong, and M. S. Lee, "The assessment of the compressive strength and thickness of concrete structures using nondestructive testing and an artificial neural network," *Nondestructive Testing and Evaluation,* vol. 24, no. 3, pp. 277-288, 2009.

[11] F. Tosti and E. Slob, "Determination, by using GPR, of the volumetric water content in structures, substructures, foundations and soil," in *Civil Engineering Applications of Ground Penetrating Radar*: Springer, 2015, pp. 163-194.

[12] M. R. Shaw, S. G. Millard, T. C. K. Molyneaux, M. J. Taylor, and J. H. Bungey, "Location of steel reinforcement in concrete using ground penetrating radar and neural networks," *Ndt & E International,* vol. 38, no. 3, pp. 203-212, 2005.

[13] M. I. Hasan and N. Yazdani, "Ground penetrating radar utilization in exploring inadequate concrete covers in a new bridge deck," *Case Studies in Construction Materials,* vol. 1, pp. 104-114, 2014.

[14] D. J. Clem, T. Schumacher, and J. P. Deshon, "A consistent approach for processing and interpretation of data from concrete bridge members collected with a hand-held GPR device," *Construction and Building Materials,* vol. 86, pp. 140-148, 2015.

[15] J. Hugenschmidt, A. Kalogeropoulos, F. Soldovieri, and G. Prisco, "Processing strategies for high-resolution GPR concrete inspections," *NDT & E International,* vol. 43, no. 4, pp. 334-342, 2010.

[16] S. M. Toolbox, "Matlab," *Mathworks Inc,* 1993.

[17] R. Yelf, "Where is true time zero?," 2004, vol. 1: IEEE, pp. 279-282.

[18] K. Agred, G. Klysz, and J. P. Balayssac, "Location of reinforcement and moisture assessment in reinforced concrete with a double receiver GPR antenna," *Construction and Building Materials,* vol. 188, pp. 1119-1127, 2018.

[19] S. Laurens, J. P. Balayssac, J. Rhazi, G. Klysz, and G. Arliguie, "Non-destructive evaluation of concrete moisture by GPR: experimental study and direct modeling," *Materials and structures,* vol. 38, no. 9, pp. 827-832, 2005.

[20] A. V. Ristic, D. Petrovacki, and M. Govedarica, "A new method to simultaneously estimate the radius of a cylindrical object and the wave propagation velocity from GPR data," *Computers & Geosciences,* vol. 35, no. 8, pp. 1620-1630, 2009.

[21] K. Dinh, N. Gucunski, and T. H. Duong, "An algorithm for automatic localization and detection of rebars from GPR data of concrete bridge decks," *Automation in Construction,* vol. 89, pp. 292-298, 2018.

[22] W. Al-Nuaimy, Y. Huang, M. Nakhkash, M. T. C. Fang, V. T. Nguyen, and A. Eriksen, "Automatic detection of buried utilities and solid objects with GPR using neural networks and pattern recognition," *Journal of applied Geophysics,* vol. 43, no. 2-4, pp. 157-165, 2000.

[23] V. Krause, I. Abdel-Qader, O. Abudayyeh, and S. Yehia, "An image segmentation algorithm for the detection of rebar in bridge decks from GPR scans," 2007: IEEE, pp. 114-119.

[24] P. Gamba and S. Lossani, "Neural detection of pipe signatures in ground penetrating radar images," *IEEE Transactions on Geoscience and Remote Sensing,* vol. 38, no. 2, pp. 790-797, 2000.

[25] E. Pasolli, F. Melgani, and M. Donelli, "Automatic analysis of GPR images: A pattern-recognition approach," *IEEE Transactions on Geoscience and Remote Sensing,* vol. 47, no. 7, pp. 2206-2217, 2009.

[26] P. Kaur, K. J. Dana, F. A. Romero, and N. Gucunski, "Automated GPR rebar analysis for robotic bridge deck evaluation," *IEEE transactions on cybernetics,* vol. 46, no. 10, pp. 2265-2276, 2015.

[27] S. Gibb and H. M. La, "Automated rebar detection for ground-penetrating radar," 2016: Springer, pp. 815-824.

[28] E. Pasolli, F. Melgani, M. Donelli, R. Attoui, and M. De Vos, "Automatic detection and classification of buried objects in GPR images using genetic algorithms and support vector machines," 2008, vol. 2: IEEE, pp. II-525.

[29] M. Szymczyk and P. Szymczyk, "Preprocessing of GPR data," *Image Processing & Communications,* vol. 18, no. 2-3, pp. 83-90, 2013.

[30] L. W. Galagedara, G. W. Parkin, and J. D. Redman, "An analysis of the ground-penetrating radar direct ground wave method for soil water content measurement," *Hydrological Processes,* vol. 17, no. 18, pp. 3615-3628, 2003.

[31] J. F. C. Sham and W. W. L. Lai, "Development of a new algorithm for accurate estimation of GPR's wave propagation velocity by common-offset survey method," *NDT & E International,* vol. 83, pp. 104-113, 2016.

[32] K. Dinh, N. Gucunski, and T. Zayed, "Automated visualization of concrete bridge deck condition from GPR data," *NDT & E International,* vol. 102, pp. 120-128, 2019.

[33] A. Tarussov, M. Vandry, and A. De La Haza, "Condition assessment of concrete structures using a new analysis method: Ground-penetrating radar computer-assisted visual interpretation," *Construction and Building Materials,* vol. 38, pp. 1246-1254, 2013.

[34] H. Liu, C. Lin, J. Cui, L. Fan, X. Xie, and B. F. Spencer, "Detection and localization of rebar in concrete by deep learning using ground penetrating radar," *Automation in Construction,* vol. 118, p. 103279, 2020.

[35] C. Maas and J. Schmalzl, "Using pattern recognition to automatically localize reflection hyperbolas in data from ground penetrating radar," *Computers & geosciences,* vol. 58, pp. 116-125, 2013.

[36] Q. Lu, J. Pu, and Z. Liu, "Feature extraction and automatic material classification of underground objects from ground penetrating radar data," *Journal of Electrical and Computer Engineering,* vol. 2014, 2014.

[37] L. Qiao, Y. Qin, X. Ren, and Q. Wang, "Identification of buried objects in GPR using amplitude modulated signals extracted from multiresolution monogenic signal analysis," *Sensors,* vol. 15, no. 12, pp. 30340-30350, 2015.

[38] H. M. Jol, *Ground penetrating radar theory and applications*. elsevier, 2008.

[39] W. Kim, *Ground penetrating radar application for non-destructive testing: Bridge deck inspection and dowel bar detection*. 2003.

[40] A. D. Perkins, J. J. Amrol, F. A. Romero, and R. L. Roberts, "DOT specification development based on evaluation of ground-penetrating radar system performance in measuring concrete cover (reinforcement depth) on new bridge deck construction," *Structural Material Technology IV,* vol. 28, pp. 53-60, 2000.

[41] A. Benedetto and L. Pajewski, *Civil engineering applications of ground penetrating radar*. Springer, 2015.

[42] F. Soldovieri, R. Solimene, and G. Kouemou, "Ground penetrating radar subsurface imaging of buried objects," *Radar Technology,* pp. 105-126, 2010.

[43] @theconstructor2. "How does a Ground Penetrating Radar (GPR) Work? [PDF]." @theconstructor2. https://theconstructor.org/practical-guide/ndt/how-ground-penetrating-radar-gpr-work/43370/ (accessed.

[44] R. Persico, *Introduction to ground penetrating radar: inverse scattering and data processing*. John Wiley & Sons, 2014.

[45] J. J. Daniels, "Fundamentals of ground penetrating radar," 1989: Society of Exploration Geophysicists, pp. 62-142.

[46] G. Klysz, J. P. Balayssac, S. Laurens, and X. Ferrieres, "Numerical FDTD simulation of the direct wave propagation of a GPR coupled antenna," 2004, vol. 1: IEEE, pp. 45-48.

[47] GSSI. "Exploration Instruments." https://www.exiusa.com/item/radar/radan-7-0 (accessed.

[48] E. G. Ernenwein, "Imaging in the ground-penetrating radar near-field zone: a case study from New Mexico, USA," *Archaeological Prospection*, vol. 13, no. 2, pp. 154-156, 2006.

[49] K. Dinh, N. Gucunski, J. Kim, and T. H. Duong, "Method for attenuation assessment of GPR data from concrete bridge decks," *Ndt & E International*, vol. 92, pp. 50-58, 2017.

[50] K. Dinh, N. Gucunski, and T. H. Duong, "Migration-based automated rebar picking for condition assessment of concrete bridge decks with ground penetrating radar," *NDT & E International*, vol. 98, pp. 45-54, 2018.

[51] P. Wiwatrojanagul, R. Sahamitmongkol, S. Tangtermsirikul, and N. Khamsemanan, "A new method to determine locations of rebars and estimate cover thickness of RC structures using GPR data," *Construction and Building Materials*, vol. 140, pp. 257-273, 2017.

[52] L. Steinbeck, A. Mester, E. Zimmermann, A. Klotzsche, and S. van Waasen, "In situ time-zero correction for a ground penetrating radar monitoring system with 3000 antennas," *Measurement Science and Technology*, vol. 33, no. 7, p. 075904, 2022.

[53] H. Zadhoush and A. Giannopoulos, "Optimizing GPR time-zero adjustment and two-way travel time wavelet measurements using a realistic three-dimensional numerical model," *Near Surface Geophysics*, vol. 20, no. 2, pp. 208-226, 2022.

[54] M. Rasol, V. Pérez-Gracia, and S. S. Assunção, "Analysis and calibration of ground penetrating radar shielded antennas," 2018: IEEE, pp. 1-4.

[55] A. Alin, "Minitab," *Wiley interdisciplinary reviews: computational statistics*, vol. 2, no. 6, pp. 723-727, 2010.

[56] A. C. I. Committee, *Building Code Requirements for Structural Concrete (ACI 318-19): An ACI Standard ; Commentary on Building Code Requirements for Structural Concrete (ACI 318R-19)* (Opal Collection). American Concrete Institute, 2019.

[57] C. Astm, "Standard practice for making and curing concrete test specimens in the field," ed, 2012.

[58] J. M. Reynolds, *An introduction to applied and environmental geophysics*. John Wiley & Sons, 2011.

[59] Z. Xiang, G. Ou, and A. Rashidi, "Integrated Approach to Simultaneously Determine 3D Location and Size of Rebar in GPR Data," *Journal of Performance of Constructed Facilities*, vol. 34, no. 5, p. 04020097, 2020.

[60] W. W.-L. Lai, X. Derobert, and P. Annan, "A review of Ground Penetrating Radar application in civil engineering: A 30-year journey from Locating and Testing to Imaging and Diagnosis," *Ndt & E International*, vol. 96, pp. 58-78, 2018.

[61] L.-B. Liu and R.-Y. Qian, "Ground Penetrating Radar: A critical tool in near-surface geophysics," *Chinese Journal of Geophysics,* vol. 58, no. 8, pp. 2606-2617, 2015.

[62] S. Hubbard, J. Chen, K. Williams, J. Peterson, and Y. Rubin, "Environmental and agricultural applications of GPR," 2005.

[63] R. Knight, "Ground penetrating radar for environmental applications," *Annual Review of Earth and Planetary Sciences,* vol. 29, no. 1, pp. 229-255, 2001.

[64] L. Bianchini Ciampoli, F. Tosti, N. Economou, and F. Benedetto, "Signal processing of GPR data for road surveys," *Geosciences,* vol. 9, no. 2, p. 96, 2019.

[65] U. B. Halabe, K. Maser, and E. Kausel, "Propagation characteristics of electromagnetic waves in concrete," *US Army Research Office,* 1989.

[66] Q. Cao and I. L. Al-Qadi, "Effect of moisture content on calculated dielectric properties of asphalt concrete pavements from ground-penetrating radar measurements," *Remote Sensing,* vol. 14, no. 1, p. 34, 2021.

[67] J. Hugenschmidt and R. Loser, "Detection of chlorides and moisture in concrete structures with ground penetrating radar," *Materials and Structures,* vol. 41, pp. 785-792, 2008.

[68] J. A. Huisman, S. S. Hubbard, J. D. Redman, and A. P. Annan, "Measuring soil water content with ground penetrating radar: A review," *Vadose zone journal,* vol. 2, no. 4, pp. 476-491, 2003.

[69] W. L. Lai, W. F. Tsang, H. Fang, and D. Xiao, "Experimental determination of bulk dielectric properties and porosity of porous asphalt and soils using GPR and a cyclic moisture variation technique," *Geophysics,* vol. 71, no. 4, pp. K93-K102, 2006.

[70] G. Klysz and J. P. Balayssac, "Determination of volumetric water content of concrete using ground-penetrating radar," *Cement and concrete research,* vol. 37, no. 8, pp. 1164-1171, 2007.

[71] Z. Anxue, J. Yansheng, W. Wenbing, and W. Cheng, "Experimental studies on GPR velocity estimation and imaging method using migration in frequency-wavenumber domain," 2000: IEEE, pp. 468-473.

[72] Z. Lin and W. Jiang, "Estimation on Underground Electromagnetic Wave Velocity Based on Characteristics of Shallow-Buried Small Target Echo," 2015: IEEE, pp. 723-726.

[73] W. W. L. Lai, J. F. C. Sham, and F. Xie, "Correction of GPR wave velocity with distorted hyperbolic reflection in underground utility's GPR survey," 2016: IEEE, pp. 1-4.

[74] R. Delf, R. G. Bingham, A. Curtis, S. Singh, B. Schwarz, and A. Giannopoulos, "Automated estimation of englacial radar velocity from zero offset data; implications for glacier bed topography retrieval," 2020, p. 20484.

[75] P. K.-W. Lau, B. W.-Y. Cheung, W. W.-L. Lai, and J. F.-C. Sham, "Characterizing pipe leakage with a combination of GPR wave velocity algorithms," *Tunnelling and Underground Space Technology,* vol. 109, p. 103740, 2021.

[76] L. Liu and T. Guo, "Determining the condition of hot mix asphalt specimens in dry, water-saturated, and frozen conditions using GPR," *Journal of Environmental & Engineering Geophysics,* vol. 8, no. 2, pp. 143-149, 2003.

[77] K. H. Le, T. H. Dang, and T. Van Nguyen, "Determining velocities in high frequency electromagnetic prospecting by phase shift plus interpolation migration," *VNUHCM Journal of Science and Technology Development,* vol. 19, no. 1, pp. 74-82, 2016.

[78] T. Van Nguyen and C. V. A. Le, "Energy Difference Of High Frequency Electromagnetic Waves Amplitude In Detecting Buried Objects At Ho Chi Minh City, Vietnam," *VNUHCM Journal of Natural Sciences,* vol. 5, no. 1, pp. 925-932, 2021.

[79] H. Perroud and M. Tygel, "Velocity estimation by the common-reflection-surface (CRS) method: Using ground-penetrating radar data," *Geophysics,* vol. 70, no. 6, pp. B43-B52, 2005.

[80] L. Weifeng and L. Mingxing, "The estimation of the ground penetrating radar wave velocity based on template matching," 2010, vol. 2: IEEE, pp. 362-364.

[81] Y. Wijewardana and L. W. Galagedara, "Estimation of spatio-temporal variability of soil water content in agricultural fields with ground penetrating radar," *Journal of Hydrology,* vol. 391, no. 1-2, pp. 24-33, 2010.

[82] H. Liu and M. Sato, "Dynamic groundwater level estimation by the velocity spectrum analysis of GPR," 2012: IEEE, pp. 413-418.

[83] J. De Pue, M. Van Meirvenne, and W. M. Cornelis, "Accounting for surface refraction in velocity semblance analysis with air-coupled GPR," *IEEE Journal of Selected Topics in Applied Earth Observations and Remote Sensing,* vol. 9, no. 1, pp. 60-73, 2015.

[84] F. Cui, S. Li, and L. Wang, "The accurate estimation of GPR migration velocity and comparison of imaging methods," *Journal of Applied Geophysics,* vol. 159, pp. 573-585, 2018.

[85] H. Yuan, M. Montazeri, M. C. Looms, and L. Nielsen, "Diffraction imaging of ground-penetrating radar data," *Geophysics,* vol. 84, no. 3, pp. H1-H12, 2019.

[86] E. Du *et al.*, "Soil moisture calibration equations for active layer GPR detection—A case study specially for the Qinghai–Tibet Plateau permafrost regions," *Remote Sensing*, vol. 12, no. 4, p. 605, 2020.

[87] P. Huggenberger, E. Meier, and A. Pugin, "Ground-probing radar as a tool for heterogeneity estimation in gravel deposits: advances in data-processing and facies analysis," *Journal of Applied Geophysics*, vol. 31, no. 1-4, pp. 171-184, 1994.

[88] Y. LeCun, Y. Bengio, and G. Hinton, "Deep learning," *nature*, vol. 521, no. 7553, pp. 436-444, 2015.

[89] R. Girshick, J. Donahue, T. Darrell, and J. Malik, "Rich feature hierarchies for accurate object detection and semantic segmentation," 2014, pp. 580-587.

[90] Z. Gong and H. Zhang, "Research on GPR image recognition based on deep learning," 2020, vol. 309: EDP Sciences, p. 03027.

[91] D. Kumlu, "GPR Image Recovery Effect on Faster R-CNN-Based Buried Target Detection," *Journal of Electromagnetic Engineering and Science*, vol. 22, no. 5, pp. 591-598, 2022.

[92] Z. Liu, X. Gu, W. Wu, X. Zou, Q. Dong, and L. Wang, "GPR-based detection of internal cracks in asphalt pavement: A combination method of DeepAugment data and object detection," *Measurement*, vol. 197, p. 111281, 2022.

[93] Z. Wang, T. Lan, X. Qu, S. Gao, Z. Yu, and X. Yang, "Improved SSD Framework for Automatic Subsurface Object Indentification for GPR Data Processing," 2021: IEEE, pp. 2078-2081.

[94] Y. Li, Z. Zhao, Y. Luo, and Z. Qiu, "Real-time pattern-recognition of GPR images with YOLO v3 implemented by tensorflow," *Sensors*, vol. 20, no. 22, p. 6476, 2020.

[95] T. Wunderlich, D. Wilken, B. S. Majchczack, M. Segschneider, and W. Rabbel, "Hyperbola Detection with RetinaNet and Comparison of Hyperbola Fitting Methods in GPR Data from an Archaeological Site," *Remote Sensing*, vol. 14, no. 15, p. 3665, 2022.

[96] S. Matlab, "Matlab," *The MathWorks, Natick, MA*, 2012.